

**Search for Beyond the Standard Model signals in a quark-gluon tagged  
dijet final state with the ATLAS detector**

by

Katherine Rybacki

A thesis submitted in partial fulfillment of the requirements for the degree of

Doctor of Philosophy

Department of Department of Physics  
Lancaster University

© Katherine Rybacki, 2023

# Abstract

A search for Beyond the Standard Model (BSM) particles that decay into a pair of jets is performed using  $139 \text{ fb}^{-1}$  of ATLAS pp collision data recorded from the Large Hadron Collider operating at  $\sqrt{s} = 13 \text{ TeV}$ . To increase the sensitivity to resonances preferentially decaying to one or more gluons, selection cuts are applied to tag jets as either quark-like or gluon-like, based on the number of tracks in the jet. The expected cross-section limits at  $6 \text{ TeV}$  are presented, and are shown to represent an improvement of up to 25% (for the significance of observing an excited quark using a single gluon tag). The results are consistent with the Standard Model.

*Firstly, a massive thank you to my supervisor Iain Bertram, for sharing your huge amount of knowledge and for being the only supervisor I know who will read his students' code! Thank you to everyone in my office too. From my very first day when I found a crossbow on my desk (thank you, Ben!), every single one of you has helped me laugh my way through my Lancaster years. Mell, I don't know what I'd do without you and your zoo - particularly Harley and Nellie! But it wouldn't be a PhD. I owe you a deep and heartfelt thank you for all your help, and for always, always being there for me.*

*And finally, thank you to my family, for all your love and support; but especially to my parents. This dedication is far too short to express how much you've done for me. This is as much your PhD as it is mine, and I'd never have made it here without you.*

# Acknowledgments

## 0.1 Declaration

This thesis is a presentation of original research performed by the author. It has not been previously submitted for the award of a higher degree. The work presented in this thesis was ultimately made possible by a large number of ATLAS collaborators. The specific contributions of the author are summarised below:

- Production of ROOT trees for the analysis group (data and H', strings, quantum black holes,  $q^*$  Monte Carlo), implementing all selection and quality cuts.
- Setup of the fitting framework xmlAnaWSBuilder, adaptations to accommodate the dijet mass spectrum and fit stability testing.
- Deriving track reconstruction and modelling uncertainties on the tagger.
- Figures in sections 5 and 6 are produced with other members of the ATLAS analysis group.

# Table of Contents

0.1	Declaration . . . . .	iv
<b>1</b>	<b>Introduction</b>	<b>1</b>
1.1	Motivation . . . . .	1
1.2	Objectives . . . . .	2
1.3	Outline . . . . .	2
<b>2</b>	<b>Background</b>	<b>3</b>
2.1	The Standard Model . . . . .	3
2.1.1	Dijet Cross Section . . . . .	5
2.2	Beyond the Standard Model . . . . .	6
2.2.1	Benchmark Models . . . . .	7
2.3	The ATLAS Detector . . . . .	18
2.3.1	Luminosity . . . . .	18
2.3.2	The ATLAS Detector . . . . .	21
2.3.3	Coordinate System . . . . .	23
2.3.4	The Inner Detector . . . . .	24
2.3.5	Electromagnetic Calorimeter . . . . .	25
2.3.6	Hadronic Calorimeter . . . . .	27
2.3.7	Muon Spectrometer . . . . .	28
2.3.8	Trigger System . . . . .	29
2.4	Jets and Jet Phenomenology . . . . .	30
2.4.1	Jet Algorithms . . . . .	36

2.4.2	Jet Tagging . . . . .	41
<b>3</b>	<b>Data Selection</b>	<b>44</b>
3.1	Jet Trigger . . . . .	44
3.2	Event Selection . . . . .	47
3.2.1	Good Runs Lists . . . . .	49
3.3	Jet Reconstruction and Calibration . . . . .	50
3.4	Jet Calibration . . . . .	52
3.4.1	Pile-up Corrections . . . . .	54
3.4.2	Jet Energy Scale and $\eta$ Calibration . . . . .	54
3.5	Jet Energy Resolution . . . . .	67
3.6	Jet Cleaning . . . . .	69
3.7	Quality Cuts . . . . .	75
3.8	Monte Carlo Samples . . . . .	77
3.9	Data/MC comparisons . . . . .	79
<b>4</b>	<b>Quark-Gluon Tagging</b>	<b>86</b>
4.1	Expected Signal Significance . . . . .	86
4.1.1	GG Selection . . . . .	86
4.1.2	QG Selection . . . . .	87
4.2	Optimization of $y^*$ . . . . .	91
4.3	Tagging Procedure . . . . .	93
4.4	Systematic Uncertainties . . . . .	104
4.4.1	Existing Approach . . . . .	104
4.4.2	Pure MC-based Uncertainties . . . . .	108
4.4.3	Track Uncertainties . . . . .	112
4.4.4	Experimental Uncertainties . . . . .	112

<b>5</b>	<b>Fitting Framework</b>	<b>117</b>
5.1	xmlAnaWSBuilder . . . . .	117
5.2	Statistical Method . . . . .	119
5.2.1	Limit Setting . . . . .	119
5.2.2	Implementation . . . . .	121
5.3	Uncertainties . . . . .	123
5.4	Pseudodata . . . . .	124
5.5	Spurious Signal . . . . .	127
5.6	Signal Injection Tests . . . . .	133
<b>6</b>	<b>Results</b>	<b>136</b>
6.1	Model-independent Gaussian Limits . . . . .	136
<b>7</b>	<b>Conclusion and Future Work</b>	<b>141</b>

# List of Tables

2.1	Bosons in the Standard Model . . . . .	5
3.1	Parameters used to build the two types of topological cluster available in the standard ATLAS reconstruction. From [67]. . . . .	52
3.2	The five observables used to derive a calibration to improve JES resolution. . . . .	57
3.3	Summary of the uncertainties from the in-situ calibrations. . . . .	64
3.4	Additional systematic uncertainties in the JES. Uncertainties from electron, photon and muon energy scales [75]. . . . .	66
3.5	Jet selection criteria for the dijet analysis . . . . .	78
3.6	Cutflow for this analysis applied to full Run2 Data (2015-2018). . . . .	85
4.1	The efficiency of truth quark and gluon jet selection by the quark (gluon) selection $\epsilon_{qQ}, \epsilon_{gQ}$ ( $\epsilon_{qG}, \epsilon_{gG}$ ). E.g. at a truth quark efficiency of 0.9, the truth gluon efficiency is 0.6. . . . .	87
4.2	The efficiency for truth quark or gluon jets passing the QG selection $\epsilon_{qq}, \epsilon_{gQ}$ ( $\epsilon_{qG}, \epsilon_{gG}$ ) . . . . .	90
4.3	Values of the constants $m_q$ and $c_q$ from Equation 4.5 such that $n_{\text{track}} \leq n_g$ for truth gluon jets with efficiencies ranging from 65 to 95%. . . . .	99
4.4	Values of the constants $m$ and $c$ from Equation 4.5 such that $n_{\text{track}} \geq n_q$ for truth quark jets with efficiencies ranging from 65 to 95%. . . . .	99
4.5	Dataset comparisons and uncertainties drawn from each. . . . .	109
4.6	The four tracking uncertainties and the systematic associated with each. . . . .	112

5.1	Spurious Signal tests using Gaussian signals for the 1 gluon tagged category. . . . .	128
5.2	Spurious Signal tests using Gaussian signals for 2 gluon tagged category.	129

# List of Figures

2.1	The Standard Model of particle physics, which includes all discovered elementary particles [2] . . . . .	4
2.2	Exclusion limits on heavy particles by the ATLAS Collaboration. Figure by the ATLAS Collaboration [8] . . . . .	8
2.3	Exclusion limits on heavy particles by the CMS Collaboration (Figure by CMS Collaboration [9]). . . . .	9
2.4	Dijet mass (dijet $m_{jj}$ ) distributions for the strings signal at various masses, generated using the Strings version 1.00 Monte Carlo event generator [10]. . . . .	11
2.5	Feynman diagram of excited quark ( $q^*$ ) production from quark - gluon scattering [12]. . . . .	12
2.6	Transitions between ordinary and excited fermions via gauge-boson emission. $f(L)$ denotes a left-handed fermion, $f(R)^*$ is a right-handed excited fermion. The striped circle denotes the presence of virtual, off-mass-shell particles. The striped circle and black circle at the vertices are equivalent. . . . .	14
2.7	The peaks from excited quarks of various masses shown against the Standard Model dijet mass spectrum for pp collisions with $\sqrt{s} = 16$ TeV. [17] . . . . .	15
2.8	Mass distributions for the $q^*$ signal with the following properties: spin 1/2, isospin 1/2, compositeness scale set to the $q^*$ mass and the coupling constants of SM quarks. . . . .	16

2.9	Signal Shapes for the $H'$ at various mass points. Simulated SU(3) singlet scalar production and decay using Pythia . . . . .	19
2.10	Schematic diagram of the ATLAS detector. The function of each component is summarised in the subsequent sections [34]. . . . .	22
2.11	A computer generated image of the ATLAS calorimeter [36] . . . . .	25
2.12	A barrel module where the different layers are visible. The granularity of the layers in $\eta$ and $\phi$ is also shown [37]. . . . .	26
2.13	Graphical representations of (a) the String model of hadronisation and (b) the Cluster model of hadronisation of a $q\bar{q}$ pair [48][49]. . . . .	32
2.14	On the left is a diagram illustrating collinear emission of a gluon, while on the right a soft gluon is emitted [51]. . . . .	35
2.15	Cancellation of singularities in Sterman Weinberg jets [51]. Singularities arise with opposite signs and cancel. . . . .	36
2.16	A high mass dijet event: two high- $p_T$ jets with invariant mass 2.8 TeV. A track $p_T$ cut of 2.5 GeV has been applied for the display. On the left is an event reconstruction, the lower right panel shows a jet reconstructed via a cone algorithm. . . . .	37
2.17	Collinear unsafety in algorithms. Partons are represented by lines and their height is proportional to the energy of the parton. With a virtual correction, the parton on the right is more energetic, so this is selected as the initiating parton and grouped with the central particle. With collinear splitting the left-most parton becomes most energetic, with the algorithm selecting this parton and again the central one instead [51]. . . . .	38
2.18	An event generated with Herwig and with four different clustering algorithms applied. This figure illustrates how applying different algorithms to the same event leads to different outcomes [55]. . . . .	38

2.19	In the left diagram, the quark jets have properties largely determined by the emitted gluons. The same configuration can be produced from the right diagram, in which a third hard parton, a gluon, splits into two gluons with momenta comparable to the showered gluons. These two amplitudes interfere, and so it may not make sense to describe the final state configuration as having two quark jets. In this case, the amplitude for the shower diagram on the left is much larger than the hard-gluon-splitting event for the same final state kinematics. As the gluons become more collinear with the quarks, the first amplitude is divergent. From [60]. . . . .	43
3.1	Cumulative data quality efficiency vs total integrated luminosity of the ATLAS experiment, 2015-2018. The sharp drops in efficiency are due to single incidents which results in rejection of data on quality grounds. There have been improvements year-on-year during Run 2[61] . . . .	45
3.2	Workflow for Data Quality assessment, from [62]. Data is first processed by online shifters (who monitor data in real time and deal with any issues that arise). It is then passed on to Data Quality (DQ) experts, who decide which data is usable for analyses, to continue the process offline. . . . .	46
3.3	Trigger efficiencies and their corresponding fits for HLT_j420 and HLT_-j225_gsc420_boffperf_split triggers as a function of jet $p_T$ for 2018 data [63]. . . . .	48
3.4	Calibration stages for EM-scale jets, from [66]. . . . .	53
3.5	Average energy response (a) and $\eta$ difference (b) between truth and reco jets for truth energies of 30, 60, 110, 400 and 1200 GeV [68]. . . .	55

3.6	The average jet response in MC simulation as a function of the GSC variables for three ranges of truth jet $p_T$ . Jets are constrained to $ \eta  < 0.1$ for the distributions of calorimeter and track-based observables and $ \eta  < 1.3$ for the muon nsegments distribution. The distributions of the underlying observables in MC simulation are shown in the lower panels for each truth jet $p_T$ region, normalized to unity. . . . .	58
3.7	The average jet response in MC simulation as a function of the GSC variables for three ranges of $p_T^{\text{truth}}$ . a) is the number of muon track segments ghost-associated with the jet. b) is shown with both preceding calorimeter corrections applied, and the punch-through distribution c) is shown with the four calorimeter and track-based corrections applied [66]. The distributions of the underlying observables in MC simulation are shown in the lower panels for each truth jet $p_T$ region, normalized to unity. . . . .	59
3.8	Data/MC EM+JES jet response ratio for the $Z$ +jet, $\gamma$ +jet and multi-jet channels used for in-situ calibrations. The black line indicates the final correction. The uncertainties are shown in dark blue (statistical) and light green (total). Finally the original ratios are shown. From [73], [72]. . . . .	61
3.9	Final total uncertainty of jets in the JES as a function of (a) jet $p_T$ at $\eta = 0$ and (b) $\eta$ at $p_T = 80$ GeV. Systematic uncertainty components include pile-up, punch-through, and uncertainties propagated from the $Z/\gamma$ +jet and multi-jet balance (absolute in situ JES) and $\eta$ -intercalibration (relative in situ JES). The flavor composition and response uncertainties assume a quark and gluon composition taken from Pythia dijet MC simulation (inclusive jets) [75]. . . . .	67

3.10	An illustration of the variables used in the bisector method for JER uncertainties. The $\eta$ -axis corresponds to the azimuthal angular bisector of the dijets, and the $\Psi$ -axis is orthogonal to the $\eta$ -axis. Both are transverse to the beam which goes into the page [81]. . . . .	68
3.11	Variables used to distinguish between good and fake jets. (a) $\langle Q \rangle$ (b) $f_Q^{LAr}$ , (c) $f_Q^{HEC}$ and (d) $E_{neg}$ . Good jets in 2015 data are shown by black points with simulation results in blue in (d), along with a sample enriched with fake jets from 2015 data in red points. Differences are significant and so allow easy differentiation. From [83]. . . . .	72
3.12	Distributions of the energy ratio variables, defined to identify the difference between fake and good jets. (a) $f_{EM}$ , (b) $f_{HEC}$ and (c) $f_{max}$ for good jets in 2015 data, shown in black points, the simulation (blue shaded histograms) and a sample enriched with fake jets from 2015 data denoted with red points [83]. . . . .	74
3.13	Distributions of (a) $f_{ch}$ and (b) $f_{ch}$ and $f_{max}$ . Efficiency is high in the good jets enriched samples from data in black points and also for simulation in blue shaded histograms. Deviations of the fake jet enriched samples in red points from both data and MC are significant [83]. . . . .	75
3.14	$f_{ch}$ as a function of the EM fraction $f_{EM}$ for (a) good jets and (b) samples enriched with fake jets. From [83]. . . . .	76
3.15	Data-MC comparisons for (a) jet angle $\Delta\phi$ , (b) the scalar sum of jet $p_T$ (HT), (c) jet energy $E$ , (d) jet energy at the EM scale and (e,f) jet angle $\eta, \phi$ in the detector. . . . .	80
3.16	Data-MC comparisons for (a) jet multiplicity, (b) reconstructed jet angle $\phi$ , (c) reconstructed jet angle $\eta$ , (d) jet $p_T$ , (e) jet rapidity and (f) dijet invariant mass $m_{jj}$ [94]. . . . .	81

3.17	Data-MC comparisons for (a) number of jets, (b) number of primary vertices, (c) rapidity boost and (d) the angular separation $y^*$ of the two jets [94]. . . . .	82
3.18	Data-MC comparisons of charged track multiplicity for $QQ$ in (a) and (b), $QG$ in (c) and (d) and $GG$ in (e) and (f) [94]. . . . .	83
4.1	The expected significance for an $H'$ with values of $\epsilon_{qG}$ from 0.9 to 0.6, compared to the significance with no selection with the dashed line. Masses are in GeV and go up to the highest simulated signal mass for the $H'$ , which for this analysis is 7 TeV [94]. . . . .	88
4.2	The expected significance for a $q^*$ compared to the significance with no selection applied. The legend gives efficiency pairs $(\epsilon_{gG}, \epsilon_{qG})$ . Masses are in GeV [94]. . . . .	90
4.3	The expected significance for a $q^*$ compared to the significance with no selection applied. The key gives efficiency pairs $(\epsilon_{gG}, \epsilon_{qG})$ . Masses are in GeV [94]. . . . .	91
4.4	String significance as a function of the $y^*$ cut for (a) $\geq 1$ gluon-tag and (b) 2 gluon-tag [94]. . . . .	92
4.5	$H'$ significance as a function of the $y^*$ cut for (a) $\geq 1$ gluon-tag and (b) 2 gluon-tag [94]. . . . .	92
4.6	The fraction of dijet events that are initiated by quark-quark events (blue), quark-gluon events (green) and gluon-gluon events (red) in simulated data [94]. . . . .	94
4.7	Distribution of the reconstructed number of tracks in a jet across different $p_T$ bins and with the Pythia8 A14 generator tune results input into GEANT4. Jets must satisfy $ \eta  < 2.1$ and tracks pass if $p_T > 500$ MeV along with quality criteria described in [57]. Figure from [57]. . . . .	95

4.8	The cumulative distribution of $n_{\text{track}}$ for truth quark (blue) and gluon (red) initiated jets satisfying $800 < p_T < 900$ GeV. . . . .	97
4.9	The values of $n_{\text{track}}$ for (a) 70%, (b) 75% and (c) 80% quark (blue) and gluon (red) selection efficiencies in every $p_T$ bin, along with the best fit to Equation 4.5 [94]. . . . .	98
4.10	Examples of the Pythia8 Truth $n_{\text{track}}$ distributions between 500 and 800 GeV. The quark jets shown in blue have fewer tracks than the gluon jets in red, with the separation increasing at higher $p_T$ . Quark jets are far more numerous at high $p_T$ . . . . .	101
4.11	Pythia8 Truth $n_{\text{track}}$ distributions across all $p_T$ bins. The difference in the distributions of quark and gluon jets shows how it can act as an excellent discriminator. . . . .	102
4.12	Pythia8 Truth $n_{\text{track}}$ distributions between 4500 and 7000 GeV for excited quark samples. At high $p_T$ the number of quark and gluon jets is roughly equal [94]. . . . .	103
4.13	In (a), the simulated fraction of jets originating from gluons as a function of jet $p_T$ for the more forward jet (down triangle), the more central jet (up triangle), and the difference between these two fractions (circle). The error bars represent PDF and ME uncertainties. In (b), the jet $p_T$ dependence of the average charged-particle multiplicity of quark- and gluon-initiated jets. The error bands include the experimental uncertainties, as well as PDF and ME uncertainties. The MC statistical uncertainties are smaller than the markers. The uncertainty band for the N3LO pQCD prediction is determined by varying the scale $\mu$ by a factor of two up and down. Both (a) and (b) use Pythia with the CT10 PDF. From [98]. . . . .	105
4.14	The systematic uncertainties on the particle-level charged particle distribution for a 60% quark jet efficiency working point, from [57]. . . . .	106

4.15	A comparison of charged particle multiplicity for the most forward jet in a dijet pair, from data, Pythia8 with the A14 tune and Pythia8 with the AZNLO tune from [57]. Data and uncertainties are from [98] via HEPData [105]. . . . .	107
4.16	The total systematic uncertainty for the 60% quark jet efficiency working point of the quark/gluon tagger for (a) quark jets and (b) gluon jets. From [57]. . . . .	108
4.17	Quark Efficiency vs Gluon Efficiency for SherpaCSS. The number of quarks misidentified by the tagger as gluons is the quark efficiency, produced separately for each $p_T$ bin, and the number of gluons correctly identified is the gluon efficiency. . . . .	110
4.18	Plots are made by calculating the cut that gives a certain gluon efficiency for each generator, applying this cut to other generators and comparing the resulting gluon efficiency to the original. The hadronization uncertainty is given by the difference between SherpaCSS and SherpaLund, while a comparison of Pythia and SherpaCSS gives the PDF uncertainty. . . . .	111
4.19	(a) Track reco efficiency variation vs nominal (b) Fake rate variation vs nominal . . . . .	113
4.20	(c) Weak modes variation vs nominal (d) Remaining systematic variations vs nominal (vary cone acceptance, TIDE efficiency) . . . . .	114
4.21	Systematics from experimental (detector-dependent) uncertainties on track reconstruction for a 60% quark jet efficiency of the tagger, from [57]. . . . .	116

5.1	The workflow in the xmlAnaWSBuilder. The terms widely used in discussions is listed in 'Physics terms' with the specific inputs the code needs for these listed under 'Technical terms'. The file formats required as inputs and given as outputs are shown in the 'Formats' section [114].	118
5.2	Untagged dijet spectrum with $ y^*  < 0.8$ using full Run-2 data fitted with the 5-parameter global fit function (Equation 5.6).	125
5.3	To obtain the fraction of events passing one gluon tag selection from the inclusive spectrum, analysis selection cuts are applied to the Pythia dijet MC samples. Figure 27 shows the fraction of the MC events events passing 1 gluon tag selection.	126
5.4	The distribution of the number of signal events from 1000 pseudo experiments fitted with a 10% width for a Gaussian with mass 4750 GeV.	130
5.5	The distribution of the number of signal events from 1000 pseudo experiments fitted with an 8 TeV Gaussian with a 10% width for 8000 GeV mass.	130
5.6	Spurious signal for single-tag distributions across the full mass range. The horizontal lines correspond to 0.5 and 0.79, the mean of a one-sided Gaussian. A high signal to noise ratio, i.e. well above the dashed lines, would indicate a signal that is less likely to be random statistical fluctuation.	131
5.7	Spurious signal for double-tag distributions across the full mass range. The horizontal lines correspond to 0.5 and 0.79, the mean of a one-sided Gaussian. A high signal to noise ratio, i.e. well above the dashed lines, would indicate a signal that is less likely to be random statistical fluctuation.	132

5.8	Signal injection tests for the 1 gluon tag category using Gaussian signals of (a) 5% width, (b) 10% width and (c) 15% width (of the full fit range). Where the points are above the grey line, a signal higher than input is being extracted, and below the line the reverse is true. . . . .	134
5.9	Signal injection test for the 2 gluon tag category using Gaussian signals of (a) 5% width, (b) 10% width and (c) 15% width (of the full fit range). The grey dashed line represents the correct result, where the number of extracted signal events is equal to the number of events injected. Where the points are above the grey line, a signal higher than input is being extracted, and below the line the reverse is true. . . . .	135
6.1	Model-independent limits set in the untagged $y^* < 0.8$ Signal Region using Gaussian resonances of varying widths from 0% to 15% of their peak position without systematics included using the full $139 \text{ fb}^{-1}$ Run-2 dataset. . . . .	137
6.2	Model-independent limits set in the one-gluon tagged $y^* < 0.6$ Signal Region using Gaussian resonances of varying widths from 0% to 15% of their peak position without systematics included using the full $139 \text{ fb}^{-1}$ Run-2 dataset . . . . .	138
6.3	Model-independent limits set in the two-gluon tagged $y^* < 0.8$ Signal Region using Gaussian resonances of varying widths from 0% to 15% of their peak position without systematics included using the full $139 \text{ fb}^{-1}$ Run-2 dataset . . . . .	139

# Chapter 1

## Introduction

### 1.1 Motivation

The Standard Model (SM) is unmatched in its success at describing particle physics phenomena, and achieves an exceptional degree of precision. However, there are gaps in its description of the universe, notably its inconsistency with general relativity and the observed matter-antimatter asymmetry in the Universe.

The Large Hadron Collider (LHC) is a powerful tool in trying to resolve these issues. Seven experiments have constructed detectors around the collider, to analyse the vast amounts of data it produces. Of these seven, ATLAS and CMS are the largest. The ATLAS experiment has carried out many searches for Beyond the Standard Model (BSM) physics, but as yet no evidence of new physics has been found.

There are many processes that can occur in the proton-proton collisions at the LHC. Jets, collimated sprays of particles produced by hadronization of quarks or gluons, are the most abundant final state objects produced in the ATLAS detector. The frequency of these types of events, coupled with the predictions of many BSM theories, mean dijet events are a particularly useful signature to search for (although a huge array of techniques are employed). Dijet events also probe the highest energies available at the LHC compared to other final states. QCD predicts a smoothly falling

invariant mass distribution for dijet events, and new particles coupling to quarks or gluons would show as a resonance in this spectrum.

## 1.2 Objectives

Given the increasing volumes of data, and with mass distributions spanning over six orders of magnitude, new techniques are needed to more effectively analyze the large pool of results and to increase the sensitivity of searches for new physics. One such technique, addressed in this thesis, is quark-gluon tagging.

## 1.3 Outline

Chapter 2 will discuss the theory around jets with Chapter 3 dedicated to data selection and quality processes. Chapter 4 describes quark/gluon tagging, with Chapter 5 dedicated to the fitting framework. Chapter 6 presents the results of the limit-setting procedure.

Finally, in Chapter 7, a summary of the significant results is presented.

# Chapter 2

## Background

### 2.1 The Standard Model

Searches for BSM physics often rely on the accuracy of our knowledge of the Standard Model. Given the incredibly precise predictions it provides, and with experiment notably backing these up by agreeing to as closely as ten parts in a billion (e.g. in tests of the fine structure constant of QED [1]), it is a solid foundation to rest upon. It neatly encapsulates 3 of the 4 fundamental forces into a framework that includes every known particle, and although General Relativity is incompatible with the model, on an atomic scale the effects of gravity are negligible, and so do not derail the theory's predictions.

While it omits gravity, this relativistic quantum field theory does describe the interactions of the strong, electromagnetic and weak forces. It belongs to the  $U(1)_Y \times SU(2)_L \times SU(3)$  gauge group, and applies the concept of gauge invariance to the fields it describes. The particles arising from the SM are categorised according to their spin, with fermions (antimatter/matter particles) having half-integer spins and obeying Fermi-Dirac statistics, and bosons (force carriers) having integer spins and obeying Bose-Einstein statistics. Fermions are further divided into quarks, which are subject to strong interactions, and leptons which are not. Quarks and leptons are each organised into three generations, each identical copies of the first generation that differ only by flavour quantum number and mass. Every lepton generation includes one

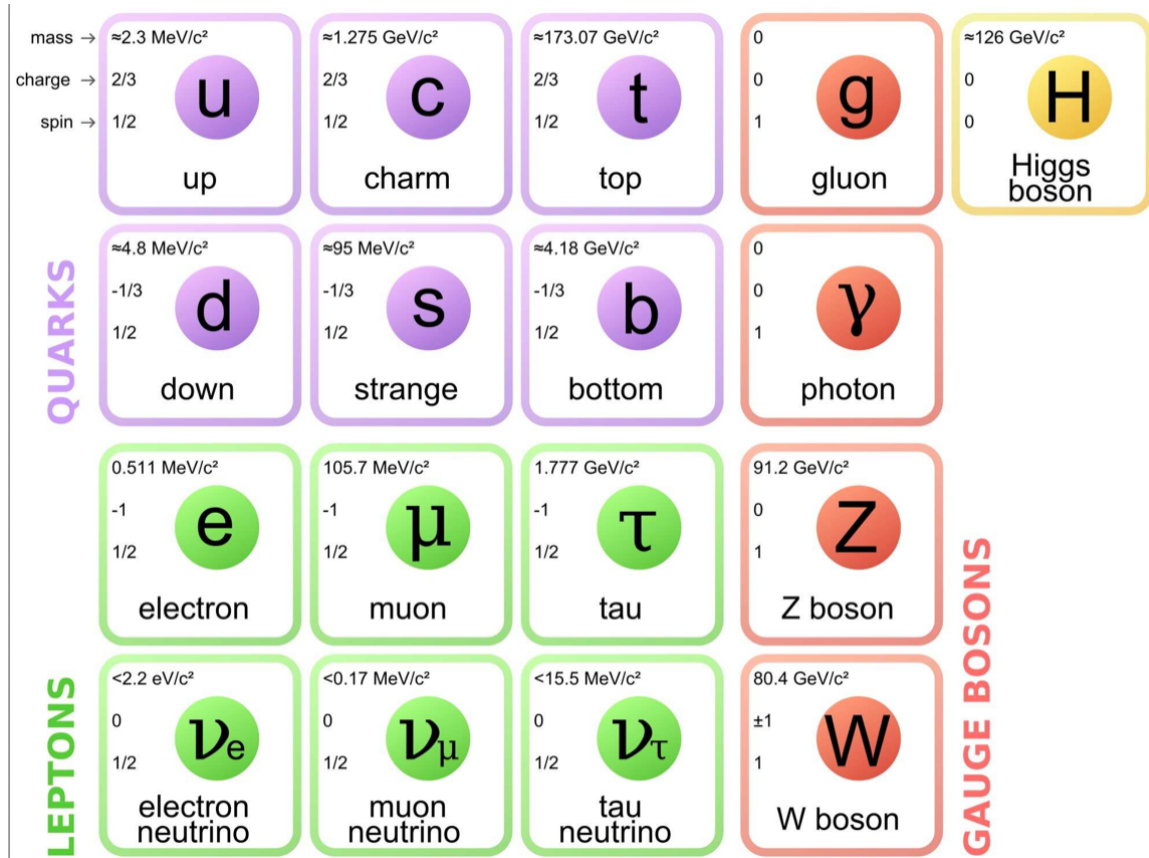


Figure 2.1: The Standard Model of particle physics, which includes all discovered elementary particles [2]

electrically charged ( $e^-$ ,  $\mu^-$ ,  $\tau^-$ ) and one corresponding neutrino for each. Generations of quarks each contain two types of flavours. The first generation is composed of up and down quarks, the second is charm and strange, followed by top and bottom. Up, charm and strange have an electrical charge of  $+2/3$ , down, strange and bottom have charges of  $-1/3$ . The particle content of the Standard Model is summarized in Figure 2.1 and the categories into which they can be split will be discussed in greater detail below.

**Bosons:** Gauge bosons arise from symmetry requirements, when imposing local gauge invariance on the Lagrangians of QCD, QED and electroweak interactions. The force each boson mediates is shown in Table 2.1.

The photon is the massless boson of the electromagnetic force. The weak force is

Force	Boson
Electromagnetic	Photon ( $\gamma$ )
Weak	$W^\pm, Z$
Strong	Gluon (g)

Table 2.1: Bosons in the Standard Model

mediated by the charged  $W$  bosons and neutral  $Z$  boson. These acquire mass via electroweak symmetry breaking (EWSB). The Higgs boson also arises as a consequence of EWSB. It is the only boson in the SM to carry no spin - a scalar boson. The breaking of this symmetry splits the massive  $W$  and  $Z$  bosons apart from the massless photon and separates the electromagnetic and weak which appear unified at high energy scales. A final boson, the hypothetical massless graviton, has been proposed to mediate gravity, but this approach faces significant theoretical challenges.

The primary aspect of the SM with which this thesis is concerned is QCD, the theory of strong interactions. It is a field theory that explains how jets originate via the mechanism of hadronization. The QCD Lagrangian is derived by requiring it to be invariant under an  $SU(3)$  gauge transformation. This demand arises from the observation of multiplets of hadrons, with properties that can be explained by the existence of a strong force associated with a colour charge that can take three values. The propagators of this force are eight gluons that couple to colour charge and propagate the strong force between quarks, which also carry colour charge.

### 2.1.1 Dijet Cross Section

The cross section is a measurement of the probability that a specific event will take place. In the case of dijets, for a  $2 \rightarrow 2$  parton process with matrix element  $M$ , the cross section  $\sigma$  is:

$$\frac{E_3 E_4 d^6 \sigma}{d^3 p_3 d^3 p_4} = \frac{1}{2\hat{s}} \frac{1}{16\pi^2} \sum_{\text{spins}} |M|^2 \delta^4(p_1 + p_2 - p_3 - p_4) \quad (2.1)$$

where quantities relating to the two incoming partons are labelled with the subscript 1 and 2 and quantities relating to the outgoing partons are labelled with subscripts 3 and 4.  $E$  is the energy of the partons,  $p$  is their momentum,  $\hat{s}$  denotes the centre-of-mass energy squared of the underlying interaction and  $M$  is the dijet invariant mass.

The cross section is calculated from data using the definition [3]

$$\frac{d^2\sigma}{dp_T dy} = N_{\text{jets}} \mathcal{L} \delta p_T \delta y \quad (2.2)$$

for rapidity  $y$ , number of jets  $N_{\text{jets}}$  (after correcting for detector effects) and integrated luminosity  $\mathcal{L}$ , in a given rapidity and momentum interval  $\delta y$  and  $\delta p_T$ .

## 2.2 Beyond the Standard Model

Despite the success and precision of the Standard Model, a number of observations demonstrate that it is not complete, with the existence of dark matter among the notable omissions. The existence of dark matter was first suggested by Fritz Zwicky in 1933 [4], to explain the observation that visible mass would not exert enough gravitational force to keep galaxies together. Despite thirty years of dedicated experimental searches, the existence of any of the proposed dark matter candidates has yet to be detected. This has constrained the interaction strength via the electromagnetic force - it interacts very weakly, but most likely not at all, via EM. It is possible that the only channel to probe the nature of dark matter is gravitational: but we assume it must interact to some degree, either through weak interaction or some other channel. The possibility remains that it interacts to a degree ATLAS would be capable of detecting. Many theories examining the nature of these processes allow subsequent decays into quark final states, and the dijet searches that are the subject of this thesis allow cross-section limits to be placed on benchmark models [5]–[7].

A second major gap in the Standard Model is the absence of gravity. Several uni-

ifying theories, so-called ‘theories of everything’, have been created which combine all four fundamental forces into one, and in so doing also reconcile the Standard Model with gravity. Among these perhaps the most well-known is string theory, where point-particles are replaced by one-dimensional vibrating ‘strings’. These objects would be so small that to even our most advanced detectors, they are indistinguishable from point particles. String corrections to QCD dijet processes may be detectable within dijet events at ATLAS, since in some versions of string theory additional dimensions allow string masses to drop to the TeV scale. Superstring theory also incorporates supersymmetry, offering a connection between seemingly disparate bosons and fermions.

Current exclusion limits on heavy particles at ATLAS and CMS are shown in Figures 2.2 and 2.3. This includes limits set by dijet searches, but also demonstrates the lack of current efforts to find exotic particles decaying to two gluons, which is one of the aims of this analysis. There are no current searches to which our results for this particular decay mode can be compared.

## 2.2.1 Benchmark Models

### Strings

String theory uses branes to describe the Standard Model [10]. Branes can have dimensions ranging from 0-dimensional to  $p$ -dimensional, where  $p$  can take values up to 9 in some versions of string theory. A brane on which fundamental strings can end is known as a D-brane. A 1-brane is a string. String resonances originate from Regge excitations of quarks and gluons. Tullio Regge treated angular momentum as a complex variable and proved that for a large number potentials, the only singularities in amplitudes were poles. If these occur for positive values of angular momentum, they represent bound states or resonances.

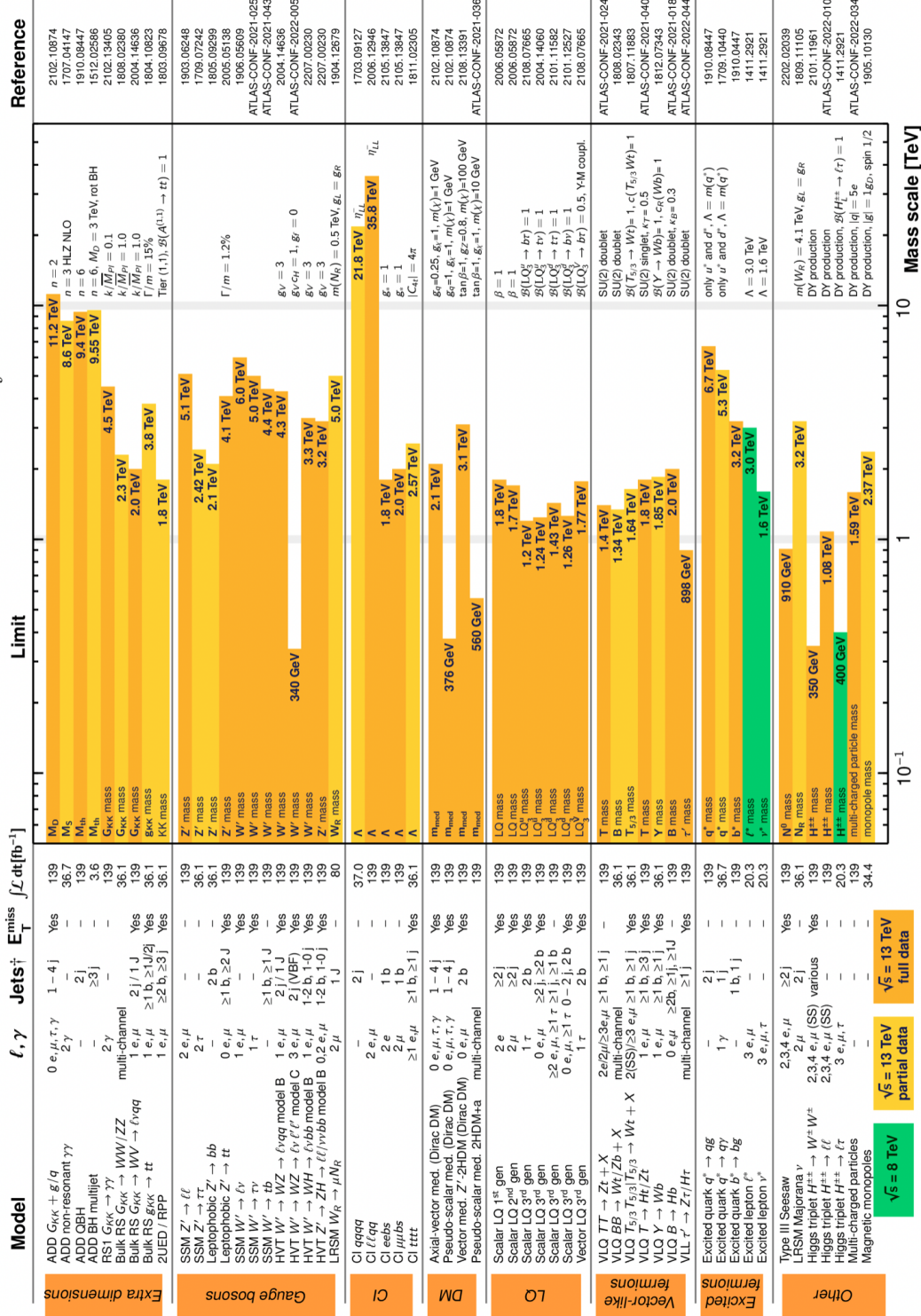
The low mass strings scenarios that would be accessible to the LHC necessitate the presence of open strings stretching between D-branes. Quarks arise from strings stretching at an angle between D-branes, while gluons arise from strings where both

# ATLAS Heavy Particle Searches\* - 95% CL Upper Exclusion Limits

Status: July 2022

ATLAS Preliminary  
 $\sqrt{s} = 8, 13 \text{ TeV}$

$$\int \mathcal{L} dt = (3.6 - 139) \text{ fb}^{-1}$$



\*Only a selection of the available mass limits on new states or phenomena is shown.

†Small-radius (large-radius) jets are denoted by the letter j ( $\nu$ ).

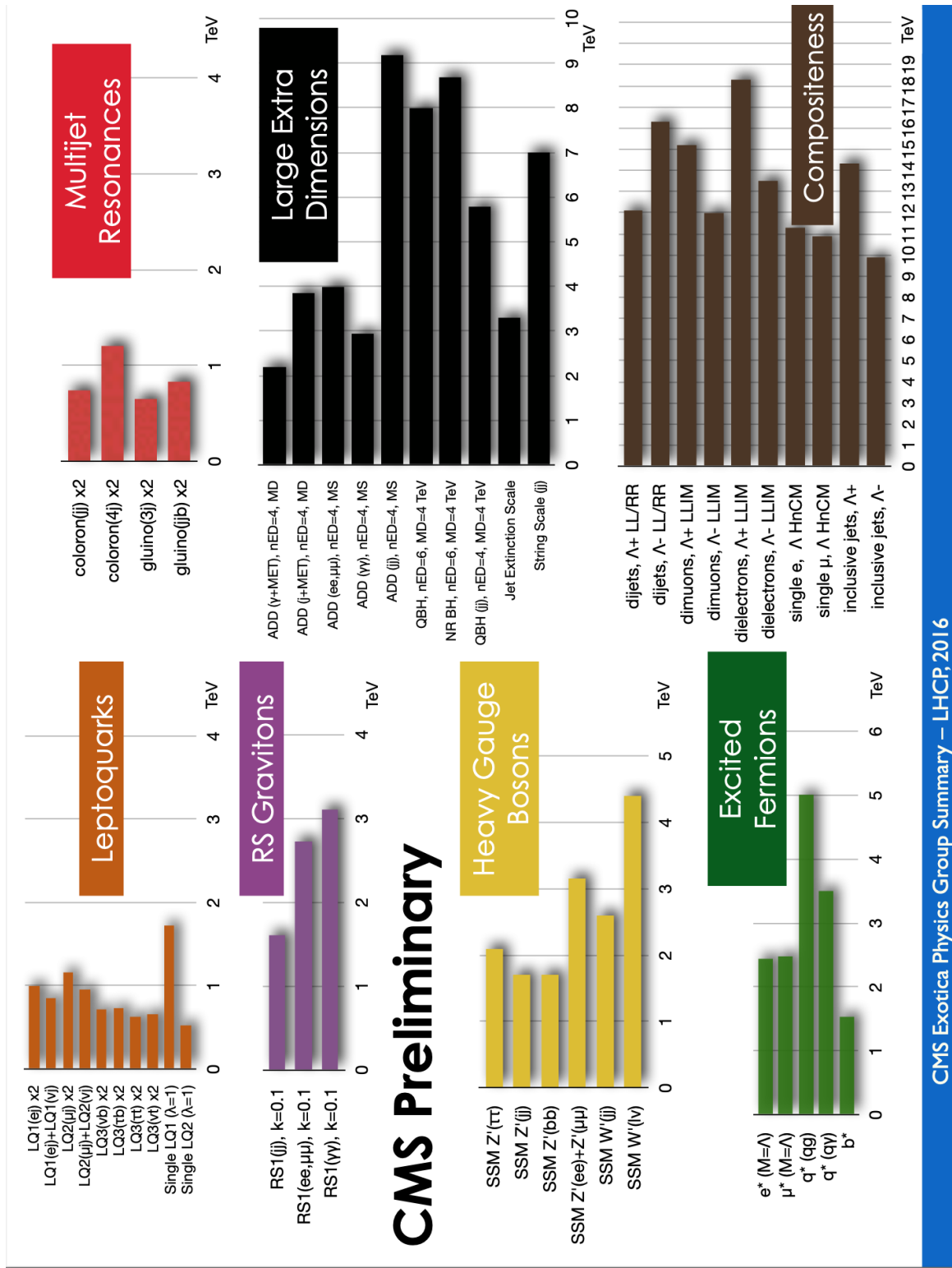


Figure 2.3: Exclusion limits on heavy particles by the CMS Collaboration (Figure by CMS Collaboration [9]).

ends end on the same D-brane. Example dijet mass peaks for the strings model used in this analysis are shown in Figure 2.4.

### Excited Quarks

It is unknown why there are exactly three generations of quarks and leptons, each seemingly identical but heavier copies of the last. This has lead to speculation that they may in fact not be fundamental, and are instead structures composed of bound states of some truly fundamental particles, called preons [11]. Although there are competing composite models one commonality exists: namely, the existence of a new type of strong gauge interaction. A non-Abelian theory incorporating this interaction must be asymptotically free and infrared-safe (these terms are discussed in greater detail in Section 2.4) . Below some compositeness scale,  $\Lambda$ , the new force is strong enough to bind preons into metacolour singlets, some colourless combination as analogously observed in QCD, and this results in the observed quarks and leptons.

Such models also tend to predict that excited states would then exist. These could occur and subsequently decay through gauge interactions, producing a signal accessible to a dijet resonance search. A variety of possible production mechanisms have been posited for proton colliders. While  $q\bar{q}$  annihilation or  $gg$  fusion would seem the most obvious path, predicted cross-sections from both of these are too small to be detectable behind the ordinary QCD and electroweak background. Another possibility would be production when quarks are excited by gluons, or through contact interactions, both of which attain larger corresponding cross-sections.

$$q + \bar{q} \rightarrow q^* + \bar{q}$$

$$g + g, g + q \rightarrow q^*$$

$$q + q \rightarrow q^* + q$$

As an example, a possible Feynman diagram via quark-gluon scattering mechanism

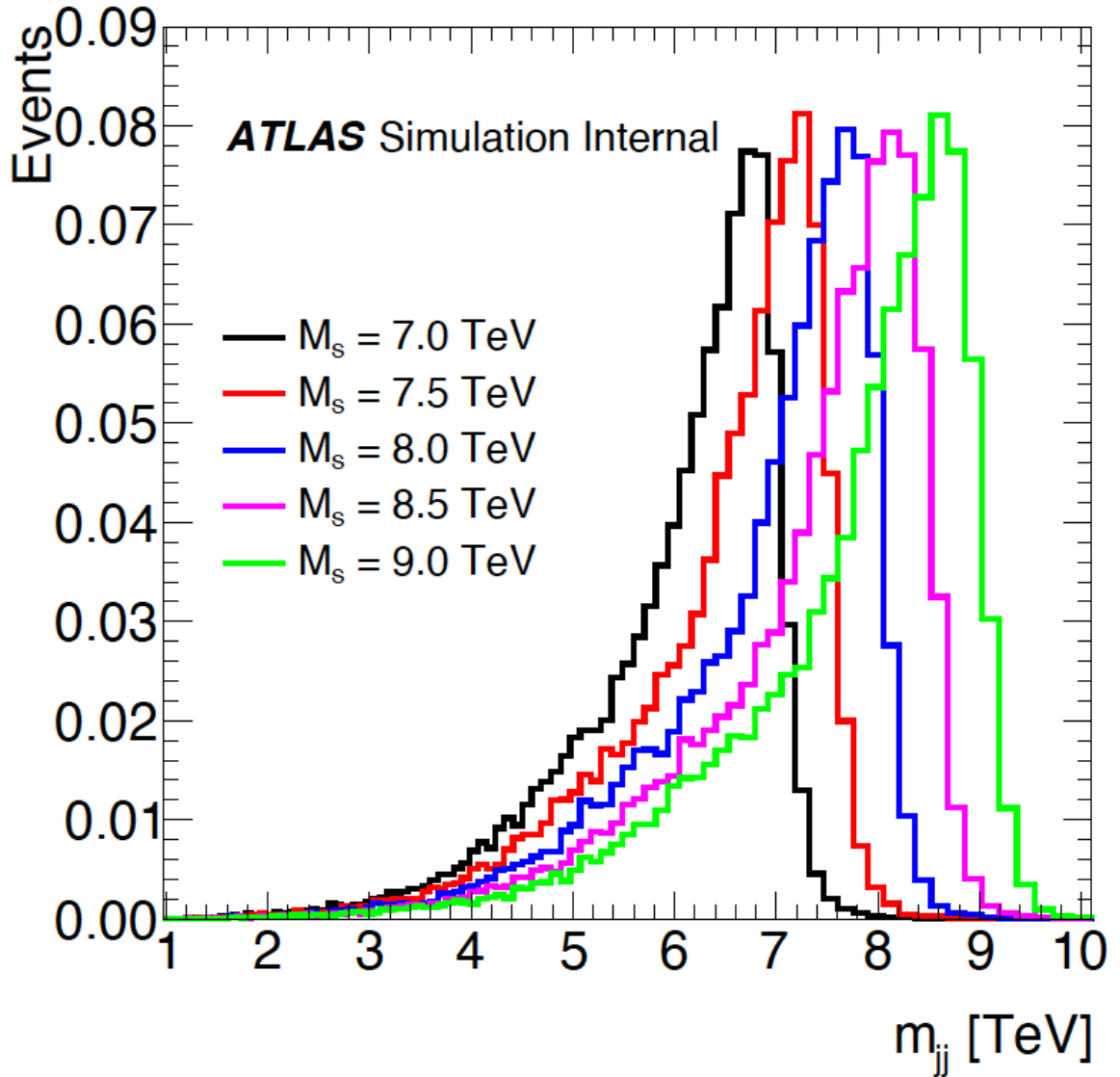


Figure 2.4: Dijet mass (dijet  $m_{jj}$ ) distributions for the strings signal at various masses, generated using the Strings version 1.00 Monte Carlo event generator [10].

to produce excited quarks is shown in Figure 2.5.

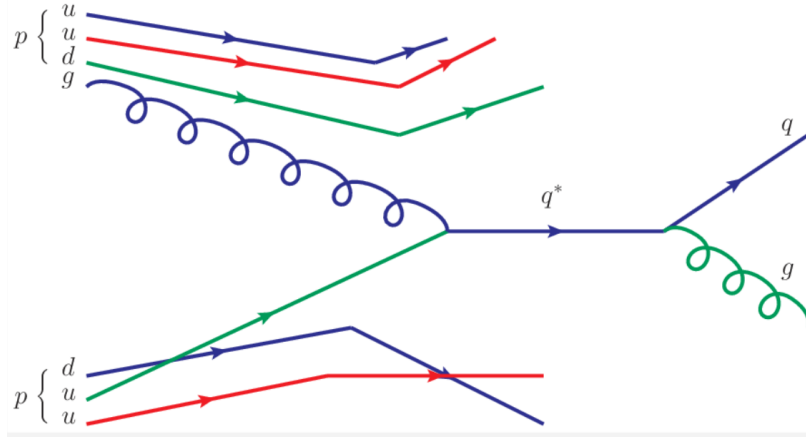


Figure 2.5: Feynman diagram of excited quark ( $q^*$ ) production from quark - gluon scattering [12].

Once produced, excited quarks are predicted to decay to quarks and gluons through gauge interactions. This would result in multi-jet final states. This process has been used to set a common benchmark across previous dijet mass resonance searches [13], with detailed discussion of the theoretical models behind them provided in [14], [15].

For this analysis the  $qg \rightarrow q^*$  model is used, with the excited quark having the following properties: spin 1/2, isospin 1/2, compositeness scale  $\Lambda$  set to the  $q^*$  mass and the coupling constants of SM quarks. These conditions are imposed for simplicity, as no theoretical constraints forbid other values of spin and isospin [15]. Assigning all excited states to  $s = 0$ , isosinglets, allows non-zero masses to exist prior to the breaking of the  $SU(2) \times U(1)$  symmetry. The same is also achieved by assigning left and right-handed components into isodoublets:

$$\begin{bmatrix} u \\ d_L \end{bmatrix}, \frac{u_R}{d_R} \begin{bmatrix} u^* \\ d^* \end{bmatrix}_L, \begin{bmatrix} u^* \\ d^* \end{bmatrix}_R \quad (2.3)$$

These excited  $u$  and  $d$  states,  $u^*$  and  $d^*$ , couple to Standard Model bosons in a vectorlike way. The Lagrangian for this is given in Equation 2.4:

$$L_{\text{gauge}} = \bar{f}^* \gamma^\mu \left[ g_s \frac{\lambda^a}{2} G_\mu^a + g \frac{\tau}{2} W_\mu + g' \frac{Y}{2} B_\mu \right] f^* \quad (2.4)$$

where  $Y$  is the weak hypercharge, which for excited quarks is  $\frac{1}{3}$ ,  $g_s$ ,  $g = e/\sin\theta_W$  and  $g' = e/\cos\theta_W$  are the gauge couplings for the electroweak and strong forces.  $G_\mu^a$ ,  $W_\mu$  and  $B_\mu$  describe the gluon, the SU(2) and the U(1) gauge fields respectively. The  $W$  boson ordinarily couples only to left-handed fermions, but can couple to both left- and right-handed ordinary fermions.

Gauge bosons can also mediate the transition from a left-handed ground state fermion to a right-handed excited state fermion. The effective Lagrangian is given by Equation 2.5

$$L_{\text{trans}} = \frac{1}{2\Lambda} \bar{f}_R^* \sigma^{\mu\nu} \left[ g_s f_s \frac{\lambda^a}{2} G_{\mu\nu}^a + g f \frac{\tau}{2} \cdot W_{\mu\nu} + g' f' \frac{Y}{2} B_{\mu\nu} \right] f_L + H.C. \quad (2.5)$$

for the tensors  $G_{\mu\nu}^a$ ,  $W_{\mu\nu}$  and  $B_{\mu\nu}$  which denote the field strengths of the gluon, the SU(2) and U(1) gauge fields.  $g$  are the strong coupling constants.  $\Lambda$  is the compositeness scale. Then  $f_s$ ,  $f$  and  $f'$  are parameters determined by composite dynamics, predicted to be  $\sim O(1)$ . These parameters can be changed to form factors e.g.  $f_s(q^2)$  to incorporate higher-dimensional operators. The Feynman diagram for this type of interaction is shown in Figure 2.6.

The contact interaction production mode is driven by strong interactions between preons. If the compositeness scale  $\Lambda$  is much larger than the centre of mass energy of the colliding partons, quarks and leptons appear point-like. Below the compositeness scale the four-fermion Lagrangian, in its chirally invariant form, is given by [16]:

$$L_{\text{contact}} = \frac{g^2}{2\Lambda^2} \left[ \eta_{LL} \bar{f}_L \gamma_\mu f_L \bar{f}_L \gamma^\mu f_L + \eta_{RR} \bar{f}_R \gamma_\mu f_R \bar{f}_R \gamma^\mu f_R + 2\eta_{LR} \bar{f}_L \gamma_\mu f_L \bar{f}_R \gamma^\mu f_R \right] \quad (2.6)$$

These interactions would result in multi-jet ( $>2$  jet) signatures in the detector and are thus not directly important to the dijet analysis, however it may be that quark/gluon tagging can also offer benefits to multi-jet searches in future.

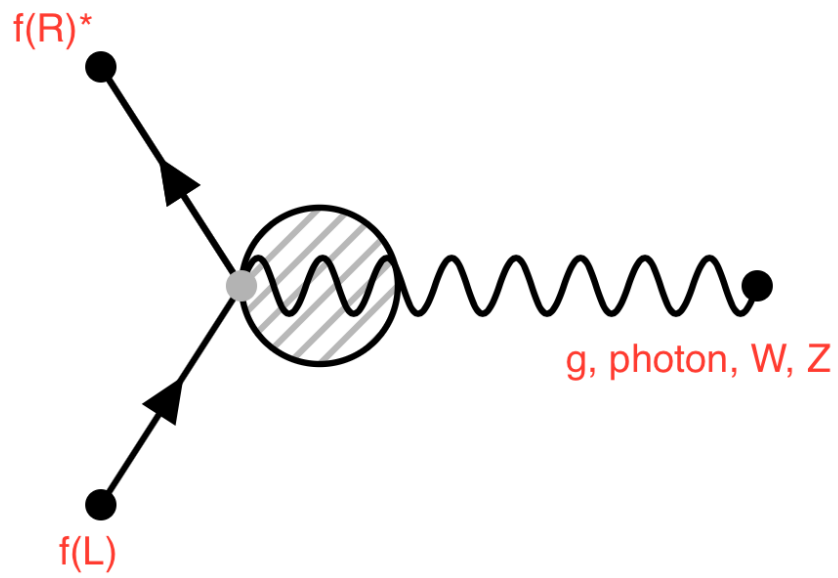


Figure 2.6: Transitions between ordinary and excited fermions via gauge-boson emission.  $f(L)$  denotes a left-handed fermion,  $f(R)^*$  is a right-handed excited fermion. The striped circle denotes the presence of virtual, off-mass-shell particles. The grey circle and black circle at the vertices are equivalent.

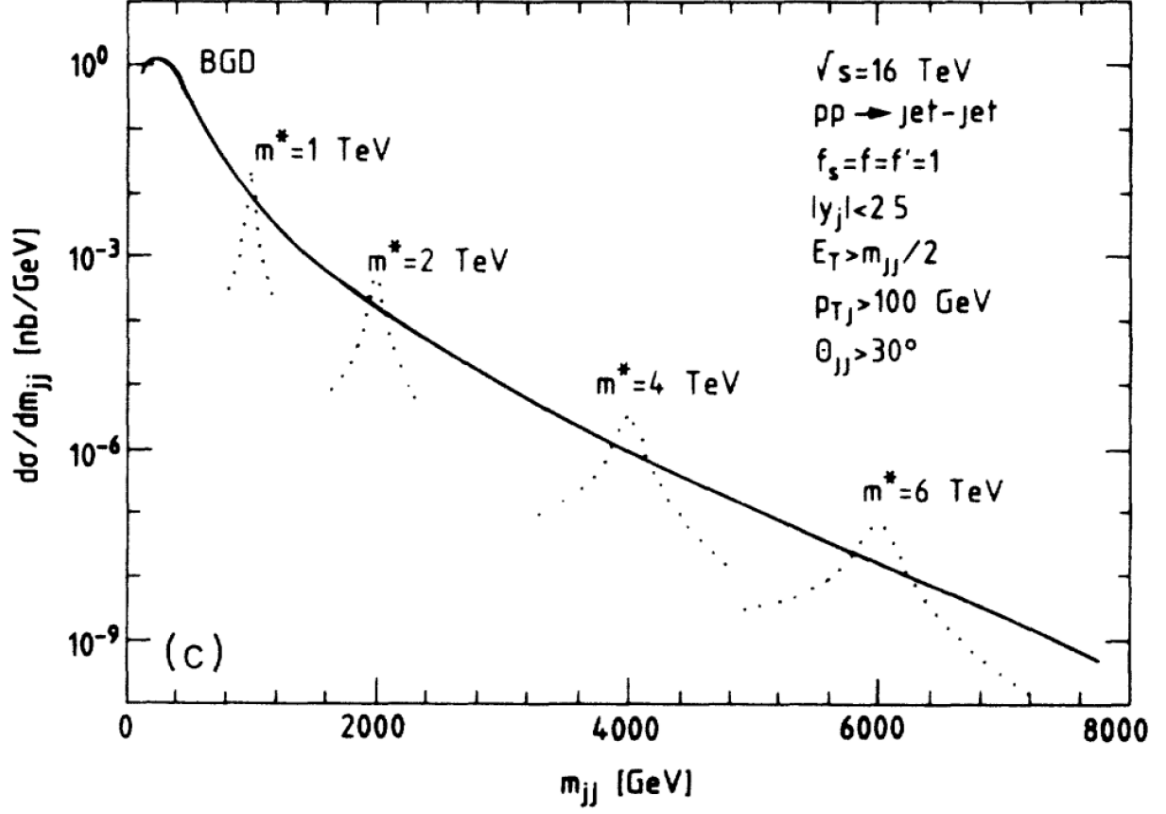


Figure 2.7: The peaks from excited quarks of various masses shown against the Standard Model dijet mass spectrum for pp collisions with  $\sqrt{s} = 16$  TeV. [17]

Since current limits on the  $q^*$  suggest the mass is much higher than the mass of electroweak gauge bosons, the strongest decay mode is to a quark and a gluon:

$$q^* \rightarrow q + g \quad (2.7)$$

where

$$\Gamma(q^* \rightarrow qg) = \frac{1}{3} \alpha_s f_s^2 \frac{m^{*3}}{\Lambda^2} \quad (2.8)$$

The resulting distributions are shown against the standard model dijet mass spectrum, for various values of  $m^*$ , in Figure 2.7.

Example mass peaks for the  $q^*$  model used in this analysis are shown in Figure 2.8.

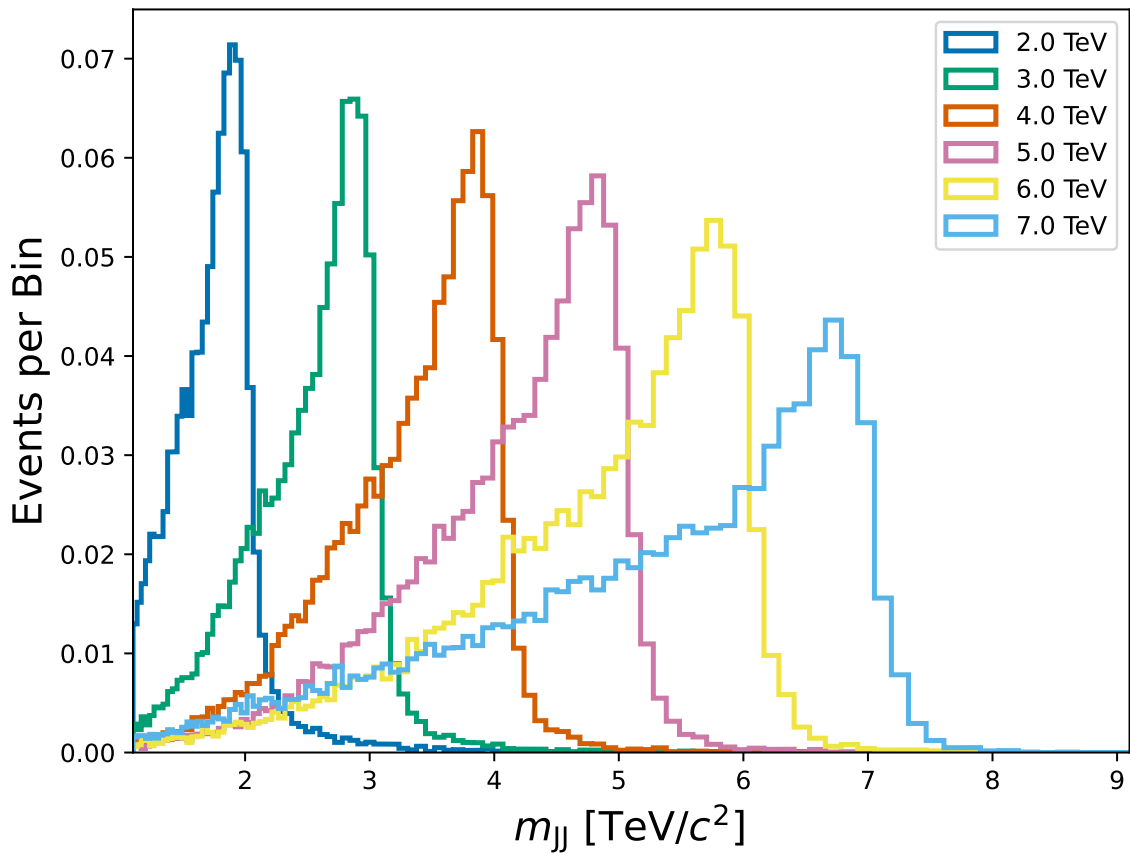


Figure 2.8: Mass distributions for the  $q^*$  signal with the following properties: spin 1/2, isospin 1/2, compositeness scale set to the  $q^*$  mass and the coupling constants of SM quarks.

## Singlet Scalar decaying to two gluons

There are several BSM models which predict novel particles that decay to gluon-gluon final states. Many of these originally arose in response to an apparent bump in the diphoton invariant mass distribution at around  $m_{\gamma\gamma} \sim 750$  GeV observed by Run 2 analyses of both ATLAS [18] and CMS data [19] in 2015 data (interest was considerably dampened following the absence of the excess in 2016 data, and it is now widely considered a statistical fluctuation [20]). However some of the resulting proposed models with  $\gamma\gamma$  final states also predicted preferential decays to two gluons. Despite the dismissal of the resonance, some among the abundance of new models are still of interest in BSM searches.

For example, the model of a pseudo-Nambu-Goldstone (pNG) boson of a new QCD-like theory retains its potential. In this model the pNG boson is produced through gluon fusion and decays into a pair of SM gauge bosons [21]. This is a scalar boson,  $\phi$ , with relevant interaction terms parameterised by

$$\mathcal{L}_{\text{eff}} = \frac{\alpha}{4\pi} \frac{k_\gamma}{\Lambda_\gamma} \phi \tilde{F}_{\mu\nu} + \frac{\alpha_s}{4\pi} \frac{k_g}{\Lambda_g} \phi G_{\mu\nu}^a G^{\tilde{a}\mu\nu} \quad (2.9)$$

where the field strength of the photon is  $F$ ,  $\tilde{F}^{\mu\nu} \equiv \frac{1}{2}\epsilon^{\mu\nu\rho\sigma} F_{\rho\sigma}$ ,  $G$  is the gluon field strength,  $k_\gamma$  and  $k_g$  are dimensionless constants and  $\Lambda_\gamma$  and  $\Lambda_g$  are mass parameters.

The widths of the decays  $\phi \rightarrow \gamma\gamma$  and  $\phi \rightarrow gg$  following the effective interactions from the Lagrangian in 2.9 are [22]:

$$\Gamma(\phi \rightarrow gg) = \frac{\alpha_s^2}{8\pi^3} \frac{k_g^2 m_\phi^3}{\Lambda_g^2} \quad (2.10)$$

$$\Gamma(\phi \rightarrow \gamma\gamma) = \frac{k_\gamma^2 m_\phi^3}{\Lambda_\gamma^2} \frac{\alpha^2}{64\pi^3} \quad (2.11)$$

for scalar boson mass  $m_\phi$ . If we assume that  $\frac{k_\gamma}{\Lambda_\gamma} \sim \frac{k_g}{\Lambda_g}$ , the dominant decay mode is  $\phi \rightarrow gg$ , with no decays to a  $qg$  or  $qq$  final state.

A model-independent motivation for di-gluon resonances is that at high  $m_{jj}$  the

background is dominated by valence quark scattering and thus gluon tagging could be particularly effective. For this analysis, we have simulated SU(3) singlet scalar production and decay using Pythia, and we refer to this particle as the  $H'$ . Example mass distributions are shown in Figure 2.9.

## 2.3 The ATLAS Detector

The Large Hadron Collider (LHC) is a two-ring particle accelerator designed to collide bunches of protons. The beam pipes are 100 m underground and 27 km long. Before entering the LHC, protons are accelerated first in a linear accelerator (called LINAC 2) and then in two synchrotrons to boost their energy up to 450 GeV. There are four points at which the beams may cross, with a detector at each one along with an associated collaboration. The four main experiments are the Compact Muon Solenoid (CMS) experiment [23], A Toroidal LHC ApparatuS (ATLAS) experiment [24], A Large Ion Collider Experiment (ALICE) [25] and the Large Hadron Collider beauty (LHCb) experiment.

There are two key figures of merit used to describe the LHC's performance that are particularly important to ATLAS [26]. These are the centre-of-mass energy and luminosity, described in Sectionn 2.3.1 and 2.3.2. The performance of all components of the ATLAS detector is described in detail e.g. in [27],[28].

### 2.3.1 Luminosity

The instantaneous luminosity  $\mathcal{L}$  is defined as the number of particles passing each other per unit time at the interaction point, through a unit transverse area. It isn't strictly the interaction rate, since it describes how many particles pass through a given space in a given time - without putting a figure on how many of those will actually interact. However, a higher luminosity will clearly lead to a higher interaction probability. Hence luminosity is an indicator of the statistics available for analysis.

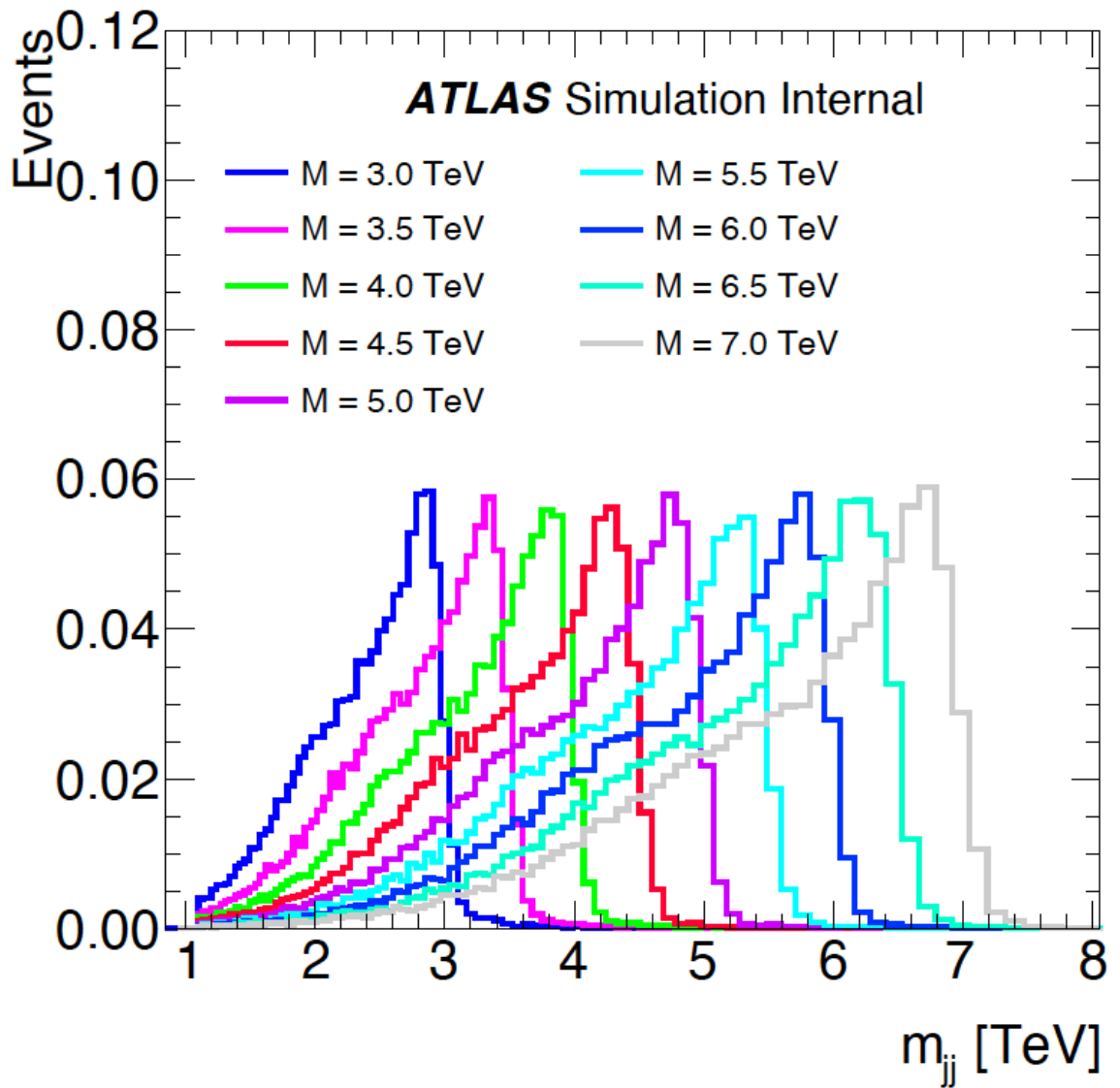


Figure 2.9: Signal Shapes for the  $H'$  at various mass points. Simulated SU(3) singlet scalar production and decay using Pythia

Luminosity depends purely on the beam parameters, and is given by (for a Gaussian process):

$$\mathcal{L} = F \frac{N_b^2 n_b f_{\text{rev}} \gamma_r}{4\pi \epsilon_n \beta^*} \quad (2.12)$$

where  $F$  is the geometric luminosity reduction factor (accounting for the fact collisions are not head-on),  $N_b$  is the number of particles in each of  $n_b$  bunches per beam.  $f_{\text{rev}}$  is the revolution frequency of bunches,  $\beta^*$  is the beta function at the collision point,  $\epsilon_n$  is the normalized transverse beam emittance (a measure of the spread of the positions and momenta of the protons) and  $\gamma_r$  is the relativistic gamma factor.

The instantaneous luminosity can then be used to calculate the event rate  $N_{\text{event}}$ , i.e. the number of scatterings per unit time, which is given by:

$$N_{\text{event}} = \mathcal{L} \sigma_{\text{event}} \quad (2.13)$$

where  $\sigma_{\text{event}}$  is the cross section of the process for which  $N_{\text{events}}$  has been collected.

Luminosity increased significantly during Run 2, peaking at  $\mathcal{L} = 19 \times 10^{33} \text{ cm}^{-2} \text{ s}^{-1}$  [29] (up from  $5 \times 10^{33} \text{ cm}^{-2} \text{ s}^{-1}$ ), due to an increase in both  $N_b$  and  $n_b$  and improved beam focusing.

## Pileup

With such high luminosities, it is inevitable that along with any collision of interest, additional proton-proton events will occur as background. Over the lifetime of the LHC this issue has grown from a maximum of 5 collisions per bunch crossing in 2011 [30] to 60 in Run-2 [31], with a predicted 200 from 2026 onwards at the High Luminosity - LHC [32]. In addition, the detector subsystems often have time resolution lower than the 25 nanoseconds between events, meaning data from two separate bunch crossings overlaps. Between them this ensures every physics object is affected

by pile-up to some degree, and dealing with this is a critical challenge for analyses in ATLAS. Pileup is separated into two major categories, in-time (concurrent collisions in a bunch crossing) and out-of-time (products of a previous or subsequent bunch crossing being detected in the present event).

The number of collisions per bunch crossing is given by

$$\mu = \frac{\sigma_{\text{inelastic}} \mathcal{L}_0}{n_b f_r} \quad (2.14)$$

for pileup  $\mu$  in a beam with  $n_b$  bunches per beam, inelastic cross-section  $\sigma_{\text{inelastic}}$ ,  $f_r$  the revolution frequency and instantaneous luminosity  $\mathcal{L}_0$ .

### 2.3.2 The ATLAS Detector

ATLAS stands for A Toroidal LHC ApparatuS. This is a general-purpose, cylindrical detector with the largest volume of any detector ever built for a collider. The ATLAS collaboration is the largest at CERN and one of the largest ever attempted globally, with almost 3,000 scientific authors. With the help of various layers of subsystems, it aims to gather as much information as possible about collision products radiating from the interaction point. A diagram of the ATLAS detector is shown in Figure 2.10 [33].

The subsystems are wrapped concentrically around the collision point, a geometry demanded by the lack of preferred directionality in the  $pp$  interactions. There is thus a need to achieve as close as possible to  $4\pi$  radians of solid angle coverage.

In order to describe the functions and operation of the subsystems, it is necessary to first discuss the co-ordinate system used.

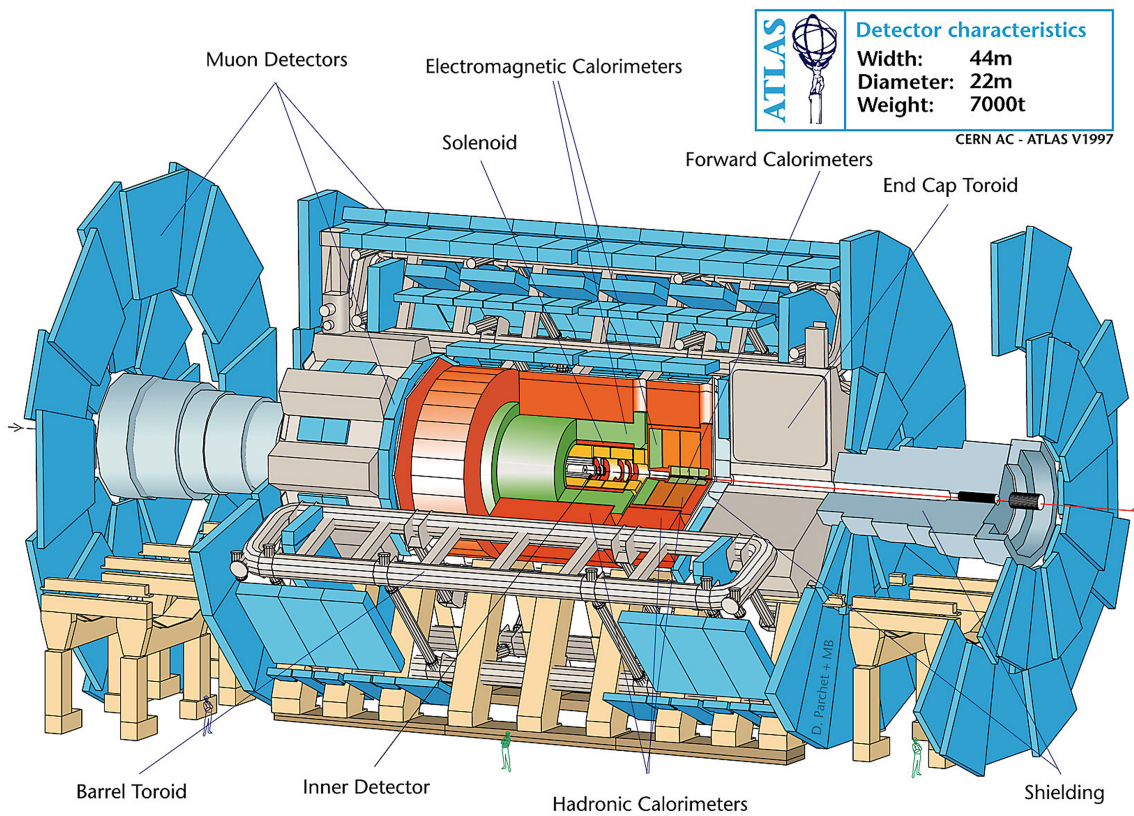


Figure 2.10: Schematic diagram of the ATLAS detector. The function of each component is summarised in the subsequent sections [34].

### 2.3.3 Coordinate System

The co-ordinate system is defined with the IP as the origin. The  $z$ -axis then runs along the beam line, with the perpendicular  $x - y$  plane often referred to as the transverse plane. The positive  $x$ -axis points to the centre of the LHC, while the positive  $y$ -axis is directed up towards Earth's surface. Along the beam line the positive and negative sides are referred to as the 'A' (standing for 'airport' - this side points towards Geneva airport) and 'C' (Crozet - or possibly Charly's pub) sides respectively. Polar coordinates are also routinely used, the cylindrical symmetry of the detector making this an efficient system. In this case the radial distance  $r$  labels the distance from the beam line while the azimuthal angle  $\phi$  is defined around the  $z$ -axis, aligning  $\phi = 0$  with the positive  $x$ -direction. The polar angle  $\theta$  is the angle from the positive  $z$ -axis such that  $\theta = 0$  is parallel to the beam line.

Having defined these we can use them to describe several further useful quantities. Firstly the rapidity  $y$  is given by:

$$y = \frac{1}{2} \ln \left( \frac{E + p_z c}{E - p_z c} \right) \quad (2.15)$$

The difference between the rapidities of two particles is invariant with respect to Lorentz boosts along the beam axis.

The polar angle is often preferentially described by pseudorapidity  $\eta$ , where:

$$\eta = -\ln(\tan \theta) \quad (2.16)$$

$\eta$  then has the value 0 for particles with a trajectory perpendicular to the beam and can be both positive and negative otherwise, and for highly relativistic particles (in the limit where the particle travels close to the speed of light, or equivalently if the mass of the particle is negligible and approximates to zero)  $y \sim \eta$ .

### 2.3.4 The Inner Detector

The first and innermost layer of ATLAS is the Inner Detector (ID). It covers the region  $\eta_{\text{det}} < 2.5$  and is made up of multiple components. Since this layer is exposed to the highest flux of particles, these components must all be designed to cope with the most radiation intensive environment in ATLAS. In order of closest to the interaction point to furthest, these components are the silicon pixel detector and the silicon-strip semiconductor tracker, which are grouped into the ‘inner tracker’, and the transition radiation tracker (TRT).

#### Inner Tracker

Silicon semiconductor tracking detectors were chosen to provide high energy and spatial resolutions, to aid in the resolution of individual particle tracks. The 1744 pixel detector modules, each  $250 \mu\text{m}$  thick, give exceptionally fine granularity. The charge deposited in any one pixel has units of Time-over-Threshold (ToT) and a granularity of 25 ns. There are roughly 80 million channels to read out from just the pixel detector, a significant data processing challenge. By the end of 2012, just 5% of these modules were inactive, with most new faults appearing after interventions or after cooling or power was rapidly switched off. The remaining detectors delivered 99.9% good quality data in the 2012 run [35]. Data used in this analysis passed all quality checks. In the barrel region these have a concentric cylindrical geometry, with perpendicular disks in the end-cap. During the first long shutdown the insertable b-layer (IBL) was placed near the new thinner beryllium beam pipe. This gave coverage at distances down to just 3mm from the pipe itself.

#### Transition Radiation Tracker

The TRT is composed of xenon drift chambers, with a smaller percentage of both carbon dioxide and oxygen. A track hit in one of the drift tubes is due to the induced current produced when gas mixture is ionised, and the resulting electrons drift to the

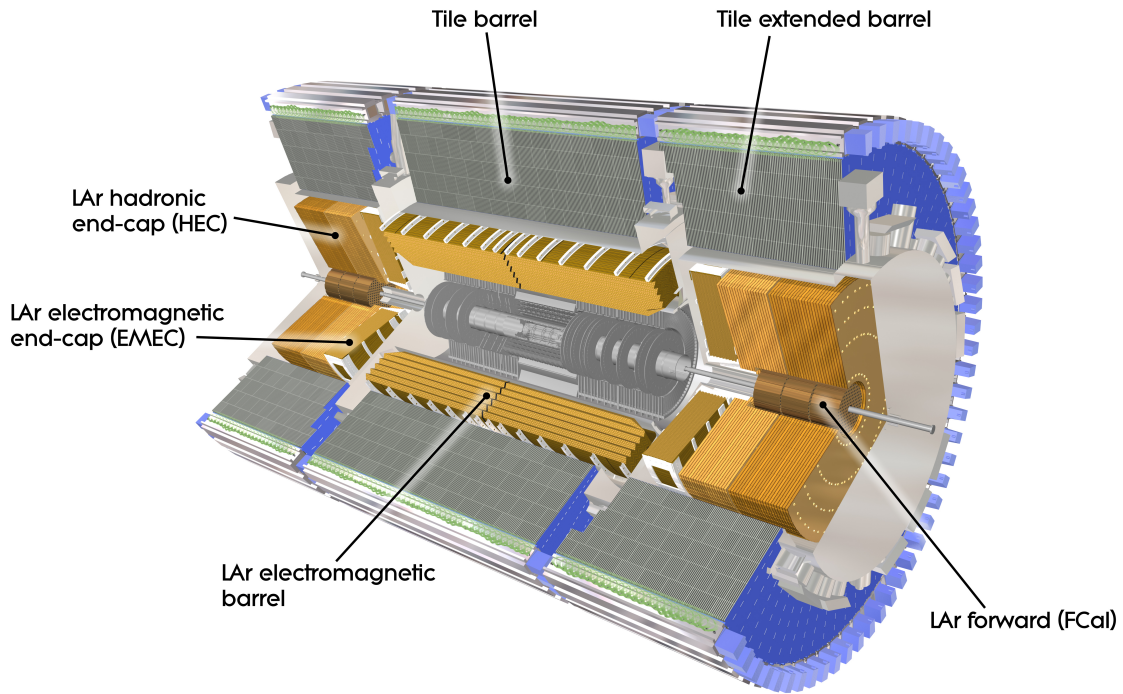


Figure 2.11: A computer generated image of the ATLAS calorimeter [36]

center wire of the straw. The current is detected and read out, with on average 36 hits per track. Only  $(r - \phi)$  information is provided by this tracker. The hit resolution is  $130 \mu m$ , significantly worse than the pixel and strip detector, but it somewhat compensates for this by the large number of hits per track, allowing for much longer measured track lengths. The energy of the transition radiation produced depends on the mass of the particle producing it, which facilitates particle identification.

### 2.3.5 Electromagnetic Calorimeter

Outside the ID sits the electromagnetic calorimeter (EMC). It is composed of alternating lead absorbing plates and liquid argon layers between electrodes with high voltage differences. Its function is to measure the properties of and contain showers from electrically charged and neutral particles. The detector is shown in Figure 2.11.

The alternating layers of active (argon) and passive (lead) materials are a feature

common to all sampling calorimeters. Passive material interacts with incident particles to begin a showering process, with the active material measuring the flux of particles in the shower. Calorimeters are designed to fully contain the particles that interact within them. Kapton electrodes accelerate and collect the electrons then transmit the resulting pulse to readout electronics.

The EMC consists of a barrel part that provides coverage of the region up to  $|\eta| < 1.475$ , and two end caps for  $1.375 < \eta < 3.2$ . The barrel region is situated behind the superconducting central solenoid and has an accordion geometry that provides full azimuthal symmetry. It is 3.2 m long with an inner and outer diameters of 2.8 m and 4 m respectively. Radially the system is split into three concentric layers, which have read-outs with different granularity. The structure is shown in Figure 2.12.

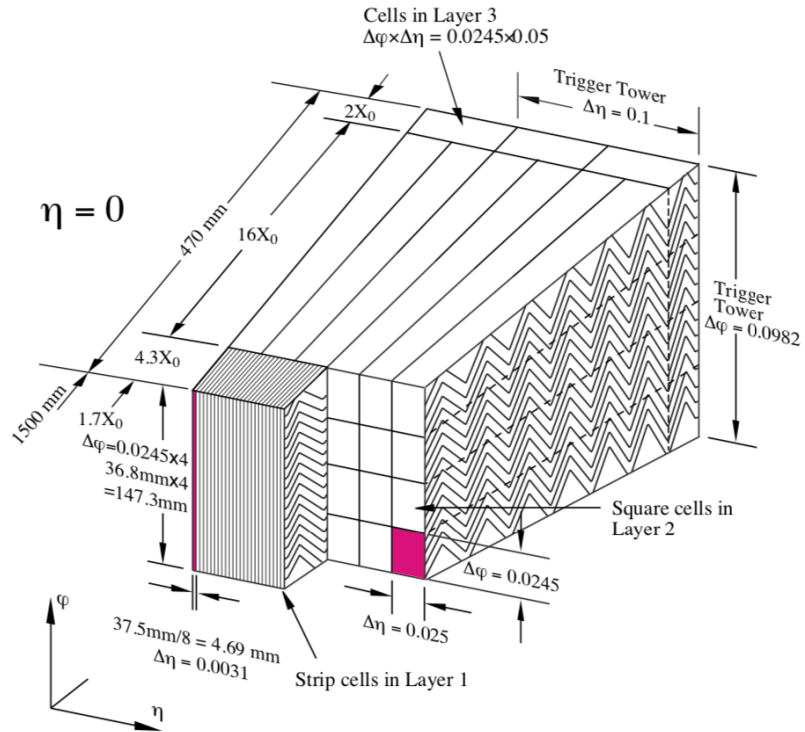


Figure 2.12: A barrel module where the different layers are visible. The granularity of the layers in  $\eta$  and  $\phi$  is also shown [37].

The total depth of the calorimeter varies from  $22 X_0$  to  $33 X_0$  depending on the  $\eta$  value.

### 2.3.6 Hadronic Calorimeter

The hadronic calorimeter is outside the EMC and measures the energy of the hadrons that were not captured by the thinner but higher resolution EMC. Only  $\sim 2/3$  of a hadronic shower is contained within the EMC. Hadronic showers have different characteristics to those generated by electromagnetic particles, driven purely by QED, because of additional strong force interactions. This means some energy is always required for nuclear breakup along with an EM component, making them complex and difficult to model. They are broader (i.e. less localised) and fluctuate significantly on an event-by-event basis, which partly compensates for the reduced granularity compared to the EMC.

These differences necessitate a slight design differences between hadronic and electromagnetic calorimeters. The hadronic calorimeter has three sub-modules: the tile calorimeter (barrel region), the the LAr hadronic end cap and the LAr forward calorimeters (in the same cryostats as the EMC end-caps). The absorbing layers require significantly greater thickness. Liquid argon and plastic scintillating tiles are alternated, with the argon measuring energy deposited in the form of EM showers and nuclear ionisation. The 'invisible' energy put into nuclear breakup is accounted for by calibration. The plastic scintillator emits UV light when molecules excited by incoming particles then de-excite.

**TileCal:** A sampling calorimeter alternating steel absorber (passive material) and scintillating tiles (active material). These materials are present with a ratio of  $\sim 4.7:1$ . Similar to the EMC, the TileCal is split radially into three layers of different thicknesses: for  $|\eta| < 1$  they are 1.5, 4.1 and 1.8 interaction lengths respectively, for  $1 < |\eta| < 1.7$  they are 1.5, 2.6 and 3.3 interaction lengths thick. The UV light produced by each interaction is measured by two optical fibres installed at the edges

of each tile. These convert the signal to visible light, allowing PMTs to be used for readout.

**LAr Hadronic End-cap (HEC):** This calorimeter is located directly behind the end-caps of the EMC and covers the region  $1.5 < |\eta| < 3.2$ . It has a planar geometry. It is made by alternating copper plates with liquid argon layers 8.5 mm thick. Again the signal originates in the active liquid argon layer.

**LAr Forward Calorimeter (FCal):** Sharing the same end-cap cryostats as the EMC and HEC, the FCal is closest to the beam pipe and covers the range  $3.1 < |\eta| < 4.9$ . It is  $\sim 10 X_0$  deep and has three sub-modules, each 45 cm thick. The active material for all three sub-modules is liquid argon, with passive materials of copper to optimise it for EM measurements, while tungsten optimises the other two for hadronic interactions. The use of LAr is particularly beneficial in forward regions where particle fluxes are high, as it is highly resistant to radiation and because of the relative ease of replacing the liquid should serious performance degradation occur.

### 2.3.7 Muon Spectrometer

The outermost section of the ATLAS experiment is the muon spectrometer (MS). It covers the region  $|\eta| < 2.7$  [38] and detects muons with momentum greater than 3 GeV, and aim for precision measurements of momenta from there up to a few TeV - in this energy range, muons lose relatively little energy via ionisation and can pass through the calorimeters. Precision momentum measurements are achieved via the magnetic fields present in the detector, with a goal of 10% resolution on 1 TeV tracks. With a sagitta of  $\sim 500 \mu\text{m}$ , this is a significant challenge. Precision tracking in the barrel region is achieved with Monitored Drift Tubes (MDTs), tubes arranged in cylindrical layers around the beam axis and filled with a mixture of argon and carbon dioxide, both in gaseous form. In the forward region the high flux necessitates a smaller drift time and greater radiation hardness, and MDTs are replaced with

Cathode Strip Chambers (CSCs). These multiwire chambers with cathode planes have a significantly smaller drift time than MDTs and can cope with high counting rates up to  $\sim 1000 \text{ Hz/cm}^2$  [39].

The muon spectrometer also includes trigger chambers. Muons can be indicative of  $W$ ,  $Z$  or Higgs decays, and their presence therefore signals a potentially interesting event. For the detector to provide a trigger, its response must be extremely fast, and spatial resolution is sacrificed to achieve this. Again the approaches to this differ between the end cap and the barrel, since at fixed transverse momentum, a particle with higher pseudo-rapidity is in general more energetic. This results in less bending by the magnetic field. In the barrel region the trigger chambers are composed of doublets of resistive plate, covering the region  $|\eta| < 1.05$  and achieving a spatial resolution of 10 mm in both  $z$  and  $\phi$ . In the end-caps these are replaced by Thin Gap Chambers (TGCs) with spatial resolution of 2 – 6 mm.

Although in theory only muons should leave tracks in the MS, with all other particles showering and being contained in the calorimeters and neutrinos simply passing through undetected, high energy hadronic showers can be very elongated and may leak into the MS. This effect is known as punch-through, and results in a background to tracks from muons.

### 2.3.8 Trigger System

The volume of data produced by the LHC in Run 2 would be impossible to store, with bunches colliding every 25 ns. Trigger and data acquisition (DAQ) systems become exceptionally important. Triggering is the process of deciding which subset of potentially interesting events should be retained with all other data discarded. ATLAS uses a hardware based level-1 trigger (L1T) and follows this with a software based high-level trigger (HLT). Within  $2.5 \mu\text{s}$ , a subset of detectors is used to decide whether to keep or discard an event [40].

The L1T is present in both the calorimeters and the MS. It looks for high transverse momentum particles and events with large missing transverse energy, suggesting high momentum neutrinos are present. Muons set off the trigger in the previously described resistive plate chambers and thin gap chambers in the muon spectrometer. High  $p_T$  jets, electrons,  $\tau$  decays and photons are detected by the reduced-granularity calorimeters. A central processor collects the information from both L1 systems and passes events according to criteria set in the trigger code on to the HLT. Events of interest are associated with their  $\eta$  and  $\phi$  coordinates, which define a Region Of Interest (ROI) [41]. Based on these ROIs the HLT does a full read-out of all detector subsystems at the relevant coordinates. This software-based trigger requires a farm of 40,000 CPUs [42].

L1 trigger items and HLT algorithms, which apply kinematic selections to the preliminary objects they are passed, work together to form 'trigger chains'. There are different chains depending on whether leptons, jets or photons are the target, and once developed these chains are often used by multiple analysis groups within ATLAS. Further controls can be applied to the trigger rate in the form of a pre-scaling factor  $N$ , where the probability of an event passing the trigger is  $1/N$ .

## 2.4 Jets and Jet Phenomenology

The most commonly produced collision products at hadron colliders are jets [43]. While this offers excellent opportunities for both Standard Model and BSM measurements, it also presents challenges, notably the large background which is consistently present. The origin of jets is explained by Quantum Chromodynamics (QCD). It describes the interaction of quarks based on their possession of a conserved quantity labelled color charge, associated with the strong force. Gluons also carry this charge and mediate the strong force.

Free particles that are not color neutral have not been observed. Color neutrality is achieved by a combination of either color with anti-color, or by equal amounts of all

three colors. This prohibits the existence of individual quarks. The requirement for such bound states is known as color confinement. In order to enforce this, the strong force coupling constant must increase as quarks become more distant from each other, a consequence of the self-interaction of gluons. This is in direct contrast with electric fields, where rapid decreases in the force are observed at increasing distances. Instead in QCD a flux tube forms in the gluon field, keeping the force at a constant magnitude until the formation of a new quark-antiquark pair becomes energetically favourable. Conversely at very short distances, the strong force coupling constant undergoes such rapid decreases that quarks behave as free particles to a good approximation. This counterweight to confinement is known as asymptotic freedom.

Jets are an expression of confinement, occurring when enough energy is poured into the gluon field to repeat the process of  $q\bar{q}$  production many times over. The resulting spray of highly collimated and color neutral particles is called a jet, with the process itself known as hadronisation. Underlying this event are an abundance of low  $p_T$  interactions between the hadronic remnants of the original collision. There is no method by which these can be unambiguously separated from the products of hadronisation. Of specific interest in this analysis are jet pairs, which primarily result from  $2\rightarrow 2$  parton (constituents of hadrons) scattering. QCD provides a prediction for the invariant mass of dijets, with the expectation of a monotonically decreasing and smooth spectrum [44].

Simulations of the processes underlying jet formation are based primarily on one of two hadronisation models: the cluster model and the string model.

1. Cluster Model - gluons split non-perturbatively into  $q\bar{q}$  pairs after the initial ‘preconfinement’ stage of showering, and are then split again into a quark-antiquark or anti-diquark-diquark pair with the same kinematics. They are assumed to form isotropically decaying clusters that become hadron pairs. This model is used in the Sherpa [45] and Herwig [46] event generators.

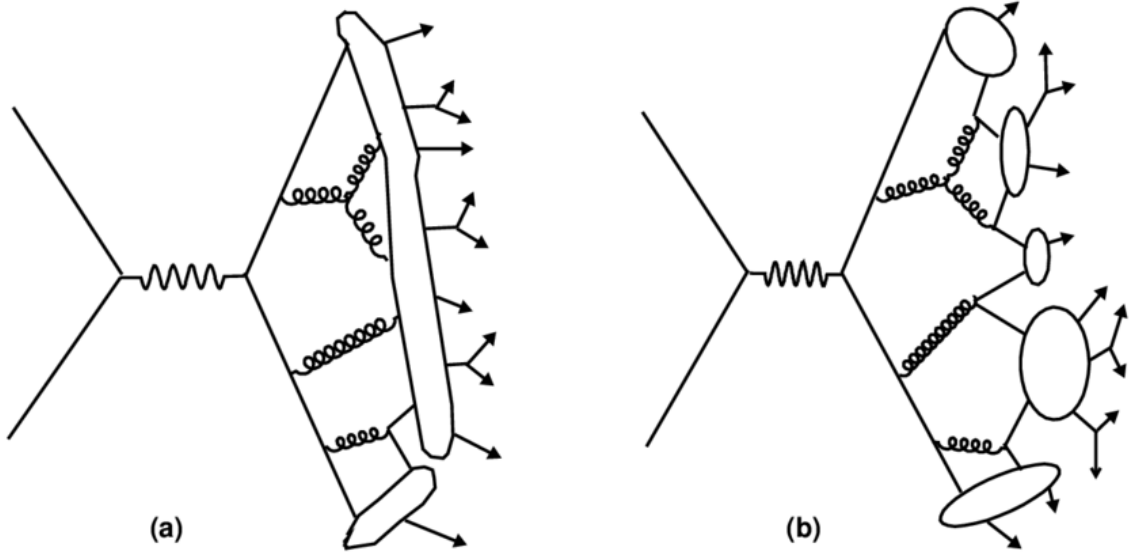


Figure 2.13: Graphical representations of (a) the String model of hadronisation and (b) the Cluster model of hadronisation of a  $q\bar{q}$  pair [48][49].

2. String Model - all but the highest-energy gluons are treated as connected by a relativistic gluon ‘string’. As the separation increases the potential increases linearly, and for the matrix elements:

$$|M(g\bar{q} \rightarrow h_1\dots h_n)|^2 \propto e^{-bA} \quad (2.17)$$

where  $h_1\dots h_n$  are the hadrons created and  $A$  is the spacetime area swept out by the string. It is more suited to describing baryon production than the cluster model, and is used in Pythia [47].

The models are represented graphically in Figure 2.13.

The Pythia generator for this analysis is based on a type of string model called the Lund String Model [50]. It applies the symmetric fragmentation function which is of the form Equation 2.18:

$$f(z) = \frac{(1-z)^a}{z} \exp\left(-\frac{bm_{\perp}^2}{z}\right) \quad (2.18)$$

where  $m_{\perp}$  is the hadron transverse mass and  $z$  is the longitudinal lightcone fraction

and the remaining parameters are free fit parameters to be tuned to data. Transverse mass is defined as

$$m_T^2 = E^2 - p_z^2 \tag{2.19}$$

where  $z$  is the direction along the beam pipe. This is a useful quantity to define as it is invariant under a Lorentz boost along the  $z$  axis.

### Jet Reconstruction algorithms

Grouping the products of collisions into jets can often be far from straightforward, and in practice the definition of a jet in a collider is somewhat ambiguous. Of course the partons themselves cannot be detected, nor can the process of hadronisation be observed. For these we rely on theory and modelling. It is the stable products of hadronisation that produce topological clusters of energy in the calorimeters. The motivation for proceeding despite this difficulty is that defining jets mitigates the need for observables sensitive to the chaotic dynamics within jet processes. Many jet algorithms exist and the decision on which to use is influenced primarily by the type of information that is to be extracted from the jet. There are some common requirements of a jet algorithm; the number of jets observed, along with their energy and momentum, should reflect the particles from which they originated. For two jets generated by a quark-antiquark pair for example, their combined four-momenta should be close to the momenta of the initiating  $q\bar{q}$  pair [51].

The first algorithm to address the problem was the Stermann-Weinberg jets algorithm [52]. It works by classifying an event as having two jets if the total energy of the hadrons produced, apart from at most a fraction  $\epsilon$ , is contained inside two cones with an angular half-width  $\delta$ . The presence of parameters which may be varied to change the fraction of hadrons included in each jet is a feature common to all jet algorithms. Stermann-Weinberg jets also have a property which is not intrinsic to all such algorithms; the fraction of events classified as dijet events is well-defined, and

predictions may be obtained from relativistic quantum mechanics and QCD. This feature is a result of the fact the algorithm is infrared and collinear (IRC) safe (discussed in more detail in subsection 2.4), which is one of the key requirements for a ‘good’ jet algorithm, as set out in the Snowmass Accord. This document specified that a good jet algorithm should [53]:

1. Be simple to implement in an experimental analysis,
2. Be simple to implement in theoretical calculations,
3. Be defined at any order of perturbation theory,
4. Yield finite cross sections at any order of perturbation theory,
5. Yield a cross section that is relatively insensitive to hadronization.

IRC safety guarantees that the final three are satisfied. Point 1 is a very practical issue dealt with on an experiment-by-experiment basis. Point 2 is generally not restrictive, since most QCD calculations are done by adopting a numerical approach via Monte Carlo procedures. But requiring some degree of approachability via an analytical approach can be beneficial, in terms of allowing the procedure and properties of the algorithm to be understood. There is no conceptual problem with allowing an algorithm to calculate particle momenta, but in a particle-dense environment the speed of the algorithm can become an issue.

### **Infrared and Collinear Safety**

Consider the jets just before the quarks and gluons hadronize. In QCD, the probability a gluon with zero energy will be emitted approaches infinity. This is referred to as a soft divergence - ‘soft’ is used to describe a particle with much smaller than the typical energy of other particles of that type. An infinite result also arises if a quark or gluon splits into a pair of parallel partons, and this is known as a collinear

divergence. These processes are illustrated in Figure 2.14.



Figure 2.14: On the left is a diagram illustrating collinear emission of a gluon, while on the right a soft gluon is emitted [51].

The presence of singularities is highly undesirable, and thus we require jet algorithms to be Infrared and Collinear (IRC) safe. IRC safety is the property that if an event is modified by the addition of either of these processes, the resulting set of jets should remain unchanged. To achieve this, the divergence must be resolved. Since different types of quantum fluctuation lead to divergent loop matrix elements with the opposite sign, taking into account the combination of these processes often leads to the infinities cancelling each other out. An example of such a quantum fluctuation would be the emission and re-absorption of a gluon before it is observed.

IRC safety is made indispensable by the fact that a hard parton, i.e. a parton with high transverse momentum compared to the proton mass, will undergo many collinear splittings during the fragmentation process. In addition to this there will always be some accompanying emission of soft particles. These occur randomly, and even average properties are unpredictable. In constructing jets, the aim is to be able to view events without sensitivity to these behaviours; in other words, for them to be IRC safe objects. Accurate SM predictions at ATLAS rely on this quality; where it is not satisfied, tree-level splittings and loop diagrams can lead to different sets of jets which do not cancel, breaking point 4 of the Snowmass conditions. Specifically for Stermann-Weinberg jets with a given value of  $\epsilon$  and  $\delta$ , a zero-energy gluon event won't change the interpretation as a dijet event. The same is true of collinear splitting, because infinities caused by the emission of real gluons and virtual corrections will

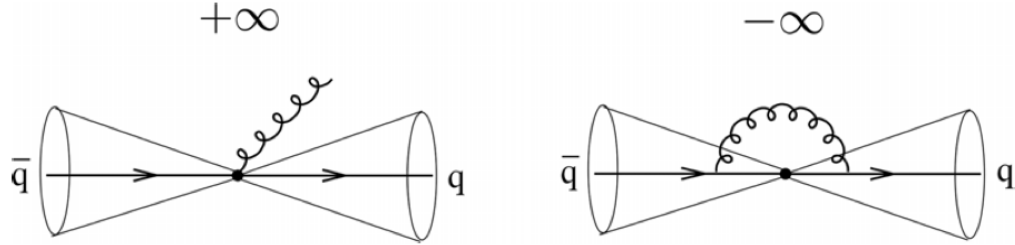


Figure 2.15: Cancellation of singularities in Sfermion Weinberg jets [51]. Singularities arise with opposite signs and cancel.

cancel. This process is shown in Figure 2.15 [51].

This property also ensures jets defined at all levels - detector, hadron and parton level - remain to all intents and purposes the same. Experimentally the calorimetric cells used to define jets at detector level present a huge challenge, as they cannot resolve the energy deposited by a single particle. Instead jets must be defined using transverse energy and pseudorapidity as inputs in place of particle momentum.

## 2.4.1 Jet Algorithms

### Cone Algorithms

There are two main types of jet algorithm. Cone algorithms adopt a ‘top-down’ approach, based on the assumption that branching and hadronisation don’t change the energy flow of an event. The natural approach is to draw cones around energy deposits in the detector and assign particles in this region to be part of that jet. For every cone drawn, the energy deposits or particles within it are removed and this is repeated until everything has been assigned to a jet. In hadron colliders this is done in a 2D plane with axes of pseudorapidity and azimuth, where a particle appears as a dot, when it activates a cluster of calorimeter cells. The result can be plotted as in the lower right-hand panel of Figure 2.16 [54]. This is an event display with a lego plot included, where activated cells are shown along with the transverse energy deposit, which is represented by the height of the yellow towers.

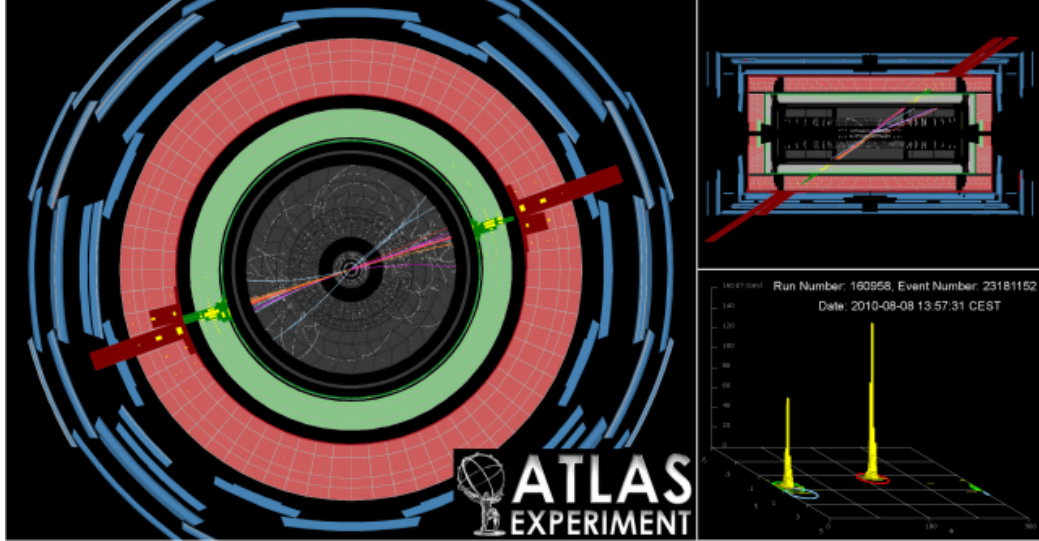


Figure 2.16: A high mass dijet event: two high- $p_T$  jets with invariant mass 2.8 TeV. A track  $p_T$  cut of 2.5 GeV has been applied for the display. On the left is an event reconstruction, the lower right panel shows a jet reconstructed via a cone algorithm.

The difficulty with cone algorithms is ensuring IRC safety. This non-cancellation is illustrated in Figure 2.17 [51]. But the procedure for drawing cones can be refined. Define a stable cone with radius  $R$  and encompassing the set of pseudo-particles  $p_i$ . The jet axis is based on the momenta of the particles inside the cone, with a direction related to for instance the vector sum of the momenta of the jet's constituents. Weighted combinations of rapidity can also be used. Neither collinear splitting nor soft gluon emission can change the momentum of a hard stable cone. Each stable cone can safely be called a jet, which have IRC safe momentum, so the goal of these algorithms is to find all possible hard cones. These types of algorithm are referred to as 'iterative cone' finders, but the procedure described above is not the best example, having a tendency to miss some possible hard cones.

The most successful cone algorithm is called SIScone (where SIS stands for seedless infrared safe). It exploits methods in computational geometry that efficiently move circles around the plane until all stable options have been found. A stable cone is a cone pointing in same direction as the momentum of its contents. This is illustrated along with several other jet algorithms in Figure 2.18 [55].

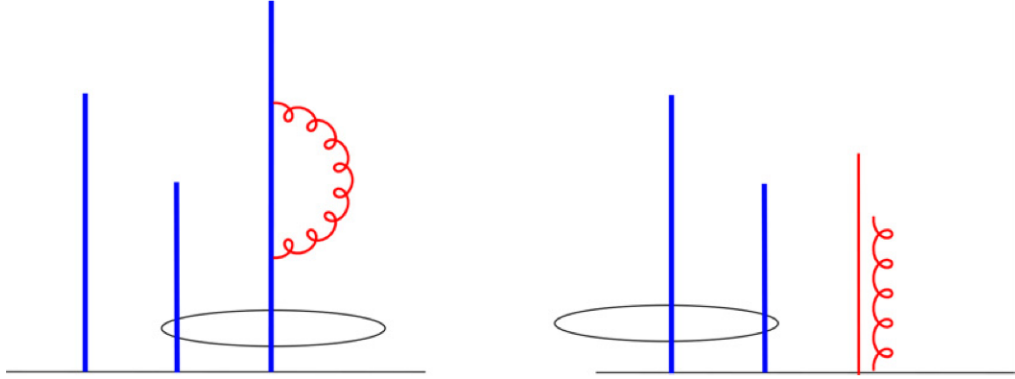


Figure 2.17: Collinear unsafety in algorithms. Partons are represented by lines and their height is proportional to the energy of the parton. With a virtual correction, the parton on the right is more energetic, so this is selected as the initiating parton and grouped with the central particle. With collinear splitting the left-most parton becomes most energetic, with the algorithm selecting this parton and again the central one instead [51].

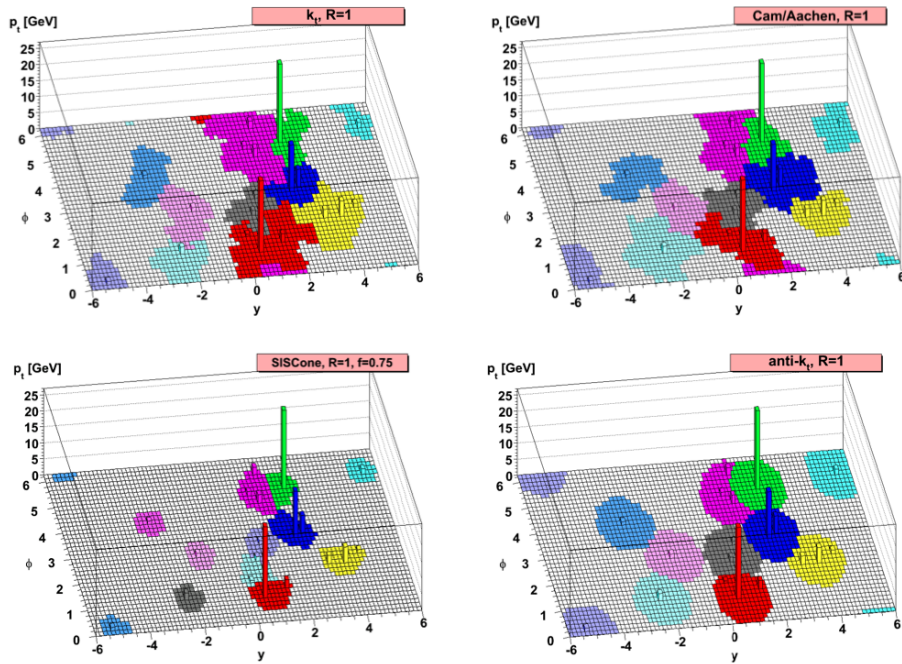


Figure 2.18: An event generated with Herwig and with four different clustering algorithms applied. This figure illustrates how applying different algorithms to the same event leads to different outcomes [55].

When all stable cones have been identified, there is likely to be overlap, and so the final step in the jet definition is defining a procedure for moving from these cones to the list of final jets.

### Sequential Clustering Algorithms

These are generally favoured at ATLAS, and have the advantage of being IRC safe. They work by clustering particles into pairs until none are left. At each step the smallest distance between the pair of particles  $p_i$  and  $p_j$  is called the  $k_t$  distance. The principle remains similar across all variations of this algorithm and begins with the definition of three distances,  $d_{ij}$ ,  $d_{jB}$  and  $d_{iB}$ .

$$d_{ij} = \min(p_{ti}^a, p_{tj}^a) x \frac{R_{ij}^2}{R} \quad (2.20)$$

$$d_{iB} = p_{ti}^a \quad (2.21)$$

$$d_{jB} = p_{tj}^a$$

where the exponent  $a$  corresponds to the specific choice of algorithm and  $R_{ij}^2 = (\eta_i - \eta_j)^2 + (\phi_i - \phi_j)^2$  is the distance between particles in the  $(\eta - \phi)$  space.  $R$  is a radius parameter describing the final size of the jets, which is generally between 0.4 and 0.7 (in this analysis jets with  $R = 0.4$  are used). The parameter  $d_{iB}$  ( $d_{jB}$ ) is the distance from the beam of the particle  $p_i$  ( $p_j$ ). If the minimum of the three  $d$ -parameters is  $d_{iB}$  ( $d_{jB}$ ), the pseudo-particle  $p_i$  ( $p_j$ ) is reassigned from the list of particles to the list of jets. If  $d_{ij}$  is the minimum, the two particles are combined using the summation of four-vectors. This is repeated until one of two conditions is fulfilled. Either all particles must be part of a jet with  $R_{ij} > R$ , which is known as inclusive clustering, or when the desired number of jets has been found, known as exclusive clustering.

In ATLAS, the most common algorithm is the anti- $k_t$  algorithm, which is also the algorithm used for this analysis. The anti- $k_t$  algorithm's popularity can be attributed to its infrared safety, natural clustering order, and robustness - it is widely

implemented in many analysis tools making it easily accessible, and has only one parameter (the distance measure parameter  $R$ ), which makes it relatively easy to use in practice. The choice of  $R$  allows easy adjustments to the size of the resulting jets to suit individual analysis needs. It sets  $a = 2$ , leading to the following:

$$d_{ij} = \min(p_{ti}^2, p_{tj}^2) x \frac{R_{ij}^2}{R} \quad (2.22)$$

$$d_{iB} = p_{ti}^2 \quad (2.23)$$

$$d_{jB} = p_{tj}^2$$

Equation 2.22 leads the algorithm to cluster high- $p_T$  particles preferentially. Essentially it clusters soft particles around hard ones, which remain fixed to a good approximation. The result is that this algorithm is poor for studying the substructure of jets, but is not strongly affected by pileup, so is very good at resolving jets.

Some common issues are encountered regardless of the choice of algorithm. The first is determining the right jet energy scale, in other words assessing the ‘true’ value of a jet’s momentum based on observations from the detector. The second is the effect of recombination, the procedure that determines jet momentum from the momenta of its components. Jet distributions like transverse momentum or invariant mass fall steeply with the increase of these variables, so a migration of events between bins here has a huge effect on their shapes. If a particle causes a peak in the invariant mass of dijet events, mis-measuring momentum could broaden this peak to the point where it is indistinguishable from QCD background.

Jet energy must be determined from calorimetric deposits, the jet energy scale problem. This is done by finding a correction factor to be applied to the observed energy/momentum of a jet, and this corrected value can be used in analyses. This procedure is referred to as ‘calibration’ and is complex, as it must be repeated for every jet algorithm and specific experimental setup. For instance, some of the issues that must be taken into account are the segmentation of calorimeters, available

tracking information (the momentum of charged particles can only be reconstructed in the central region) and noise in the detectors. These and more must be tackled during jet calibration, though some can be addressed offline. Beams of hadrons with known energy could be sent into the detectors and the response studied, though such procedures must also be validated during the experiment.

Recombination also has its impacts, one of which is that it changes the sensitivity of physical observables to the energy–momentum flow inside each jet. If the recombination scheme adds jet three-momenta vectorially, variables like the azimuthal angle between jets are insensitive to QCD radiation inside each jet. This is not the case if it performs a weighted recombinations (see e.g. [56]). Since transverse momentum of a jet depends on the recombination scheme, the jet energy scale calibration has to be repeated for every different approach to recombination that is used.

## 2.4.2 Jet Tagging

Extensions to the Standard Model often include new particles decaying preferentially to gluons or quarks. This gives techniques that may help discriminate between quark- and gluon-initiated jets enormous potential to increase the sensitivity of searches for new physics. Gluons are part of the adjoint representation of  $SU(3)$ , allowing them to carry both color and anti-color charge. Quarks are in the fundamental representation of  $SU(3)$  so they have only a single color charge [57]. The Dokshitzer–Gribov–Lipatov–Altarelli-Parisi (DGLAP) splitting functions [58] contain different factors depending on whether gluon radiation is from a quark ( $C_F$ ) and a gluon ( $C_A$ ). The difference arises from the differing number of color charges each carries. The ratio between these different factors drives the different patterns of radiation and is shown in Equation 2.24:

$$\frac{C_A}{C_F} = \frac{9}{4} \tag{2.24}$$

On average, gluon jets have more constituents than quark jets, and their radiation pattern is broader. Measurements at LEP of the number of constituents of quark and

gluon jets [59] found the following to be true:

$$\frac{\langle N_g \rangle}{\langle N_q \rangle} = \frac{C_A}{C_F} \quad (2.25)$$

$$\frac{\sigma_g^2}{\sigma_q^2} = \frac{C_A}{C_F} \quad (2.26)$$

These are good approximations of the average multiplicity and variance of any type of particle. Using the Sterman-Weinberg definition the angular width of jets is given to leading order by

$$\delta_g = \delta_q \frac{C_F}{C_A} \quad (2.27)$$

This is the mathematical explanation. Intuitively, it is also possible to understand this by considering a quark jet as dominated by the first gluon emission. After that point the showering then follows the same pattern as in a gluon jet. At any given energy gluon jets will contain more particles, and correspondingly fewer hard particles.

Jet flavour is not always a well-defined quantity. In a parton shower, the shower products from hard partons may have significant overlap. Then whether or not the resulting jets merge, or have strange shapes, is dependent on the jet reconstruction algorithm used. The jet properties may also not be distributed in such a way that they correspond to isolated quark or gluon jets. This semi-classical picture differs from the quantum level when NLO quantum effects are considered. At this order there is interference between diagrams with the same final particle momentum and flavor. Figure 2.19 shows collinear gluon emission from quark-initiated jets and the case where gluons come from hard parton splitting. But the dominant contribution to the matrix element calculation is from the parton (quark) shower-like diagram, which has a much larger amplitude than the diagram of hard-gluon-splitting.

NLO effects are reproduced, up to some overall normalisation, by merging the parton shower with corrections to the matrix element. Fully matched samples have a 1:1 association of jets to hard partons of known flavour. With the final distributions

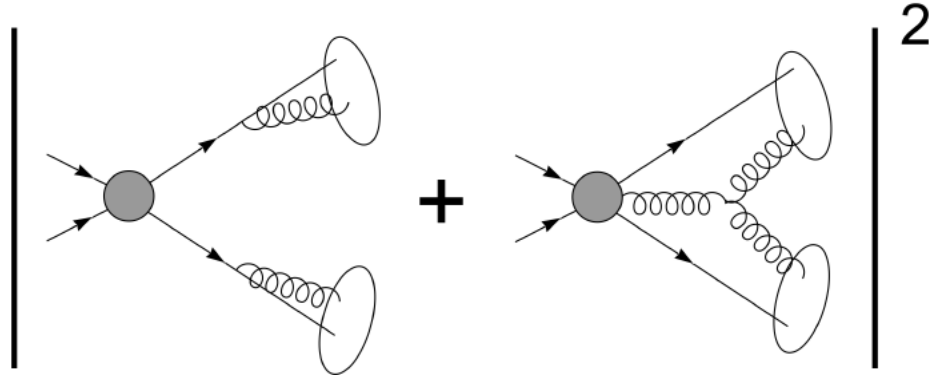


Figure 2.19: In the left diagram, the quark jets have properties largely determined by the emitted gluons. The same configuration can be produced from the right diagram, in which a third hard parton, a gluon, splits into two gluons with momenta comparable to the showered gluons. These two amplitudes interfere, and so it may not make sense to describe the final state configuration as having two quark jets. In this case, the amplitude for the shower diagram on the left is much larger than the hard-gluon-splitting event for the same final state kinematics. As the gluons become more collinear with the quarks, the first amplitude is divergent. From [60].

having only weak dependence on the merging scale, the conclusions that can be drawn regarding quark/gluon discrimination are the same as for kinematic reconstruction - i.e. that the answers are unambiguous when final state jets are clearly separated [60]. Ambiguous final states can be avoided by employing appropriate topological selection criteria.

# Chapter 3

## Data Selection

ATLAS achieved exceptionally high data quality in Run 2, certifying over 95% of recorded data as safe for analysis. Year-on-year improvements are shown in Figure 3.1. The extensive workflow for Data Quality (DQ) assessment is shown in Figure 3.2.

In the q/g tagged dijet search the strategy is derived from the standard procedure for un-tagged dijet searches [63], with identical event selection but additional cuts to obtain enriched samples, which will be described in greater detail in Chapter 4.

### 3.1 Jet Trigger

In this analysis a single jet trigger was used to select events with at least one calorimeter deposit that has transverse energy above a particular threshold. The jet trigger system identifies and saves the most interesting collision events and is composed of a hardware-based Level-1 (L1) trigger and a software-based High-Level Trigger (HLT). Triggers with low  $p_T$  thresholds have prescale factors applied. This means only a random sub-sample of events, which must all pass the selection, are recorded. The rate is  $\frac{1}{p_i}$ , where  $p_i$  is the prescale factor by which sample size is reduced. Favouring the preservation of events for maximum statistics, the dijet tagged analysis uses a non-prescaled trigger with the lowest  $p_T$  threshold. The minimum is set at 420 GeV, as this is the minimum unprescaled dijet trigger which is fully efficient for offline.

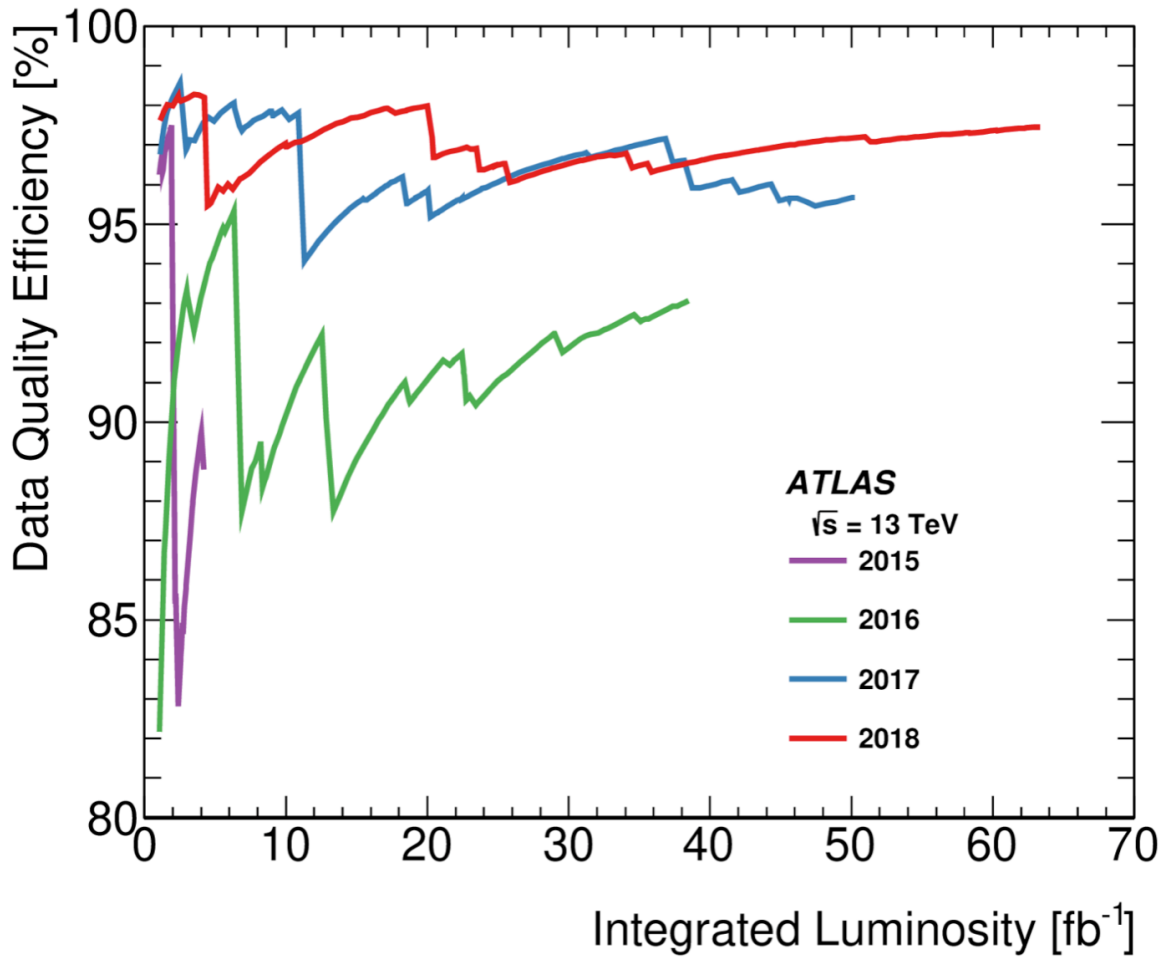


Figure 3.1: Cumulative data quality efficiency vs total integrated luminosity of the ATLAS experiment, 2015-2018. The sharp drops in efficiency are due to single incidents which results in rejection of data on quality grounds. There have been improvements year-on-year during Run 2[61]

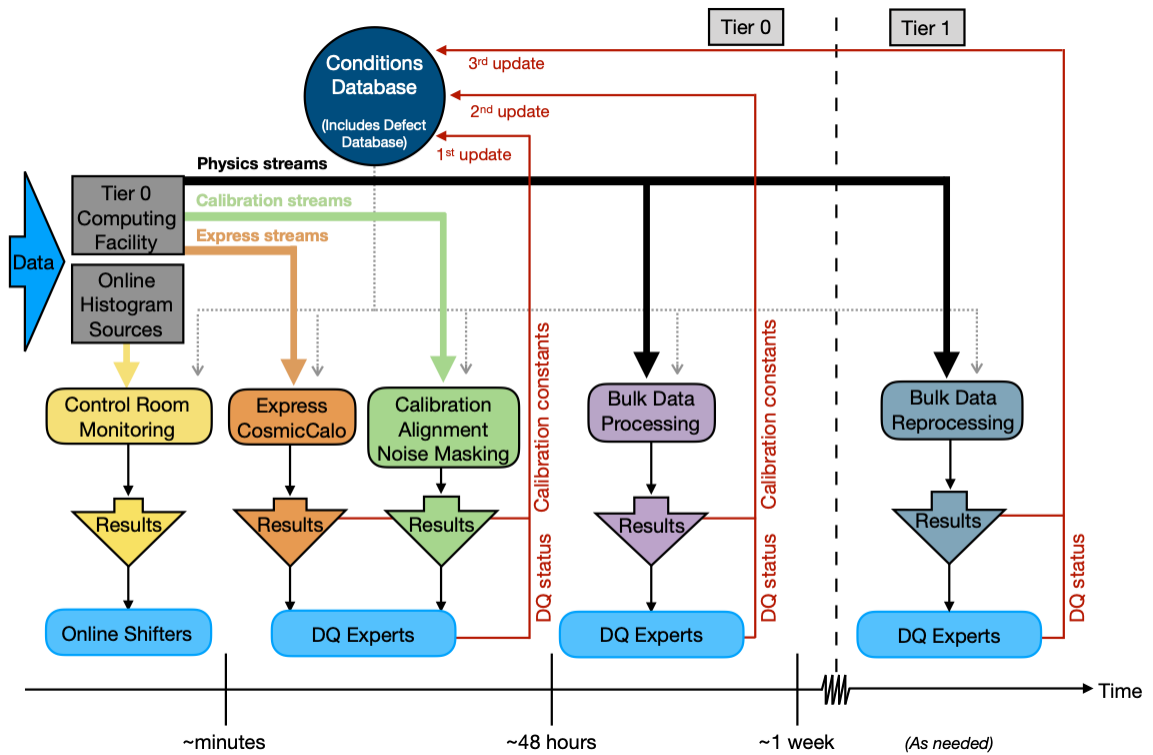


Figure 3.2: Workflow for Data Quality assessment, from [62]. Data is first processed by online shifters (who monitor data in real time and deal with any issues that arise). It is then passed on to Data Quality (DQ) experts, who decide which data is usable for analyses, to continue the process offline.

This also keeps the selection consistent across iterations of this analysis.

Single-jet triggers begin with an uppercase J for L1 triggers and a lower case j for the HLT. Either the uppercase or lowercase j is then followed by the  $p_T$ , e.g. J420. For the L1 triggers the energy scale is the EM scale, where for the HLT triggers, the calibration sequence is almost identical to that applied for offline jets. This brings their scale to the hadronic scale.

Across the complete Run 2 dataset, there are two unrescaled single-jet triggers: HLT\_j420 and HLT\_j225\_gsc420\_boffperf\_split (HLT\_GSC). Both search for jets with a minimum  $p_T$  of 420 GeV, but the HLT\_GSC trigger also applies a global sequential calibration (GSC), normally done offline, to improve the trigger turn-on. The process is described in Section 3.4.2. To measure the trigger’s efficiency in data, a sample was obtained using the HLT\_j360 trigger at  $\sim 420$  GeV.  $5\text{fb}^{-1}$  of high- $\mu$  2018 data were used to measure the trigger turn-ons and  $m_{jj}$ . The efficiencies as a function of jet  $p_T$  are shown in Figure 3.3 [63].

## 3.2 Event Selection

To maximise the chances of signal detection, the dominant QCD background processes must be reduced. This can be achieved with a kinematic cut on the difference in the rapidities of the two leading jets, which selects central jets. For jets with rapidities  $y_1$  and  $y_2$ :

$$y^* = \frac{1}{2}|y_1 - y_2| < 0.6 \tag{3.1}$$

For string resonances a cut of  $|y^*| < 0.8$  is applied instead, based on peaks in signal significance.

The angular distributions of resonant signals, contact interactions and gluon exchange are distinct, with the latter having approximately the same distribution as Rutherford scattering. The first two have  $\cos(\theta)$  angular distributions but gluon ex-

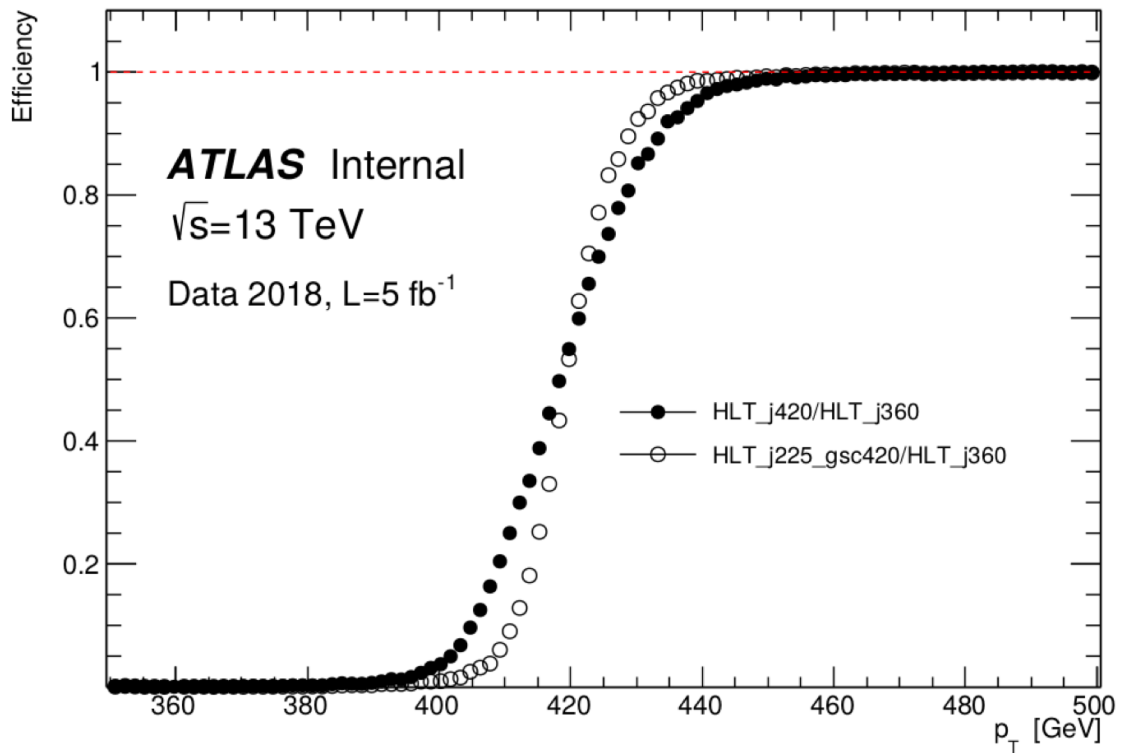


Figure 3.3: Trigger efficiencies and their corresponding fits for HLT\_j420 and HLT\_j225\_gsc420\_boffperf\_split triggers as a function of jet  $p_T$  for 2018 data [63].

change jets can either be distributed isotropically or be some polynomial in  $\cos(\theta)$ . It is on this basis that the requirement for a large polar angle, i.e. central jets, is imposed. Models of new physics generally predict more isotropic angular distributions than would be generated by QCD processes [64].

The lower mass bound of the analysis was set to 1.1 TeV, based on the fact that within the detector acceptance for which the trigger requirement is satisfied, the dijet invariant mass is fully efficient. No upper bound is applied.

### 3.2.1 Good Runs Lists

A GRL is essentially an xml file which specifies sets of luminosity blocks approved for physics analysis use. They depend on the final state analyzed and are different for different physics analyses. There are many reasons data may not be suitable; some examples of these are:

- Too many noisy/damaged cells
- Sub-detectors were off
- Magnets were off or ramping up
- LHC was not in stable-beam mode

The GRLs can be implemented (i.e. selection applied so only good runs are included in data) during ntuple creation or at the ROOT [65] stage. They are compiled by the ATLAS Data Quality (DQ) group and are based on a system of quality flags. There are over 100 flags in total. These have a traffic light hierarchy: red is not usable, yellow denotes flawed data to be used with caution, while green indicates it is cleared for use by analyses. To these are added an additional two layers: Black denotes a sub-detector which was not operational and grey is undefined - status to be decided later, because of short runs or issues with DQ monitoring. Essentially black < grey < red < yellow < green. This system allows different collections to

be assembled very efficiently, with each analysis deciding which subsystems it can tolerate faults within, and which are critical. A good-run list configuration is defined by: a query of detector- and combined-performance DQ flags, a COOL (ATLAS Conditions Database) tag, a set of run numbers, and other criteria, e.g. a certain trigger configuration. An event has passed the GRL when it is within one of the luminosity blocks contained in the list. The overall suitability of a run is determined using the framework described in [33].

The GRLs used for the dijet analysis are selected to ensure all components involved in jet measurements were working, these are:

- 2015(3.2 fb<sup>-1</sup>): data15\_13TeV.periodAllYear\_DetStatus-v89-pro21-02\_Unknown\_-PHYS\_StandardGRL\_All\_Good\_25ns.xml
- 2016(33 fb<sup>-1</sup>): data16\_13TeV.periodAllYear\_DetStatus-v89-pro21-01\_DQDefects-00-02-04\_PHYS\_StandardGRL\_All\_Good\_25ns.xml
- 2017(44 fb<sup>-1</sup>): data17\_13TeV.periodAllYear\_DetStatus-v99-pro22-01\_Unknown\_-PHYS\_StandardGRL\_All\_Good\_25ns\_JetHLT\_Normal2017.xml
- 2018(58.5 fb<sup>-1</sup>): data18\_13TeV.periodAllYear\_DetStatus-v102-pro22-04\_Unknown\_-PHYS\_StandardGRL\_All\_Good\_25ns\_TriggerNo17e33prim.xml

### 3.3 Jet Reconstruction and Calibration

A variety of objects can be used to define a jet in ATLAS. Either tracking information or information gathered at calorimeter level can be employed, with the suitability of each determined by the application. Calibration studies generally make use of track jets, which are assembled with tracks and momenta from the inner detector. Jets simulated in Monte Carlo have known particle constituents, i.e. truth information, which can be given as input four-vectors to the jet reconstruction algorithms used

by analyses. The outputs are called ‘truth jets’, and are useful for calibrating jet reconstruction performance and its variations.

However in this analysis a higher-level input than calorimeter level is used. These objects are called topoclusters, and they consist of bunches of topologically connected calorimeter cells. The exceptional resolution of the ATLAS calorimeter makes it a popular choice for this purpose [66]. A topological clustering algorithm is used, described in [66] and [67]. The algorithm used reconstructs particle showers using the lateral and longitudinal segmentation of the calorimeters - i.e. building 3D showers using 3D energy deposits in the calorimeter. Along with reconstructing the energy, it aims to give information on the directions of the incoming particles. The seeds for topoclusters are calorimeter cells with absolute energy measurements  $|E| > t_{\text{seed}}\sigma_{\text{noise}}$ , where  $t_{\text{seed}}$  is the chosen seed threshold and  $\sigma_{\text{noise}}$  is the deviation of the expected noise, which includes electronic noise as well as the expected contribution from pile-up. This renders it dependent on run conditions. This first step is followed by the iterative addition of all adjacent cells with  $|E| > t_{\text{adjacent}}\sigma_{\text{noise}}$ , repeated again for this latest set with  $|E| > t_{\text{cell}}\sigma_{\text{noise}}$ . If we wish all neighbouring cells to be included, this can be achieved with  $t_{\text{cell}} = 0$ . But the set of adjacent cells is not limited to the eight surrounding cells - overlaps in  $\eta$  and  $\phi$  from either adjacent layers or adjacent calorimeter systems can also result in a cell forming part of the set. In practice this often leads to the number of neighbouring cells being  $> 10$ , with variations being due to changes in granularity between layers and detector regions. There are two types of cluster available in the standard ATLAS reconstruction, the electromagnetic EM 633 and Had 420 clusters, with their parameters shown in Table 3.1 [67].

The parameters in the Had420 algorithm described in Table 3.1 are optimized for the efficient identification of low energy clusters without being overly affected by noise. To achieve a symmetric contribution from noise, a cut is applied on absolute energy requiring the seed cells to have  $|E| > 0$ . While the granularity and noise thresholds vary across the ATLAS calorimeters, they are all initially calibrated to

Parameter	EM 633	Had420
Calorimeters	EM only	All
Seed signal definition	E	$ E $
Cluster cut before splitting	$E_T > 5 \text{ GeV}$	$ E_T  > 0 \text{ GeV}$
$t_{\text{seed}}$	6	4
$t_{\text{adjacent}}$	3	2
$t_{\text{cell}}$	3	0

Table 3.1: Parameters used to build the two types of topological cluster available in the standard ATLAS reconstruction. From [67].

the EM scale. This correctly measures the energy deposited by particles from EM showers, while hadronic interactions produce responses lower than this scale, with the precise amount depending on where the showers develop. The analysis uses an EM scale calibration with the parameters of the Had420 topological clustering algorithm.

If sufficient energy is deposited between incident particles, clusters can grow to cover large areas of the detector. Splitting two local energy maxima into separate topoclusters becomes important so that even in the case of overlapping showers, individual particles can be separated. The final cluster is then subject to the energy cut. Removing cells with insignificant signals which are not close to cells with significant signal suppresses noise and the impact of pileup, but does include soft radiation at the perimeter of a cluster. The resulting clusters are called EMTopo clusters, and they are given as inputs to the anti- $k_t$  jet reconstruction algorithm, with the distance parameter  $R$  set to 0.4.

### 3.4 Jet Calibration

One of the issues associated with jets reconstructed from calorimeter topoclusters is that their energy can differ from the true energy of the original parton. The topoclusters associated with calorimeter cells might be accurate in their measurement

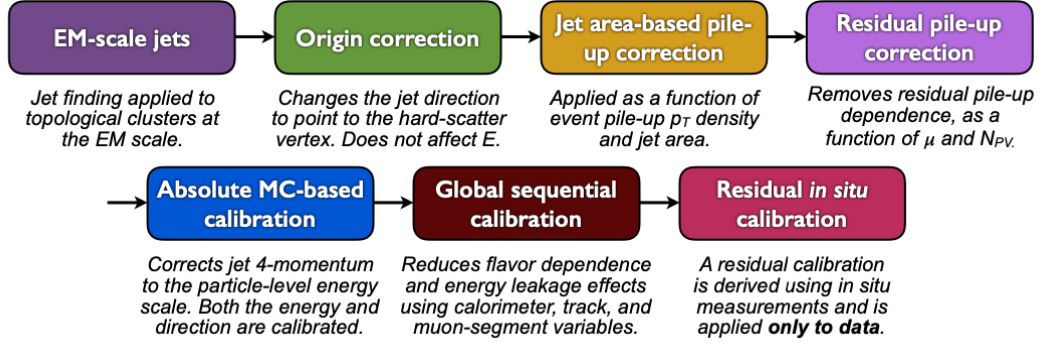


Figure 3.4: Calibration stages for EM-scale jets, from [66].

of energy deposits from EM showers, but they are poor at measuring those from hadronic showers. There are other problems that can contribute to difficulty making an accurate jet energy measurement, including:

- Reconstruction efficiency: Low energy deposits are excluded because of noise threshold requirements, but this can also lead to exclusion of genuine energy deposits and therefore energy losses.
- Leakage: Punch-through, when showers enter the muon system, allows energy to escape measurement by the calorimeters
- Dead material: Unresponsive detector areas can underestimate the energy deposited in them
- Out of jet cone: An issue originating right back at the MC stage, particles in the truth jet can incorrectly end up outside the reconstructed calorimeter jet and therefore excluded from energy measurements.

To combat these problems and restore the jet energy scale (JES) to that of the reconstructed truth jets, the ATLAS calibration scheme was developed. It corrects the full four-momentum of the jet at every stage, i.e. it scales jet  $p_T$ , energy and mass. The full procedure is summarised in Figure 3.4 [66].

The origin correction is the only stage that does not affect the full four-momentum as it recalculates four-momentum to point to the hard-scatter vertex but keeps the energy constant. Origin corrections improve the  $\eta$  resolution of jets. At a jet  $p_T$  of about 20 GeV, a typical improvement would be from 0.06 to 0.045. Pile-up corrections remove excess energy from overlapping collisions. The JES calibration changes the four-momentum to the particle-level energy scale derived from MC truth jets. Global sequential calibration employs the calorimeter, MS and track variables to further improve uncertainties and track-based variables. The final in-situ calibration corrects jets using well-understood reference objects. These steps are described in greater detail below.

### 3.4.1 Pile-up Corrections

Both in-time and out-of-time pileup contributions can be removed in this step. For Run 2 the applied techniques were developed in 2021, with techniques from Run 1 no longer applicable because of new developments in the data-taking environment. There are two components to the Run 2 procedure. The first is applied at a per-event level and consists of an area-based momentum density subtraction [55]. The pile-up contribution to each individual event is subtracted based on its area, with the area calculated using the median  $p_T$  density  $\rho$  of the jets in the  $\eta - \phi$  plane. Only positive energy topoclusters that meet the requirement for  $|\eta| < 2$  are used, clustered with the anti- $k_T$  algorithm. The central  $|\eta|$  cut excludes the forward calorimeter regions, which have higher occupancy, and the anti- $k_T$  algorithm is used for its high sensitivity to soft radiation.

### 3.4.2 Jet Energy Scale and $\eta$ Calibration

The differences in calorimeter technologies and granularities can lead to biases arising in jet  $\eta$  reconstruction. For the Jet Energy Scale (JES), the calibration is derived from correcting reconstructed jet energy to truth jet energy from a Pythia MC sam-

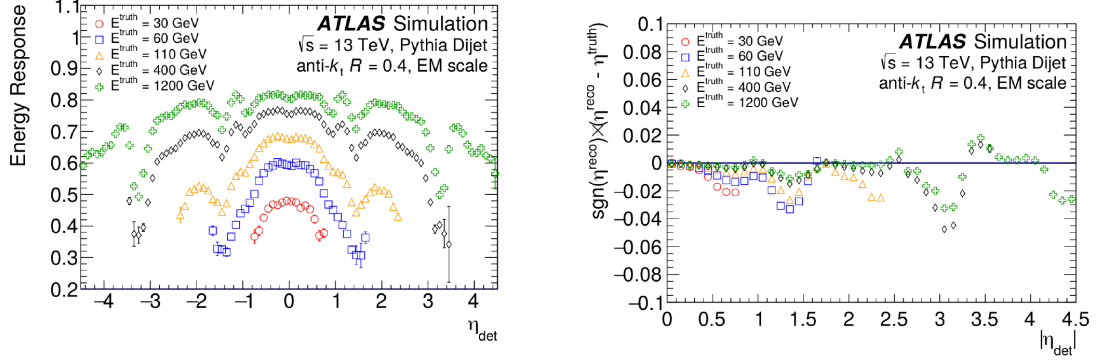


Figure 3.5: Average energy response (a) and  $\eta$  difference (b) between truth and reco jets for truth energies of 30, 60, 110, 400 and 1200 GeV [68].

ple, specifically after both origin and pileup corrections have already been applied [68]. Then the average energy response is taken to be the mean of a Gaussian fit to the  $E^{\text{reco}}/E^{\text{truth}}$  distribution of the jets, which are binned in  $E^{\text{truth}}$  and  $\eta_{\text{det}}$ , a vector of the jet  $\eta$  which points to the geometric centre of the detector. The result therefore corresponds directly to the geometry of the calorimeter and is experiment-specific. If a lower energy response is observed, this may indicate either absorbed or undetected particles caused by gaps or transitions between the different elements in the calorimeter. The result of applying the full ATLAS detector response simulation is shown in Figure 3.5 [68].

The fitting function for the calibration is defined in [69] as:

$$\mathcal{F}_{\text{calib},k}(E^{\text{jet}_{\text{EM}}}) = \sum_{i=0}^{N_{\text{max}}} a_i, k(\ln E^{\text{jet}_{\text{EM}}})^i_k \quad (3.2)$$

where  $a_i$  are the free fit parameters,  $N_{\text{max}}$  is between 1 and 6 and depends on the goodness of fit and  $k$  is the specific  $\eta_{\text{det}}$ . Scaling the measured jet energy by the value of  $\mathcal{F}_{\text{calib},k}(E^{\text{jet}_{\text{EM}}})$  gives the corrected jet energy in the relevant bin  $k$ :

$$E^{\text{jet}_{\text{EM}}+JES} = \frac{E^{\text{jet}_{\text{EM}}}}{\mathcal{F}_{\text{calib},\eta_{\text{det}}} E^{\text{jet}_{\text{EM}}}} \quad (3.3)$$

The differences between the calculated pseudorapidity of the reconstructed jet  $\eta^{\text{reco}}$  and  $\eta^{\text{truth}}$  are also shown in Figure 3.5. The difference is most noticeable in jets that

encompass different regions of the calorimeter or to changes in geometry or technology. This is because when such changes occur, it alters the energy response of one part of the jet compared with another, which is carried forward into the reconstructed four-momentum. The impact is clearly visible in Figure 3.5b at for example the transition from the barrel-endcap region ( $|\eta_{\text{det}}| \sim 1.4$ ) and the endcap-forward region at  $|\eta_{\text{det}}| \sim 3.1$ . To compensate for these effects, a second correction is necessary in addition to that applied to the jet energy, this time applied to the jet pseudorapidity. It is derived from the difference between  $\eta^{\text{reco}}$  and  $\eta^{\text{truth}}$  and parameterised as a function of  $\eta_{\text{det}}$  and  $E^{\text{truth}}$ . However this does not apply to the full four-momentum and instead corrects only  $p_T$  and  $\eta$ .

### Global Sequential Calibration

The response of the calorimeter and the jet reconstruction are affected by fluctuations in the particle composition of jets and on their energy distribution. The former depends on the initiating particle, as does shower shape, with particularly marked differences between quark- and gluon-initiated jets. Quark jets typically include hadrons that penetrate further into the calorimeter, as they have a higher fraction of the jet  $p_T$ . Gluon jets will have softer particles that have a lower calorimeter response and a wider transverse profile. Five observables that improve JES resolution have been identified by the Global Sequential Calibration (GSC) [70].

The GSC extends the calibration of EM+JES with a multivariate technique. In practice any variable that correlates with the detector response to a jet can be used. The correction is found by inverting the calibrated jet response  $\mathcal{R}$  as a function of the chosen variable  $x$ :

$$C(x) = \frac{\mathcal{R}^{-1}(x)}{\langle \mathcal{R}^{-1}(x) \rangle} \quad (3.4)$$

After this process is completed, the numerical inversion is multiplied by a constant. This removes any remaining dependence of the response on the particular variable  $x$ .

Parameter	Definition	$ \eta_{\text{det}} $
$f_{\text{LAr3}}$	Fraction of jet energy measured in the 3rd layer of the EM LAr calorimeter	$< 3.5$
$n_{\text{track}}$	The number of tracks with $p_T > 1$ GeV ghost-associated with the jet	$< 2.5$
$\mathcal{W}_{\text{track}}$	The average of $p_T$ weighted transverse distances in the $\eta - \phi$ plane, between the jet axis and all $n_{\text{track}}$	$< 2.5$
$f_{\text{Tile0}}$	The measured fraction of jet energy deposited in the first layer of the TileCal	$< 1.7$
$n_{\text{segments}}$	Muon track segments ghost-associated with the jet	$< 2.7$

Table 3.2: The five observables used to derive a calibration to improve JES resolution.

The sequential application of these corrections for several observables results in the optimum resolution. All that is required is for the correction associated with variable  $x_i(C^i)$  to be applied to already corrected jets, with a correction deriving from the variable  $x_{i-1}(C^{i-1})$ . The full corrected jet transverse momentum is then:

$$p_T^i = C^i(x_i) \times p_T^{i-1} = C^i(x_i) \times C^{i-1}(x_{i-1}) \times p_T^{i-2} \dots \quad (3.5)$$

The five observables shown to improve the JES resolution are listed in Table 3.2.

Altering the order in which these calibration factors are applied has no effect, nor does applying additional calibrations based on variables with which the base five correlate. The first four parameters are functions of  $p_T$ , while the  $n_{\text{segments}}$  variable accounts for high- $p_T$  jets not being fully contained within the calorimeter. Punch-through jets increase the tails of the response distribution as they affect the  $p_T$ -weighted track width. It is strongly correlated with the energy escaping the calorimeters and should therefore be derived as a function of energy.

Slight differences (small compared to the corrections) between data and the modelling of the five key variables in MC have a negligible impact on the GSC [68], provided the dependence of the average jet response on the observables is well mod-

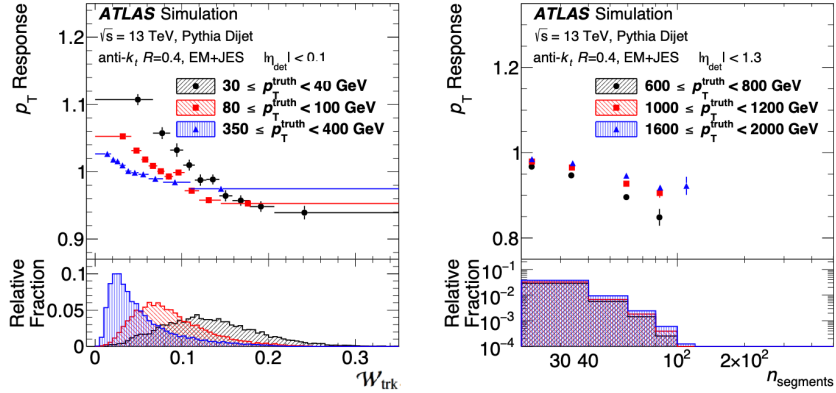


Figure 3.6: The average jet response in MC simulation as a function of the GSC variables for three ranges of truth jet  $p_T$ . Jets are constrained to  $|\eta| < 0.1$  for the distributions of calorimeter and track-based observables and  $|\eta| < 1.3$  for the muon nsegments distribution. The distributions of the underlying observables in MC simulation are shown in the lower panels for each truth jet  $p_T$  region, normalized to unity.

elled. The jet response in MC is shown as a function of each observable in Figures 3.6 and 3.7.

The dependence of the jet response on each observable is less than 2% after the GSC is fully applied. The small remaining deviations from unity are the result of correlations between observables that have not been accounted for but are negligible in total. These dependences were tested using the dijet tag-and-probe method described in Ref. [71], Section 12.1. The average momentum asymmetry between back-to-back jets was measured in 2015 as a function of each of the five observables, and data was found to be compatible with MC simulation.

### In situ Calibration

The final calibration aims to account for differences between data and MC using a well-understood and well-measured set of reference objects. This difference is quantified by the ratio of the  $p_T$  balance between jets and a reference object. The balance is given by Equation 3.6.

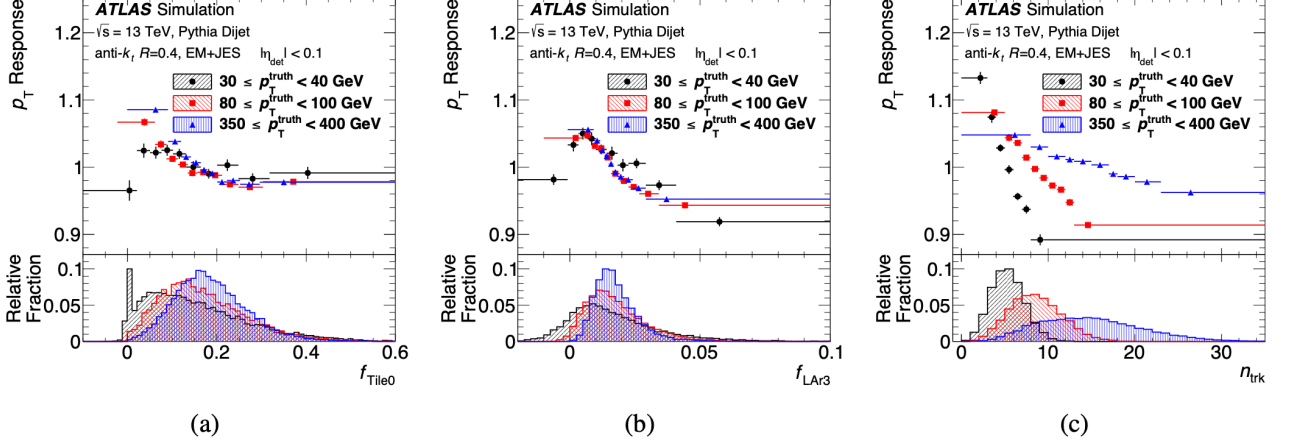


Figure 3.7: The average jet response in MC simulation as a function of the GSC variables for three ranges of  $p_T^{\text{truth}}$ . a) is the number of muon track segments ghost-associated with the jet. b) is shown with both preceding calorimeter corrections applied, and the punch-through distribution c) is shown with the four calorimeter and track-based corrections applied [66]. The distributions of the underlying observables in MC simulation are shown in the lower panels for each truth jet  $p_T$  region, normalized to unity.

$$\mathcal{A} = \frac{p_T^{\text{probe}} - p_T^{\text{ref}}}{p_T^{\text{avg}}} \quad (3.6)$$

This asymmetry uses  $p_T^{\text{probe}}$ , the transverse momentum of the forward jet,  $p_T^{\text{ref}}$ , the transverse momentum of the jet in a well-calibrated reference region and the average  $p_T$  of both jets,  $p_T^{\text{avg}}$ .

The complete in-situ calibration consists of an  $\eta$ -intercalibration, a  $Z/\gamma$ +jet and multijet calibration, applied sequentially. These processes are described in greater detail below. The  $\eta$ -intercalibration takes well-measured dijets in the central region ( $|\eta| < 0.8$ ) and uses them to derive a residual calibration for jets in the forward region ( $0.8 < |\eta| < 4.5$ ). While the central and forward jets should be balanced in  $p_T$ , up to leading order in QCD, imbalances are often observed that are attributable to differing responses in different calorimeter regions. The responses are generally less well understood in the forward region and so can be corrected based on central jets. Dijet topologies in which the two leading jets are back-to-back in  $\phi$  are selected and

there should be no substantial contamination from a third jet.

Deviations arise from imperfect understanding of the detector material and its response carried over into MC, as well as imperfections in the simulation of hard scatter, hadronisation, pileup and EM/hadronic interactions in the detector. Conservation of momentum allows the correct jet energy to be derived. Three distinct in-situ calibrations correct differences in the response of central jets ( $|\eta| < 1.2$ ) across different  $p_T$  regimes, each employing a different reference object, the  $Z$  boson, photon and multijet systems respectively. For each in-situ calibration the response  $\mathcal{R}_{\text{insitu}}$  has the same definition in both data and MC and is the average ratio of jet  $p_T$  to the  $p_T$  reference object (which depends on the momentum range, discussed below). The direct  $p_T$  balance between a jet and the decay products of a  $Z$  boson, through the decay channels of  $Z \rightarrow e^+e^-$  and  $Z \rightarrow \mu^+\mu^-$ , is used at transverse momenta in the range  $20 < p_T < 500$  GeV. This is the range where production of  $Z$  bosons is statistically significant, and it relies on independent measurement and calibration of the lepton decay products of the  $Z$ . The  $\gamma$ +jet calibration is limited to between 36 and 950 GeV because of the small number of events at high  $p_T$ , contamination by dijet events and prescaled triggers that artificially reduce the number of events at low  $p_T$ , and relies on measurement and calibration of photon energy. Up to 2 TeV, the multijet balance is used, where events with three or more lower  $p_T$  jets are selected which balance a single high- $p_T$  jet. In this selection the three recoil jets have  $p_T$  low enough for the  $Z$  and  $\gamma$ +jet calibration to be valid.

At each step of the in-situ calibration the calorimeter response to EM+JES jets, gluon radiation and energy losses outside the jet cone will affect  $\mathcal{R}_{\text{insitu}}$ , but these can all be mitigated with event selection. Assuming all these factors are well modelled by MC, the following ratio is a useful estimate of the ratio of the JES in data and MC:

$$c = \frac{\mathcal{R}_{\text{insitu}}^{\text{data}}}{\mathcal{R}_{\text{insitu}}^{\text{MC}}} \quad (3.7)$$

Then a combination of the calibration constants derived from each of the ratios de-

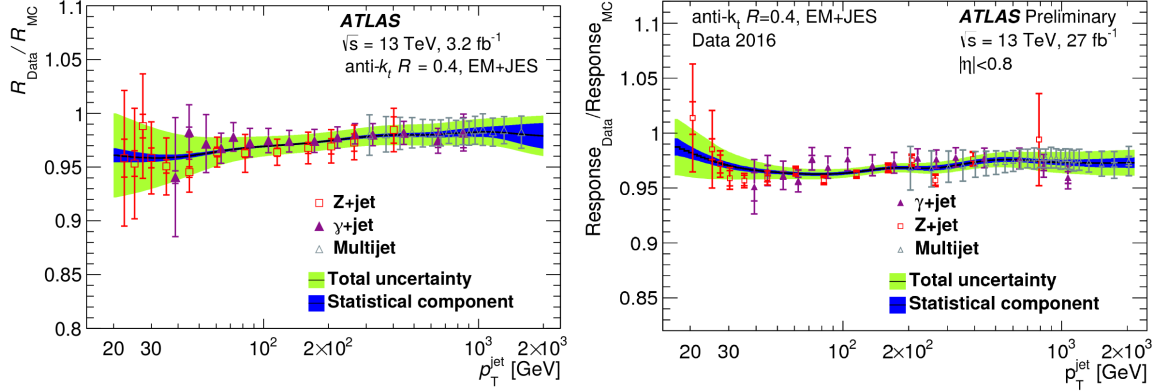


Figure 3.8: Data/MC EM+JES jet response ratio for the  $Z$ +jet,  $\gamma$ +jet and multijet channels used for in-situ calibrations. The black line indicates the final correction. The uncertainties are shown in dark blue (statistical) and light green (total). Finally the original ratios are shown. From [73], [72].

scribed above ( $Z$ +jet,  $\gamma$ +jet and multijet) and the  $\eta$ -intercalibration are combined to produced the final correction, which is the numerical inversion as a function of jet  $p_T$  and jet  $\eta$ .

The data/MC ratio and their corresponding systematic uncertainties from the balances are combined in overlapping  $p_T$  regions. The uncertainties are due to:

- Potential mis-modeling of underlying physics
- Measurement of the reference object kinematics
- The effects of selected event topology on modeling of the  $p_T$  balance

The result of this combination is a common data/MC ratio, through interpolation with second-order polynomial splines, in very fine  $p_T$  bins. It is pictured in Figure 3.8. The combined correction is the inverse of the combined data-to-MC correction and is 4% at low  $p_T$ , which goes down to 2% at 2 TeV. The individual corrections show good agreement with each other and  $\sqrt{\chi^2/N_{\text{dof}}}$  is generally below 1 [72].

So for each in-situ method, there is a  $p_T$ -dependent weight, according to a  $\chi^2$  minimisation with inputs of the response ratios and uncertainties in every  $p_T$  bin. These weights are higher in  $p_T$  regions with smaller bin sizes and smaller relative

uncertainties, with statistical fluctuations minimised by smoothing with a sliding Gaussian kernel.

## JES Uncertainties

The JES is the largest individual uncertainty for the majority of jet searches. Eighty JES systematic uncertainties are included in the final calibration, propagated sequentially through each individual calibration and study. This is unwieldy and would hamper a number of physics analyses in their progress, while often not providing any discernible benefit, and in these cases a reduced set of nuisance parameters is made available. The majority of the systematics come from the three corrections described in the previous section, the  $Z$ +jet,  $\gamma$ +jet and multijet in-situ calibration constants. They account for assumptions in event topology, MC simulation and sample statistics, along with the energy scales of electrons, muons and photons [72], [74], [75].

The systematics in these calibrations are averaged and smoothed in the combination step, which is achieved through an interpolation [68] [71]. As the variations between results of the in-situ methods are smooth, it is sufficient to employ a linear interpolation. Every source of uncertainty is shifted by  $1\sigma$ , with the method's original binning. The binning interpolation and combination are then repeated with nominal weighting. The systematics are treated independently which allows for alternative correlation assumptions at later stages: the difference between treating correlations before and after the combination are found to be negligible. However the starting point is an assumption that they are fully correlated in  $p_T$ . As for the weights, each component of the systematic uncertainties is smoothed with a sliding Gaussian kernel.

On occasion there are disagreements in the different nominal corrections within a  $p_T$  bin. Disagreement is defined as a bin which has a tension factor of  $\sqrt{\chi^2/N_{\text{dof}}} > 1$ . When this is the case, the uncertainty is scaled by the tension factor in that bin. In 2015 this was only found to be necessary in the very narrow  $p_T$  region of  $45 < p_T < 50$  GeV[76].

The uncertainties from the in-situ calibrations are summarised in Table 3.3. The  $\eta$ -intercalibration stage introduces the three uncertainties in the last three rows of the table, to cover mis-modeling of the underlying physics of the event, non-closure between  $2.0 < |\eta_{det}| < 2.6$  and a component to account for statistical fluctuations.

<b>Systematic Name</b>	<b>Description</b>
<b><math>Z + \text{jet}</math></b>	Systematic Description
Electron Scale	Uncertainty in electron energy scale
Electron Resolution	Uncertainty in the electron energy resolution
Muon Scale	Uncertainty in the muon momentum scale
Muon resolution (ID)	Uncertainty in muon momentum resolution in the ID
Muon resolution (MS)	Uncertainty in muon momentum resolution in the MS
MC generator	Difference between MC event generators
JVT	Jet vertex tagger uncertainty
$\Delta\phi$	Variation of $\Delta\phi$ between the jet and the Z boson
2nd jet veto	Radiation suppression through second-jet veto
Out-of-cone	Contribution of particles outside the jet cone
Statistical	Statistical uncertainty over 13 regions of jet $p_T$
<b><math>\gamma + \text{jet}</math></b>	
Photon Scale	Uncertainty in the photon energy scale
Photon resolution	Uncertainty in the photon energy resolution
MC generator	Difference between MC event generators
JVT	Jet vertex tagger uncertainty

Table 3.3 – continued from previous page

Systematic Name	Description
$\Delta\phi$	Variation of $\Delta\phi$ between the jet and the Z boson
2nd jet veto	Radiation suppression through second-jet veto
Out-of-cone	Contribution of particles outside the jet cone
Photon Purity	Purity of sample in $\gamma$ +jet balance
Statistical	Statistical uncertainty over 15 regions of jet $p_T$
<b>Multijet-balance</b>	
$\alpha^{MJB}$ Selection	Angle between leading jet and recoil system
$\beta^{MJB}$ selection	Angle between leading jet and closest subleading jet
MC Generator	Difference between MC event generators
$p_T^{\text{asymmetry}}$ selection	Second jet's $p_T$ contribution to the recoil system
Jet $p_T$ Threshold	Jet $p_T$ Threshold
Statistical	Statistical uncertainty over 16 regions of jet $p_T^{\text{leading}}$
<b><math>\eta</math> – intercalibration</b>	Systematic Description
Physics mismodelling	Envelope of the MC, pile-up, and event topology variations
Non-closure	Non-closure of the method in the $2.0 <  \eta_{det}  < 2.6$ region
Statistical	Statistical uncertainty

Table 3.3: Summary of the uncertainties from the in-situ calibrations.

The remaining uncertainties are summarised in Table 3.4 and described in greater detail here. Four come from correcting for pile-up. Three arise from variations in the jet response and the simulated particle composition of light-quark,  $b$ - and gluon jets. This flavour response uncertainty is derived from comparing the average jet response for each flavour across two different MC generators, Pythia and Herwig++. The uncertainty in flavour composition is specific to each analysis. There is also a punch-through correction uncertainty from the GSC, which is the maximum difference in data/MC as a function of muon segments. Fast-simulation jets, produced with FastCaloSim [77], also contribute to the uncertainty. FastCaloSim was developed to provide a balance between accuracy and fast simulation of the ATLAS calorimeter system. Parameterizations of electromagnetic and hadronic calorimeter showers are used to deposit particle energies in the calorimeter structure. The uncertainty is associated with non-closure in their absolute JES calibration. The dijet analysis only uses these for signal samples, with background produced using the full GEANT4 ATLAS detector simulation [78]. Finally, and of greatest relevance to the dijet analysis, is the systematic for calibrating calorimeter response to jets in the very high- $p_T$  regime. Recall that all in-situ calibrations are limited to  $p_T < 2$  TeV, as beyond this region there are too few jets in the data for these techniques to be effective. In its place a single hadron response calibration is used. Minimum bias data samples provide examples of the JES per isolated single hadron. The particle type corresponding to every calorimeter energy deposit in a jet is then identified and the energy calibration is performed based on these single particle responses. For jet transverse momenta above 2 TeV, this uncertainty is found to be between 2% and 5% [13]. The final combined uncertainty in the JES is shown in Figure 3.9.

The uncertainty is highest at low- $p_T$  but decreases to a minimum of  $\sim 1\%$  at 200 GeV. It then rises again at high  $p_T$  as the multijet balance calibration is no longer valid and the switch to single particle response calibrations occurs, with higher associated uncertainties.

Name	Systematic Description
<b>Pile-up</b>	
$\mu$ offset	Uncertainty of the $\mu$ modelling in MC simulation
$N_{PV}$ offset	Uncertainty of the $N_{PV}$ modelling in MC simulation
$\rho$ topology	Uncertainty of the per-event $p_T$ density modelling in the MC simulation
$p_T$ dependence	Uncertainty in the residual $p_T$ dependence
<b>Jet flavor</b>	
Flavor composition	Uncertainty in the jet composition between quarks and gluons
Flavor response	Uncertainty in the jet response of light quark and gluon-initiated jets
$b$ -jet	Uncertainty in the jet response of $b$ -quark-initiated jets
Punch-through	Uncertainty in GSC punch-through correction
AFII non-closure	Difference in the absolute JES calibration using AFII
Single-particle response	High- $p_T$ jet uncertainty from single-particle and test-beam measurements

Table 3.4: Additional systematic uncertainties in the JES. Uncertainties from electron, photon and muon energy scales [75].

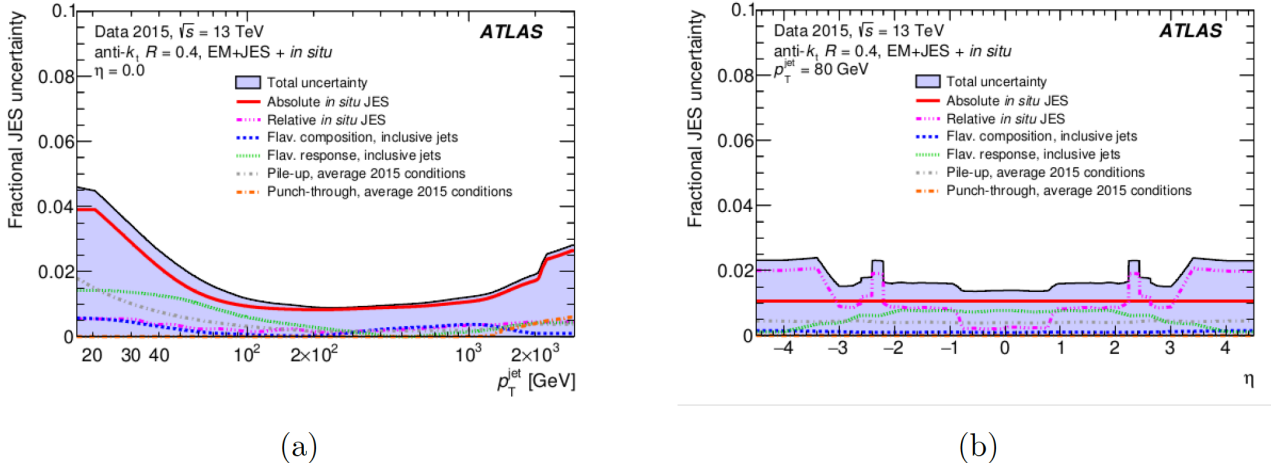


Figure 3.9: Final total uncertainty of jets in the JES as a function of (a) jet  $p_T$  at  $\eta = 0$  and (b)  $\eta$  at  $p_T = 80$  GeV. Systematic uncertainty components include pile-up, punch-through, and uncertainties propagated from the  $Z/\gamma$ +jet and multi-jet balance (absolute in situ JES) and  $\eta$ -intercalibration (relative in situ JES). The flavor composition and response uncertainties assume a quark and gluon composition taken from Pythia dijet MC simulation (inclusive jets) [75].

### 3.5 Jet Energy Resolution

The jet energy resolution quantifies the detector’s ability to resolve the difference in energy between two jets of similar total energy. Uncertainties in this resolution,  $\sigma(E)/E$ , can arise from inaccuracies in the simulation of the detector resolution. Precise knowledge of the jet energy resolution (JER) is important for searches for physics beyond the SM involving jets [79], and affects the measurement of missing transverse momentum. The JER is measured in situ with two techniques, the bisector method and the dijet balance method [80]. They exploit the fact that at fixed rapidities the fraction JER is the same as the fractional jet  $p_T$  resolution,  $\sigma(p_T)/p_T$ .

The bisector method projects the vector sum of leading jet transverse momenta onto the coordinate system bisector of the azimuthal angle between their individual transverse momentum vectors, a process illustrated in Figure 3.10 [81].

In a perfectly balanced dijet event the vector sum of  $p_T = 0$ . There are a number of effects that can disrupt this value, notably among them initial state radiation causing

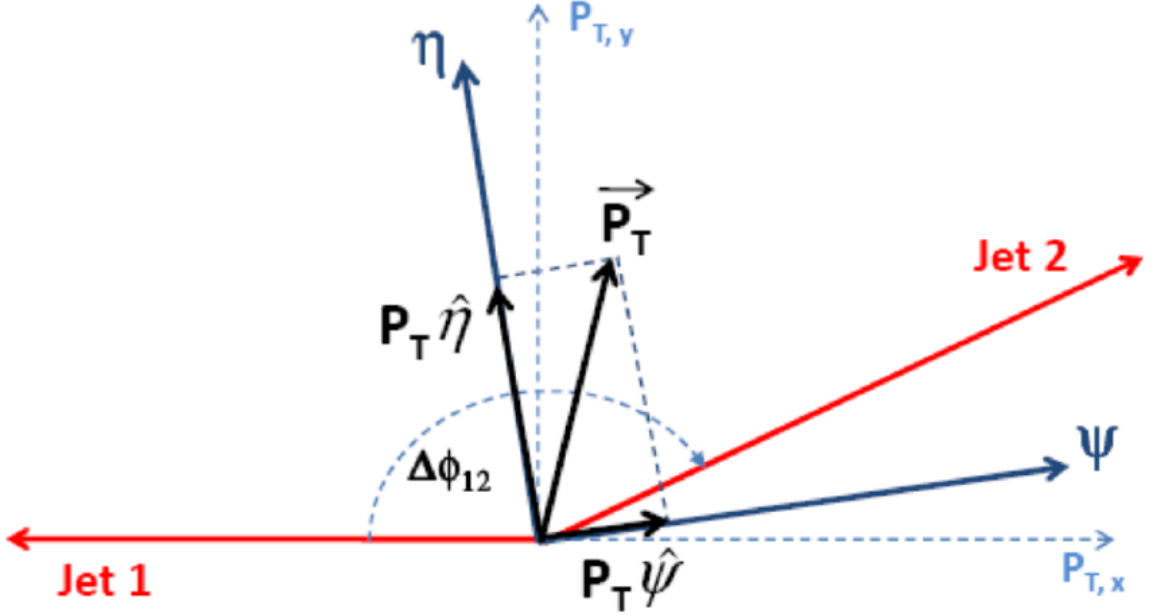


Figure 3.10: An illustration of the variables used in the bisector method for JER uncertainties. The  $\eta$ -axis corresponds to the azimuthal angular bisector of the dijets, and the  $\Psi$ -axis is orthogonal to the  $\eta$ -axis. Both are transverse to the beam which goes into the page [81].

isotropic fluctuations in the  $\eta - \phi$  plane.

The dijet balance method uses the conservation of momentum in the transverse plane and defines an asymmetry  $A$  between the momenta of the two leading jets as

$$A(p_{T,1}, p_{T,2}) \equiv \frac{p_{T,1} - p_{T,2}}{p_{T,1} + p_{T,2}} \quad (3.8)$$

where  $p_{T,1,2}$  are the transverse momenta of the two leading jets. A Gaussian fit to  $A(p_{T,1}, p_{T,2})$  results in a width  $\sigma(A)$  which can be used to characterise the asymmetry distribution. The relationship between  $\sigma(A)$  and fractional jet resolution is given by

$$\sigma(A) = \frac{\sqrt{\sigma^2(p_{T,1}) + \sigma^2(p_{T,2})}}{\langle p_{T,1} + p_{T,2} \rangle} \simeq \frac{1}{\sqrt{2}} \frac{\sigma(p_T)}{p_T} \quad (3.9)$$

where  $\sigma(p_T, 1) = \sigma(p_T, 2) = \sigma(p_T)$ , as the jets are both in the same  $y$  region. The requirement to ensure that only jets in back-to-back event topologies are included is satisfied using an azimuthal cut between leading jets -  $\Delta\phi(j_1, j_2) \geq 2.8$ . An additional

cut on the momentum of the third jet  $p_T^{EM} < 10 \text{ GeV}$ . A final safeguard is the soft radiation correction, which is applied to take into account the presence of soft particle jets which were not detected by the calorimeter. The size of this correction varies with the average  $p_T$  of the two leading jets in the events,  $\bar{p}_T = (p_{T,1} + p_{T,2})/2$ . For  $\bar{p}_T = 50 \text{ GeV}$  it can be up to 25% and can drop to  $\sim 5\%$  for  $\bar{p}_T = 400 \text{ GeV}$  [69].

### 3.6 Jet Cleaning

Reco jets can come from the hard proton-proton collisions which are the focus of this analysis, or from other unwanted background processes not related to the  $pp$  collisions, arising from the way jet algorithms function. The techniques that have been developed for iterative cone jet reconstruction involve first subtracting the underlying event energy within the calorimeter. But background fluctuations can persist after this process and so a stable cone, as defined by the algorithm, can arise from such remaining random or correlated background [82]. In studying any aspect of jets and their modification, such fake jets must be tagged and removed from the data sample. It is, therefore, necessary to study the characteristics of fake jets so as to extract a sample of jets with high purity. Distinguishing between these processes is vital. ATLAS achieves this with the selection criteria collectively known as jet cleaning [83]. There are three types of background these cuts aim to suppress:

- **Cosmic ray showers:** Cosmic rays can be produced by atmospheric interactions of ordinary atomic nuclei and elementary particles that have been accelerated to very high energies, originating from the Sun or elsewhere in the galaxy. The location of the ATLAS detector 100 m below ground provides shielding from most of these showers but some of the high energy muons produced can penetrate the Earth far enough to be detected.
- **Calorimeter noise:** Occasionally individual calorimeter cells will malfunction, and these isolated cells can sometimes produce large scale noise in ATLAS.

These pathological cells are masked either permanently or on an event-by-event basis if they only sporadically contribute noise. A small amount of calorimeter noise will escape these data quality measures and must be removed later by additional checks.

- **Beam-induced Background (BIB)** [84]: The beam pipe is not a perfect vacuum. This means some scattering does take place between protons and gas particles, leading to background in the detector. Protons that fly too far from the main beam-line are hard to remove and form a beam halo that can also contribute, since some fraction of it will interact with the collimators around ATLAS. Showers can then be produced that may interact with the calorimeter.

Jet quality variables that can discriminate between fake and good jets must be defined, and this is done on the basis of calorimeter signal pulse shapes, track-based variables and energy ratios that act as effective quality indicators. They are described in greater detail below.

### Calorimeter noise variables

The ionisation signal shape in liquid argon (LAr) calorimeters is well-understood. Its characteristic shape can be used to distinguish between real and fake energy deposits. The calorimeters that use LAr are the forward, hadronic end-cap and EM calorimeters. Simulations of the response of these electronics are used to model the expected pulse, allowing comparisons between this and the measured pulse shapes. The discrimination is quantified by the quadratic difference between pulse shapes in Equation 3.10.

$$Q_{\text{cell}}^{\text{LAr}} = \sum_{j=1}^4 (s_j - A(g_j - \tau g'_j))^2 \quad (3.10)$$

where  $A$  is the amplitude of the signal,  $\tau$  is the time spread of the signal,  $s_j$  is the amplitude of the four samples in ADC counts,  $g_j$  is the normalised predicted ionisation

shape with derivative  $g'_j$ . From this value  $Q_{\text{cell}}^{\text{LAr}}$  several jet-level quantities are defined:

- $\langle Q_{\text{cell}}^{\text{LAr}} \rangle$  is the normalised average jet quality. In other words it is the energy-squared weighted average of the pulse quality of the calorimeter cells in the jet.
- $f_Q^{\text{LAr}}$  is the fraction of energy deposited in the LAr calorimeter cells with poor signal quality shape. The threshold for poor quality is defined as  $Q_{\text{cell}}^{\text{LAr}} > 4000$
- $f^{\text{HECQ}}$  is the fraction of energy deposited in the hadronic calorimeter cells with poor signal shape quality. The threshold for poor quality is defined as  $Q_{\text{cell}}^{\text{LAr}} > 4000$

The calorimeter cells that emit only sporadic noise can nonetheless generate large fake energy and negative energy deposits. If the energy of all cells with negative energy are summed to give the quantity  $E_{\text{neg}}$ , this can also be used as a discriminator since it has a different distribution for good and fake jets. Negative energy in good jets is due to electronic and pile-up noise rather than faults in the calorimeters. The ease with which this allows good and fake jets to be distinguished is evident in Figure 3.11 - the differences are significant.

Fake jets are selected from events with at least one jet with  $p_T > 70$  GeV. Since events with fake jets are characterized by jets with unbalanced transverse momentum, only events satisfying  $H_T^{\text{miss}} = |\vec{H}_T^{\text{miss}}| > 70$  GeV are retained. The variable  $|\vec{H}_T^{\text{miss}}|$  is defined as  $|\vec{H}_T^{\text{miss}}| = \sum_{\text{jets}} \vec{p}_T$  where all jets with  $p_T$  greater than 20 GeV are considered. In addition, the direction of  $|\vec{H}_T^{\text{miss}}|$  should be opposite to the transverse component of the jet momentum, and the leading jet is required to be out-of-time ( $|t_{\text{jet}}| > 6$  ns), where the jet time ( $t_{\text{jet}}$ ) is defined by the energy-squared weighted average of the time of the energy deposits in the jet. The latter reduces the contribution from physics processes like  $Z$ +jets. Jets produced in  $pp$  collisions are expected to be reconstructed at  $t_{\text{jet}} = 0$ . These selection criteria result in a jet sample dominated by non-collision backgrounds, the ‘fake jets enriched’ sample.

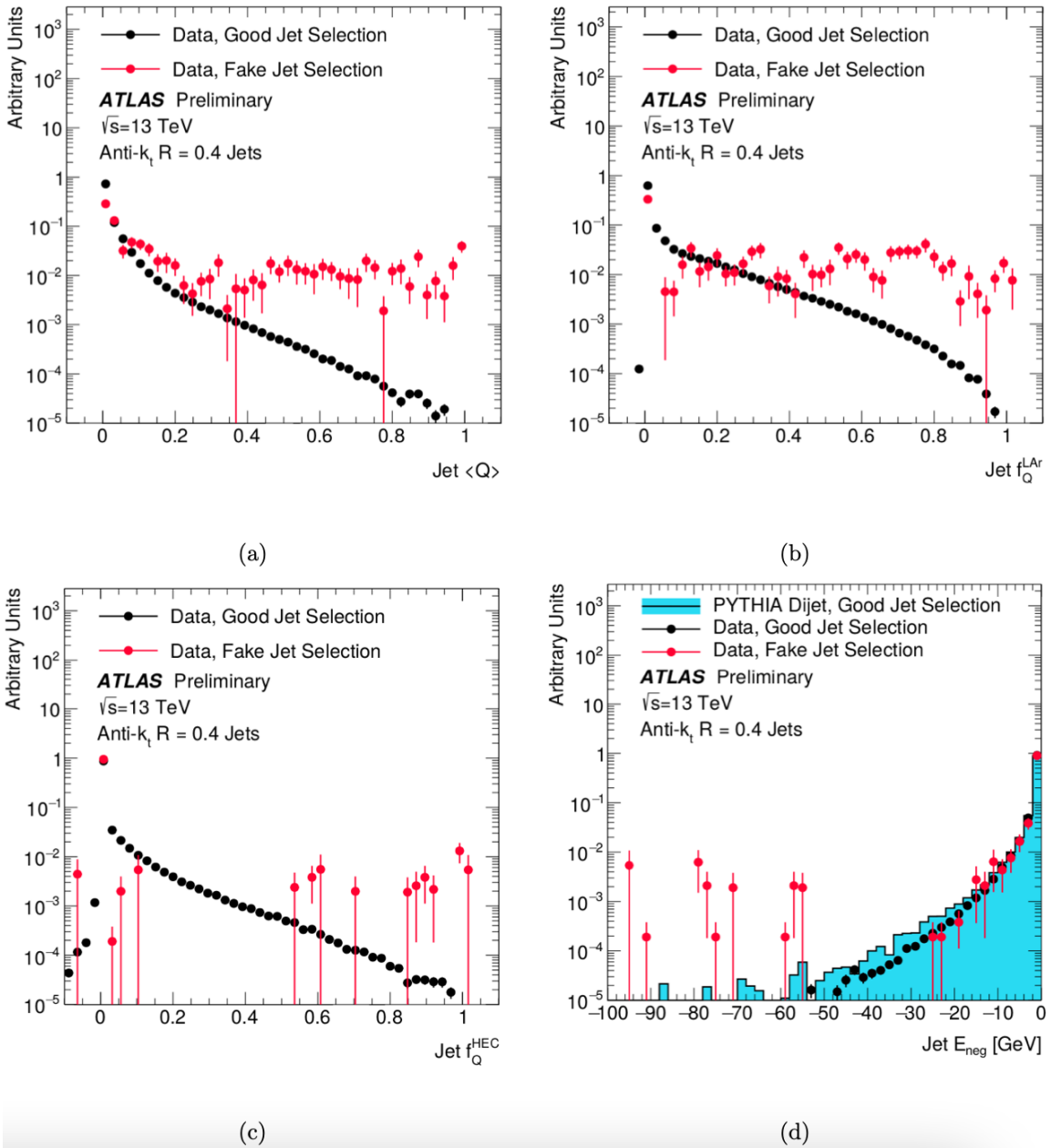


Figure 3.11: Variables used to distinguish between good and fake jets. (a)  $\langle Q \rangle$  (b)  $f_Q^{LAr}$ , (c)  $f_Q^{HEC}$  and (d)  $E_{neg}$ . Good jets in 2015 data are shown by black points with simulation results in blue in (d), along with a sample enriched with fake jets from 2015 data in red points. Differences are significant and so allow easy differentiation. From [83].

## Energy Ratio Variables

The effect of BIB and calorimeter noise is generally to produce more longitudinally localised jets compared to those from pp collisions. Useful variables can be defined that will show significant differences between fake and good jets, taking advantage of the BIB and calo noise differences.

- $f_{\text{EM}}$ : The EM fraction is the ratio of jet energy deposited in the EM calorimeter to the total energy of the jet.
- $f^{\text{HEC}}$ : The ratio of jet energy deposited in the hadron calorimeter to the total energy of the jet.
- $f_{\text{max}}$ : The maximum energy fraction in any given layer of the calorimeter.

These variables produce a smooth and predictable distribution when plotted for good jets, as shown in Figure 3.12. Also in Figure 3.12 is the contrasting uneven distribution of fake jets.

## Track based variables

Good jets generally contain charged hadrons which are reconstructed by the inner tracker and TRT. Track variables in the ID tracking system have been found to be useful in defining several discriminatory parameters, which allow good separation of good and fake jets. These are for example  $f_{ch}$ , the ratio of the jet charged particle fraction, to the jet energy fraction  $f_{\text{max}}$  of the layer where maximum energy was deposited.  $f_{ch}$  is the ratio of the scalar sum of  $p_T$  of tracks from the primary vertex associated with the jet, divided by jet  $p_T$ .

These variables are plotted in data and MC in Figure 3.13, which shows they are effective discriminants. Data and MC are in strong agreement with significant deviations by fake jets.

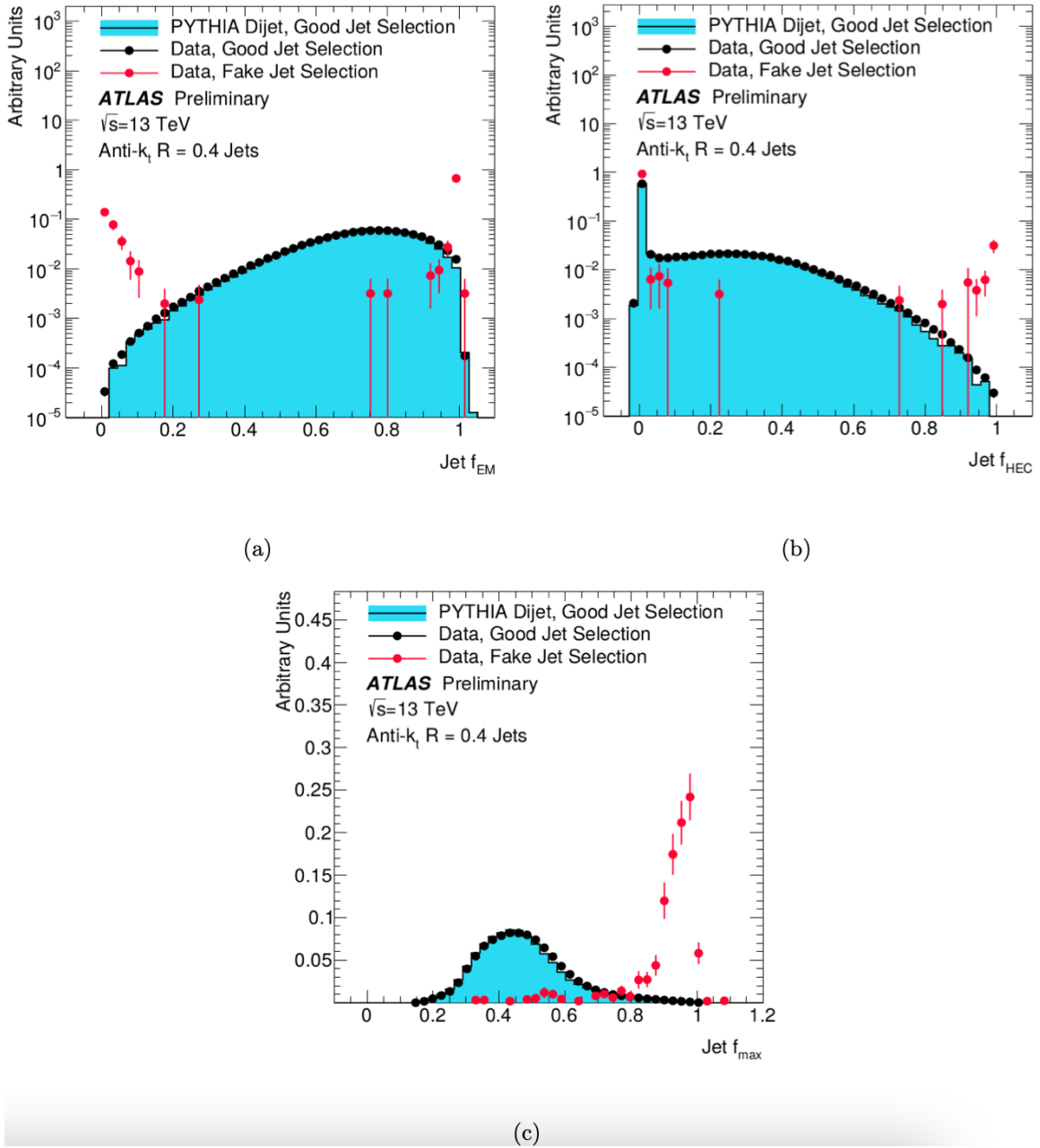


Figure 3.12: Distributions of the energy ratio variables, defined to identify the difference between fake and good jets. (a)  $f_{EM}$ , (b)  $f_{HEC}$  and (c)  $f_{max}$  for good jets in 2015 data, shown in black points, the simulation (blue shaded histograms) and a sample enriched with fake jets from 2015 data denoted with red points [83].

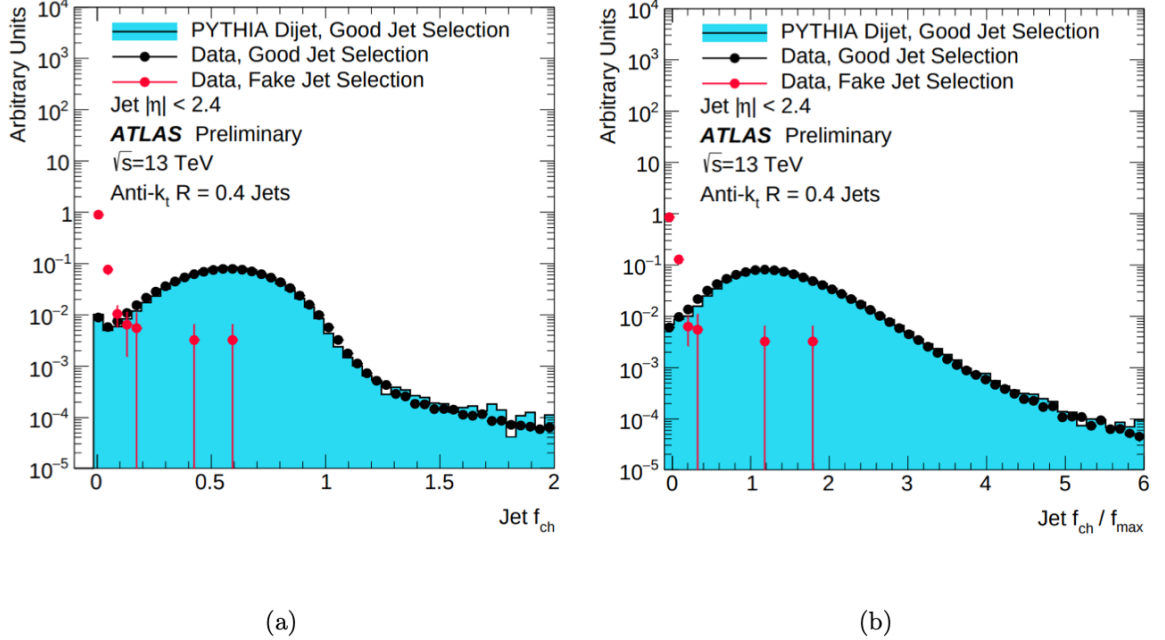


Figure 3.13: Distributions of (a)  $f_{ch}$  and (b)  $f_{ch}$  and  $f_{max}$ . Efficiency is high in the good jets enriched samples from data in black points and also for simulation in blue shaded histograms. Deviations of the fake jet enriched samples in red points from both data and MC are significant [83].

Figure 3.14 shows  $f_{ch}$  as a function of  $f_{EM}$  in good- and fake-jet enriched samples. This variable has high efficiency in differentiating between good and fake jets across the range, as they generally have  $f_{ch}$  close to 0 and  $f_{max} \sim 1$ , while good jets have  $f_{ch} > 0$  and  $f_{max} < 1$ .

### 3.7 Quality Cuts

There are two main types of selection used in ATLAS to separate fake jets from good jets. They are called LooseBad and TightBad, and are based on the jet variables described above. The dijet analysis uses the LooseBad criteria. This selection was introduced in [84], [71], though under the name ‘looser’, with the aim of providing high good jet efficiency with an optimised level of fake jet rejection. A jet is labelled as LooseBad and excluded if it satisfies any of the following criteria:

- $f_{HEC} > 0.5$  and  $|f_Q^{HEC}| > 0.5$  and  $\langle Q \rangle > 0.8$

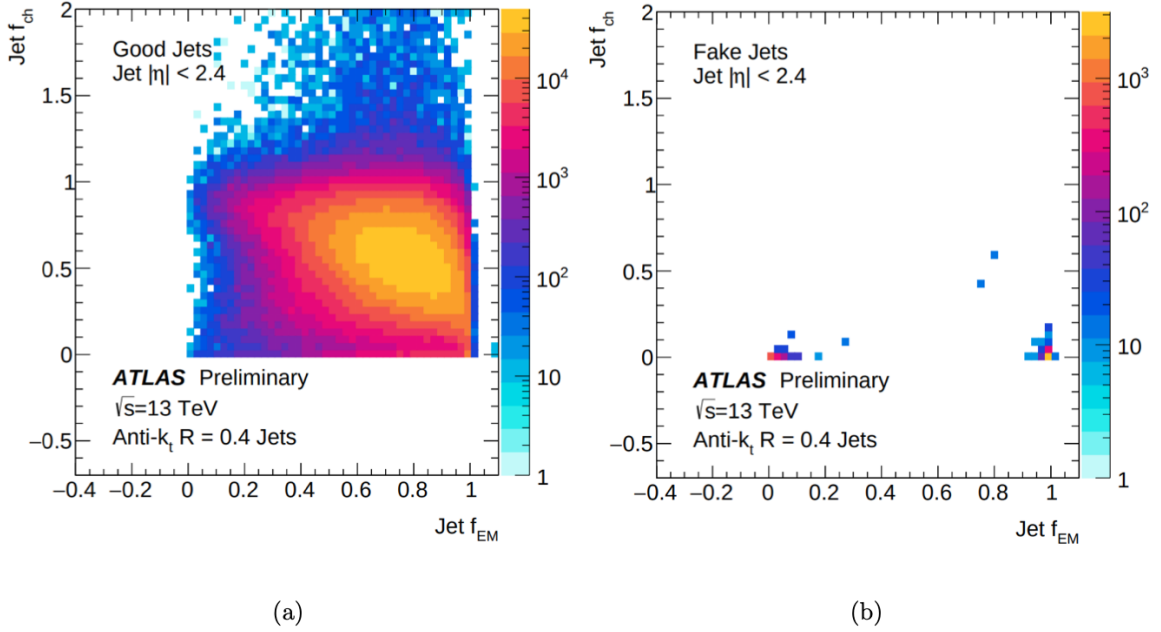


Figure 3.14:  $f_{ch}$  as a function of the EM fraction  $f_{EM}$  for (a) good jets and (b) samples enriched with fake jets. From [83].

- $E_{neg} > 60 \text{ GeV}$
- $f_{EM} > 0.95$  and  $f_Q^{LAr} > 0.8$  and  $|\eta| < 2.8$
- $f_{max} > 0.99$  and  $|\eta| < 2$
- $f_{EM} < 0.05$  and  $f_{ch} < 0.05$  and  $|\eta| < 2$
- $f_{EM} < 0.05$  and  $|\eta| \geq 2$

The first two criteria identify fake jets from sporadic noise bursts in the HEC. The third set of criteria filters out coherent EM calorimeter noise and isolated pathological cells. The remainder are aimed at identifying more general noise sources like BIB, cosmic ray muons and other hardware issues.

The TightBad selection provides a much higher rejection of fake jets, at the cost of an inefficiency in good jet selection of up to a few percent [83]. It adds a single additional criterion:

- $f_{ch}/f_{max} < 0.1$  for  $|\eta| < 2.4$

The jet cleaning cuts applied in this analysis are shown in Table 3.5.

### 3.8 Monte Carlo Samples

A Monte Carlo method is any that uses (pseudo!) random numbers and probability statistics, in this case to simulate particle collisions. Searches for beyond Standard Model physics at ATLAS involve comparing data to predictions based on the Standard Model. The event generators that make these predictions use a series of complex parton shower, hadronisation and multi-interaction models to enhance fixed-order parton-level matrix element events. In this analysis generators used have included Pythia, SherpaCSS/SherpaLund and Herwig. Excellent knowledge of the underlying physics and detector technology is required to simulate events such that they are close to actual collider data. The basis of these models are often approximations of high-multiplicity perturbative QCD calculations, or alternatively a phenomenological approach may be needed in the non-perturbative regime where the physics is not well-understood based on first principles.

There are several free parameters which must be optimised if a good description of measured observables is to be obtained. This process is referred to as tuning, and multiple sets of tunes are available to suit specific event topologies and observables. The set used in the dijet analysis is part of the ATLAS 2014 (A14) tune series [85], which is made up of four tunes performed on leading-order parton density functions with the labels CTEQ6L1 [86], MSTW2008LO [87], NNPDF23LO [88] and HERA-PDF15LO [89]. The dijet analysis employs specifically the A14NNPDF23LO PDF set. Systematic variations on this tune have been done using the ‘eigentunes’ method [90] in order to obtain estimates of the systematic uncertainties associated with the MC modelling. The data from which this tuning was generated includes a number of ATLAS observables with demonstrated sensitivity to the underlying event, jet track properties [91] and other substructure variables [92].

The full simulation must also take into account the interactions of the final-state

<b>Jet Reconstruction Parameters</b>	
Parameter	Value
Algorithm	anti- $k_t$
R-parameter	0.4
Input Constituent	EMTopo
Analysis Release Number	21.2.121
CalibArea tag	00-04-82
Calibration Configuration	JES_MC16Recommendation_Consolidated_-EMTopo_Apr2019_Rel21.config
Calibration Sequence (Data)	JetArea_Residual_EtaJES_GSC_Insitu
Calibration Sequence (MC)	JetArea_Residual_EtaJES_GSC_Smear
Calibration Configuration (AFII)	JES_MC16Recommendation_AFII_EMTopo_-Apr2019_Rel21.config
Calibration Sequence (AFII)	JetArea_Residual_EtaJES_GSC
<b>Selection Requirements</b>	
Observable	Requirement
Jet Cleaning	LooseBad
Batman Cleaning	No
$p_T$	$> 150$ GeV
$ \eta $	$< 5.0$ GeV

Table 3.5: Jet selection criteria for the dijet analysis

hadrons with the ATLAS detector. MC events are therefore passed to the GEANT4 toolkit [93], which simulates the response of the detector. It takes into account the scattering of different types of particles in different detector materials and probabilistically calculates decay paths from knowledge of lifetimes and branching ratios. GEANT4 also models particle interactions with the readout electronics and outputs digitised signals from each simulated detector component. These MC signals can be processed with the same reconstruction software as for real data to give a full understanding of what the resulting measurements would be.

### 3.9 Data/MC comparisons

The final MC simulation output, including GEANT4 modeling, is compared to a selection of observables in Figures 3.15-3.18. There is good agreement for all variables with the exception of the number of primary vertices NPV in Figure 3.17b. This is due to pile-up in the detector. Other slight differences are due to the MC not fully representing the run conditions of the data. Figure 3.15 shows data/MC comparisons for difference in jet angle  $\Delta\phi$ , the scalar sum of jet momentum, jet energy and jet angles in  $\eta$  and  $\phi$ . Several other kinematic variables are also shown - recall that  $y^*$  is based on the difference in rapidities of two jets and was discussed in Chapter 2.

There is often an imbalance in jet longitudinal momenta due to the differing momenta of the colliding particles, resulting in a boost with respect to the lab reference frame. The boost  $y_B$  is defined in Equation 3.11.

$$\begin{aligned} y_B &= \frac{y_1 + y_2}{2} \\ &= \frac{1}{2} \ln\left(\frac{x_1}{x_2}\right) \end{aligned} \tag{3.11}$$

The most important quantity for the dijet analysis is the dijet invariant mass  $m_{jj}$ , defined in Equation 3.12.

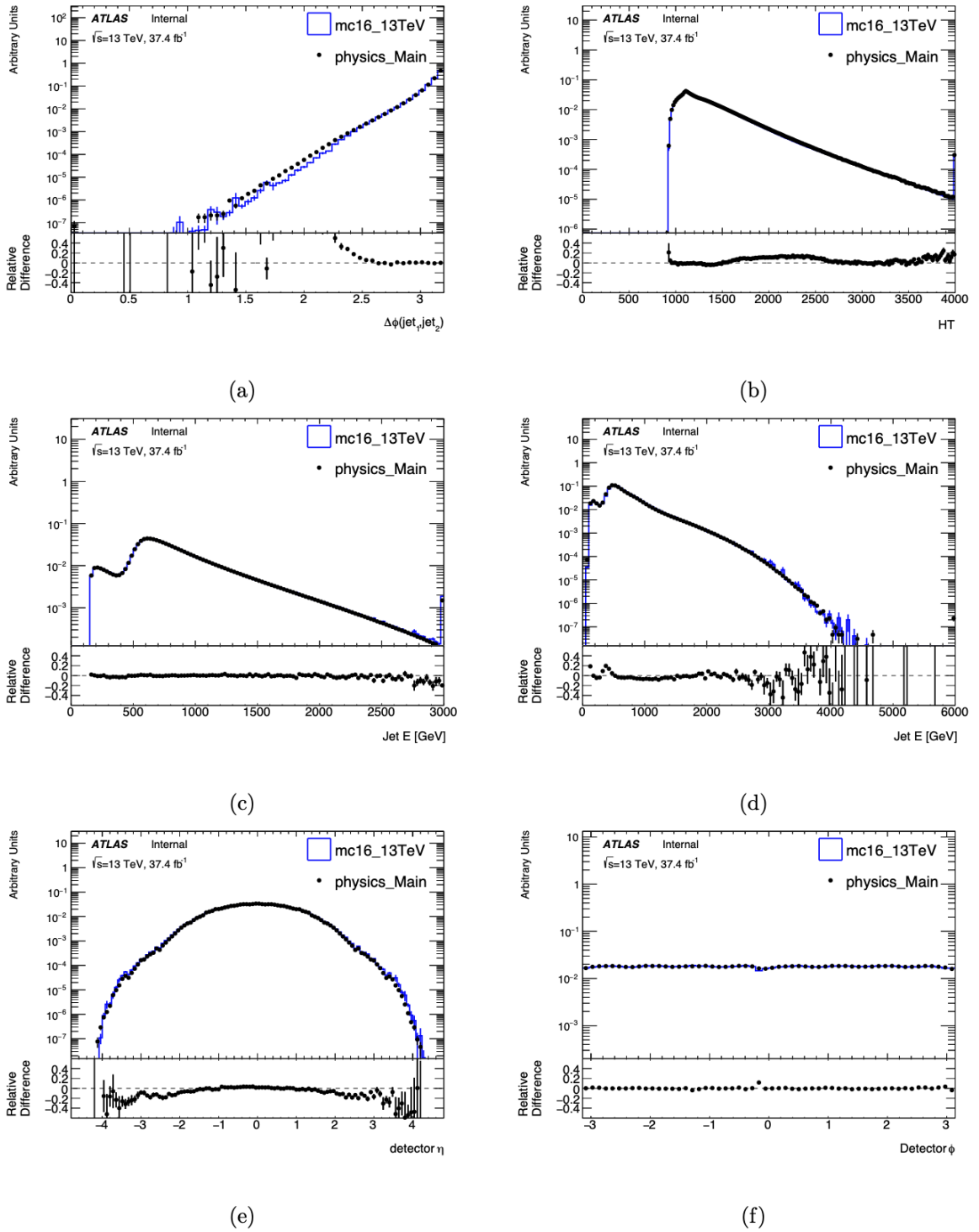
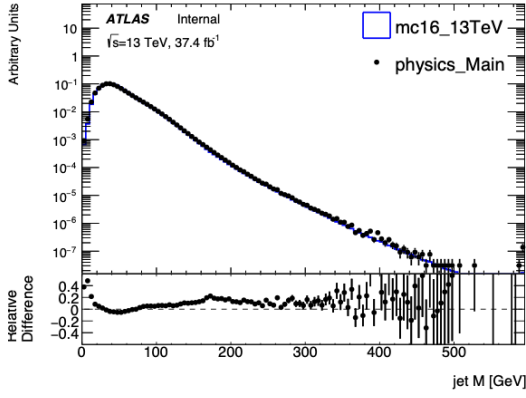
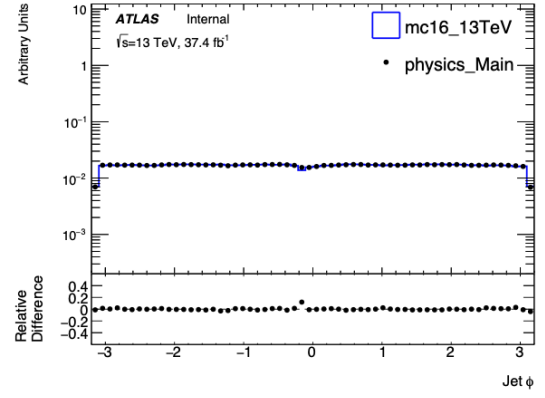


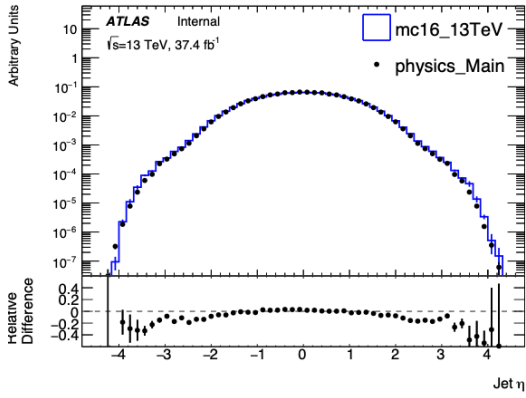
Figure 3.15: Data-MC comparisons for (a) jet angle  $\Delta\phi$ , (b) the scalar sum of jet  $p_T$  (HT), (c) jet energy  $E$ , (d) jet energy at the EM scale and (e,f) jet angle  $\eta, \phi$  in the detector.



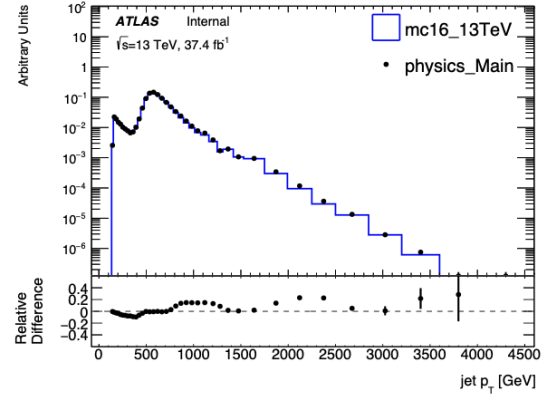
(a)



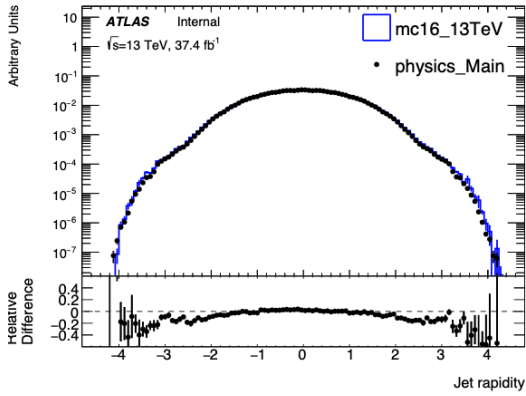
(b)



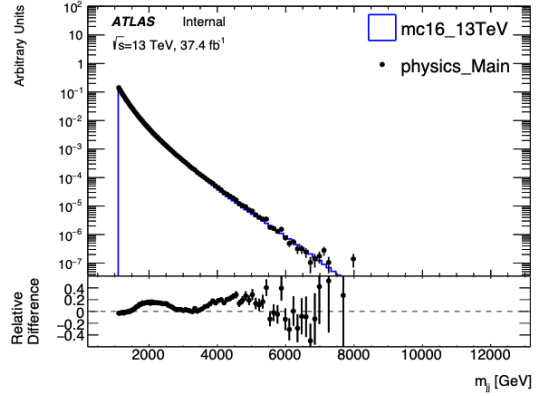
(c)



(d)

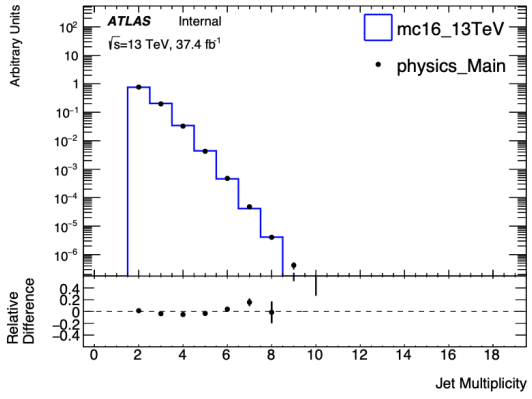


(e)

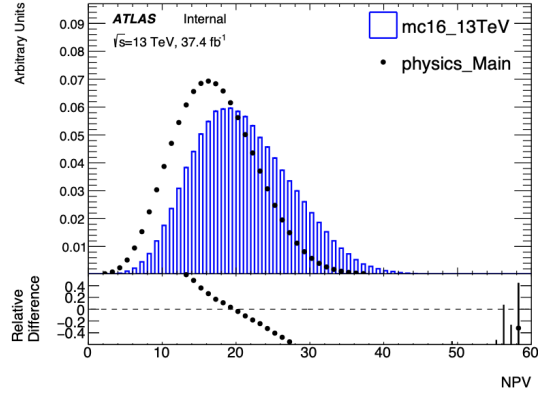


(f)

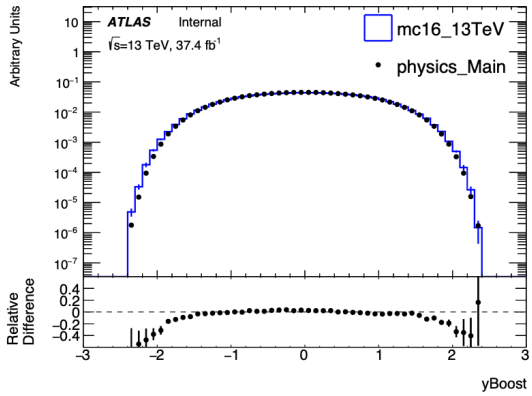
Figure 3.16: Data-MC comparisons for (a) jet multiplicity, (b) reconstructed jet angle  $\phi$ , (c) reconstructed jet angle  $\eta$ , (d) jet  $p_T$ , (e) jet rapidity and (f) dijet invariant mass  $m_{jj}$  [94].



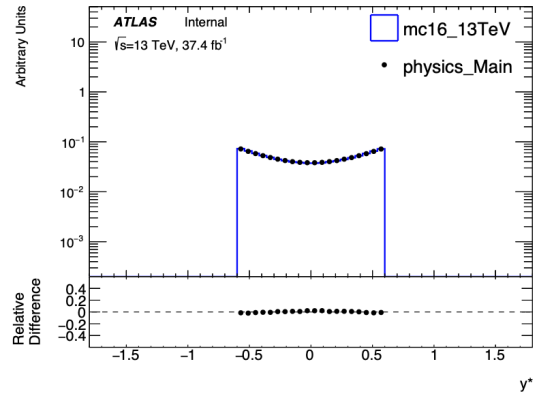
(a)



(b)

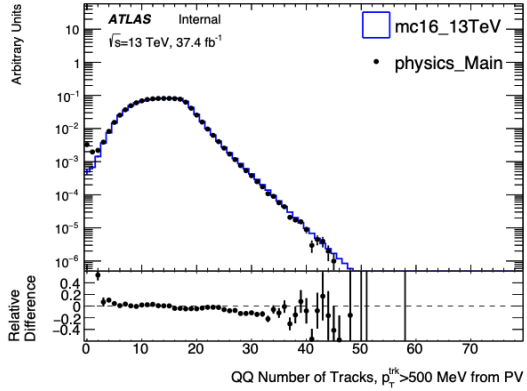


(c)

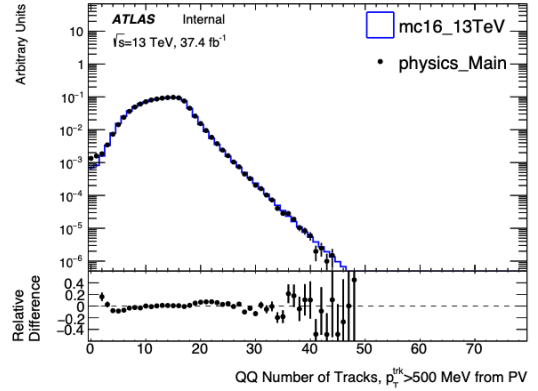


(d)

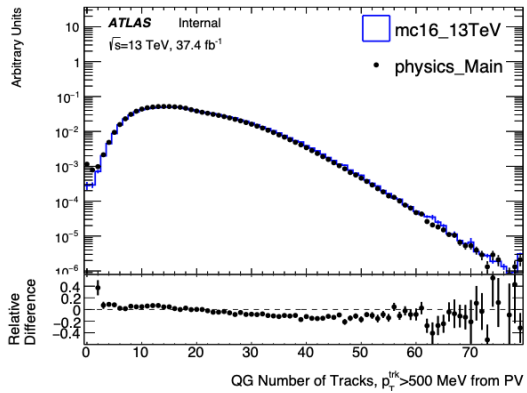
Figure 3.17: Data-MC comparisons for (a) number of jets, (b) number of primary vertices, (c) rapidity boost and (d) the angular separation  $y^*$  of the two jets [94].



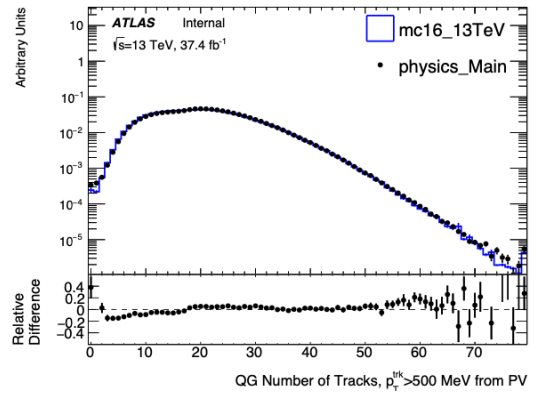
(a)



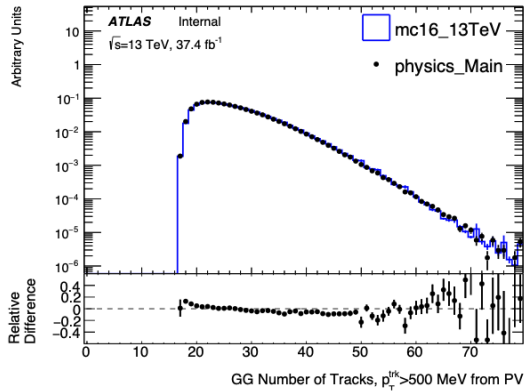
(b)



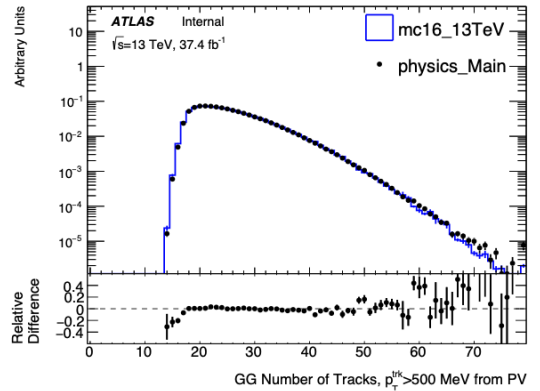
(c)



(d)



(e)



(f)

Figure 3.18: Data-MC comparisons of charged track multiplicity for  $QQ$  in (a) and (b),  $QG$  in (c) and (d) and  $GG$  in (e) and (f) [94].

$$m_{jj} = \sqrt{(E_1 + E_2)^2 - |\vec{p}_1 + \vec{p}_2|^2} \quad (3.12)$$

where  $E_1, \vec{p}_1$  and  $E_2, \vec{p}_2$  are the energy and momentum of leading and subleading jets.  $m_{jj}$  is a Lorentz invariant quantity and can also be expressed as

$$m_{jj} = \sqrt{\hat{s}} = 2p_T \cosh y^* \quad (3.13)$$

where  $\hat{s}$  is one of the Mandelstam variables  $(p_1 + p_2)^2$ .

The cumulative effect of applying all the quality cuts for the analysis in this thesis is shown in Table 3.6, after which  $\sim 5.5$  million events are accepted.

Selection criteria	$N_{\text{events}}$	Relative percentage	Cumulative percentage
No Cuts	4403665748		
GRL	4291728423	97.46	97.46
LAr	4287690715	99.91	97.37
Tile	4287644293	100.00	97.37
SCT	4287390142	100.00	97.36
Core	4287390142	100.00	97.36
Jet Cleaning	4230810790	98.68	96.10
NPV	4230801918	100.00	96.10
Trigger HLT $_j360 _j380 _j400 _j420 _j440$	370897862	8.77	8.42
JetSelect ( $p_T > 150$ GeV, $ \eta  < 5.0$ , $n_{\text{jet}} \geq 2$ )	363879632	98.11	8.26
Trigger HLT j420	250268296	68.78	5.68
$ \Delta\phi  > 1.$	250201845	99.97	5.68
$ y^*  < 0.6$	135532014	54.17	3.08
$m_{jj} > 1100$ GeV	27407919	20.22	0.62
Jet $ \eta  < 2.1$	27029730	98.62	0.61
$\geq 1$ gluon tag	19075078	70.57	0.43
2 gluon tag	5538257	29.03	0.13
$ y^*  < 0.8$	172691209	69.02	3.92
$m_{jj} > 1200$ GeV	28276748	16.37	0.64
Jet $ \eta  < 2.1$	27553578	97.44	0.63
$\geq 1$ gluon tag	19339165	70.19	0.44
2 gluon tag	5583092	28.87	0.13

Table 3.6: Cutflow for this analysis applied to full Run2 Data (2015-2018).

# Chapter 4

## Quark-Gluon Tagging

### 4.1 Expected Signal Significance

Quark-gluon tagging is the practice of labelling jets as either quark-initiated or gluon-initiated. A good measure of the effectiveness of applying such selections is the expected signal significance. This is calculated based on the composition of the  $q^*$ ,  $H'$  and strings signal models, the background simulations and the expected selection efficiencies. In this section it is assumed that a cut can be applied that has a constant gluon selection efficiency as a function of mass. This is demonstrated to be true in the next section.

#### 4.1.1 GG Selection

The simplest case to consider is that of a  $gg$  final state, which is the expected final state of  $H'$  model. The inputs for the significance calculation are the efficiency at which truth quark and gluon jets are selected by the tagger,  $\epsilon_{qQ}$ ,  $\epsilon_{gQ}$  ( $\epsilon_{qG}$ ,  $\epsilon_{gG}$ ), are the efficiency of a quark initiated jet passing the quark (gluon) selection criteria and the efficiency of a gluon initiated jet passing the quark (gluon) selection criteria respectively. The efficiencies for the  $H'$  are shown in Table 4.1.

The expected significance for a GG signal selection for the  $H'$  model against a

$\epsilon_{qQ}$	$\epsilon_{gQ}$	$\epsilon_{qG}$	$\epsilon_{gG}$
0.9	0.6	0.9	0.46
0.8	0.37	0.86	0.39
0.7	0.24	0.79	0.31
0.6	0.15	0.75	0.27
0.5	0.09	0.7	0.23
0.4	0.05	0.65	0.2
0.3	0.03	0.6	0.17

Table 4.1: The efficiency of truth quark and gluon jet selection by the quark (gluon) selection  $\epsilon_{qQ}$ ,  $\epsilon_{gQ}$  ( $\epsilon_{qG}$ ,  $\epsilon_{gG}$ ). E.g. at a truth quark efficiency of 0.9, the truth gluon efficiency is 0.6.

QCD background is given by

$$S_{H'} = N_S \sum_i \frac{f_{qq_i} \epsilon_{qG}^2 + f_{qg_i} \epsilon_{qG} \epsilon_{gG} + f_{gg_i} \epsilon_{gG}^2}{\sqrt{B_{qq_i} \epsilon_{qG}^2 + B_{qg_i} \epsilon_{qG} \epsilon_{gG} + B_{gg_i} \epsilon_{gG}^2}} \quad (4.1)$$

where  $N_S$  is the expected number of signal events,  $f_{xx_i}$  is the fraction of signal events that produce  $qq$ ,  $qg$  and  $gg$  jet events in the mass bin  $i$ . For the  $H'$ , this mostly consists of  $gg$  events.  $B_{xx_i}$  is the number of background events producing  $qq$ ,  $qg$  and  $gg$  jet events in mass bin  $i$ , where the total number of events is normalised to three size of the data set collected during data taking in 2015 and 2016. The resulting significance can be compared to the expected significance of applying no selection to data for  $H'$  masses of 2-7 TeV in steps of 0.5 TeV. The results of performing this calculation are shown in Figure 4.1 and an improvement in significance of up to 40% is seen at high masses. This improvement is achieved using an  $n_{\text{track}}$  cut that gives gluon efficiency of  $\epsilon_{gG} = 0.8, 0.9$ , which results in a ‘gluon-enhanced’ sample.

### 4.1.2 QG Selection

Calculating significances for  $QG$  signal selection presents a greater challenge as it is possible for a jet to be simultaneously tagged as both a quark and a gluon jet. This

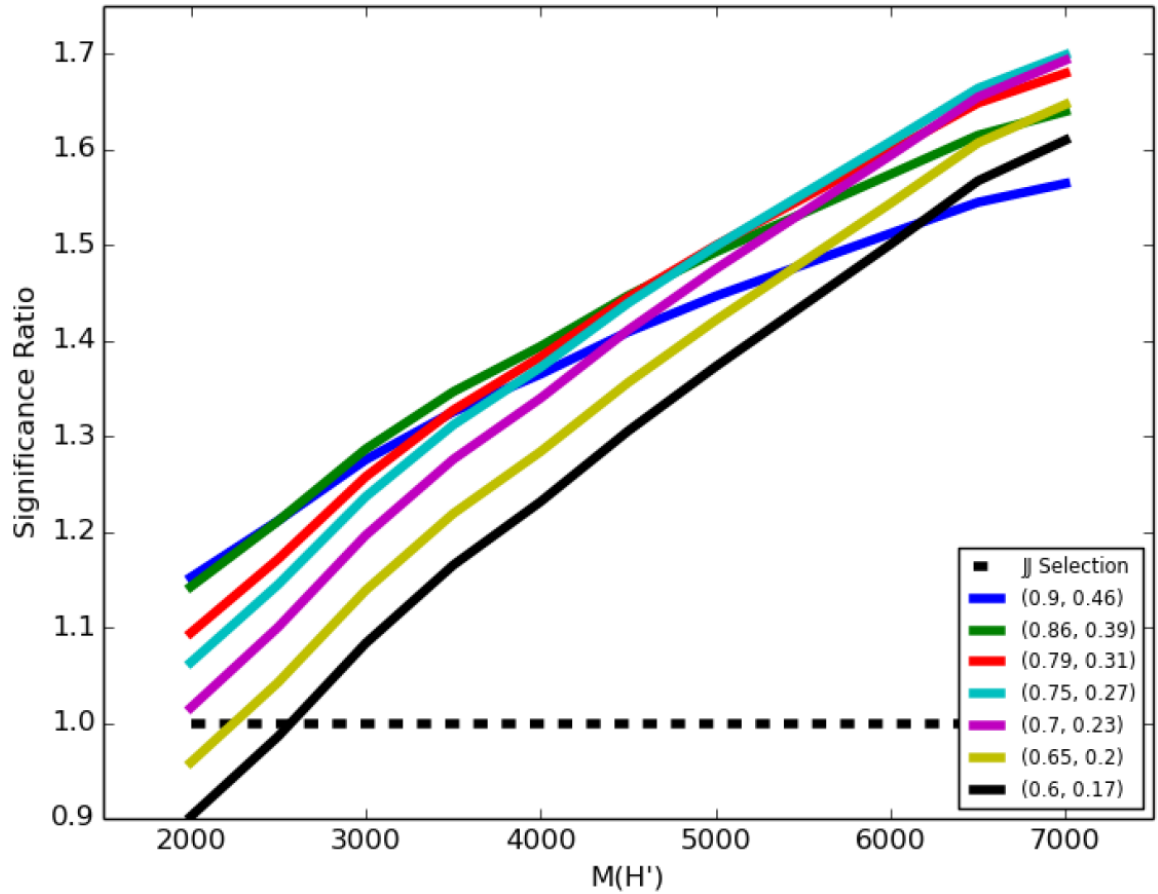


Figure 4.1: The expected significance for an  $H'$  with values of  $\epsilon_{gG}$  from 0.9 to 0.6, compared to the significance with no selection with the dashed line. Masses are in GeV and go up to the highest simulated signal mass for the  $H'$ , which for this analysis is 7 TeV [94].

type of signal thus has an additional category of jets resulting in a total of three categories, which will be labelled as  $Q_{only}$ ,  $QG$  and  $G_{only}$ . New efficiencies must now be defined:

- $\epsilon_{qQ_{only}}$ : the probability of a quark jet being identified as a quark jet only
- $\epsilon_{qQG}$ : the probability of a quark jet being identified as both a quark and gluon jet
- $\epsilon_{qG_{only}}$ : the probability of a quark jet being identified as a gluon jet only

By definition then  $\epsilon_{qQ_{only}} + \epsilon_{qQG} + \epsilon_{qG_{only}} = 1$ . A further set with  $q$  replaced by  $g$ ,  $\epsilon_{gQ_{only}}$ ,  $\epsilon_{gQG}$  and  $\epsilon_{gG_{only}}$  can also be defined. The fraction of truth samples that pass the selection can then be calculated as:

$$\begin{aligned}
\epsilon_{qq} &= 2\epsilon_{qQ_{only}}\epsilon_{qG_{only}} + \epsilon_{qQG} + \epsilon_{qQ_{only}}(\epsilon_{qQ_{only}} + \epsilon_{qG_{only}}) + \epsilon_{qQG}^2 \\
\epsilon_{qg} &= \epsilon_{qQ_{only}}(\epsilon_{qQG} + \epsilon_{qG_{only}}) + \epsilon_{qQG}(\epsilon_{qQ_{only}} + \epsilon_{qQG} + \epsilon_{qG_{only}}) \\
&\quad + \epsilon_{qG_{only}}(\epsilon_{qQG} + \epsilon_{qQ_{only}}) \\
\epsilon_{gg} &= 2\epsilon_{gQ_{only}}\epsilon_{gG_{only}} + \epsilon_{gQG}(\epsilon_{gQ_{only}} + \epsilon_{gG_{only}}) + \epsilon_{gQG}^2
\end{aligned} \tag{4.2}$$

Giving an overall significance of:

$$S_{q^*} = N_s \sum_i \frac{f_{qq_i}\epsilon_{qq} + f_{qg_i}\epsilon_{qg} + f_{gg_i}\epsilon_{gg}}{\sqrt{B_{qq_i}\epsilon_{qq} + B_{qg_i}\epsilon_{qg} + B_{gg_i}\epsilon_{gg}}} \tag{4.3}$$

The efficiencies are shown in Table 4.2.

The expected significance for the signal selection with the  $q^*$  model and QCD background is determined using the same previously described method. The results are shown in Figure 4.2. No improvements are observed.

This is for the case where quark and gluon selection efficiencies are set to be equal. If they are allowed to vary, some improvement is found, with best results for no selection on the gluon jet and tight selection on the quark jet - i.e. one jet must pass

$\epsilon_{qG_{only}}$	$\epsilon_{qQG}$	$\epsilon_{qG_{only}}$	$\epsilon_{gQG}$	$\epsilon_{gG_{only}}$	
0.52	0.39	0.1	0.1	0.51	0.39
0.66	0.14	0.2	0.2	0.19	0.61
0.7	0.0	0.26	0.24	0.0	0.7
0.6	0.0	0.19	0.15	0.0	0.6
0.5	0.0	0.1	0.05	0.0	0.5
0.4	0.0	0.1	0.05	0.0	0.4
0.29	0.0	0.07	0.02	0.0	0.3

Table 4.2: The efficiency for truth quark or gluon jets passing the QG selection  $\epsilon_{qq}$ ,  $\epsilon_{gQ}$  ( $\epsilon_{qG}$ ,  $\epsilon_{gG}$ )

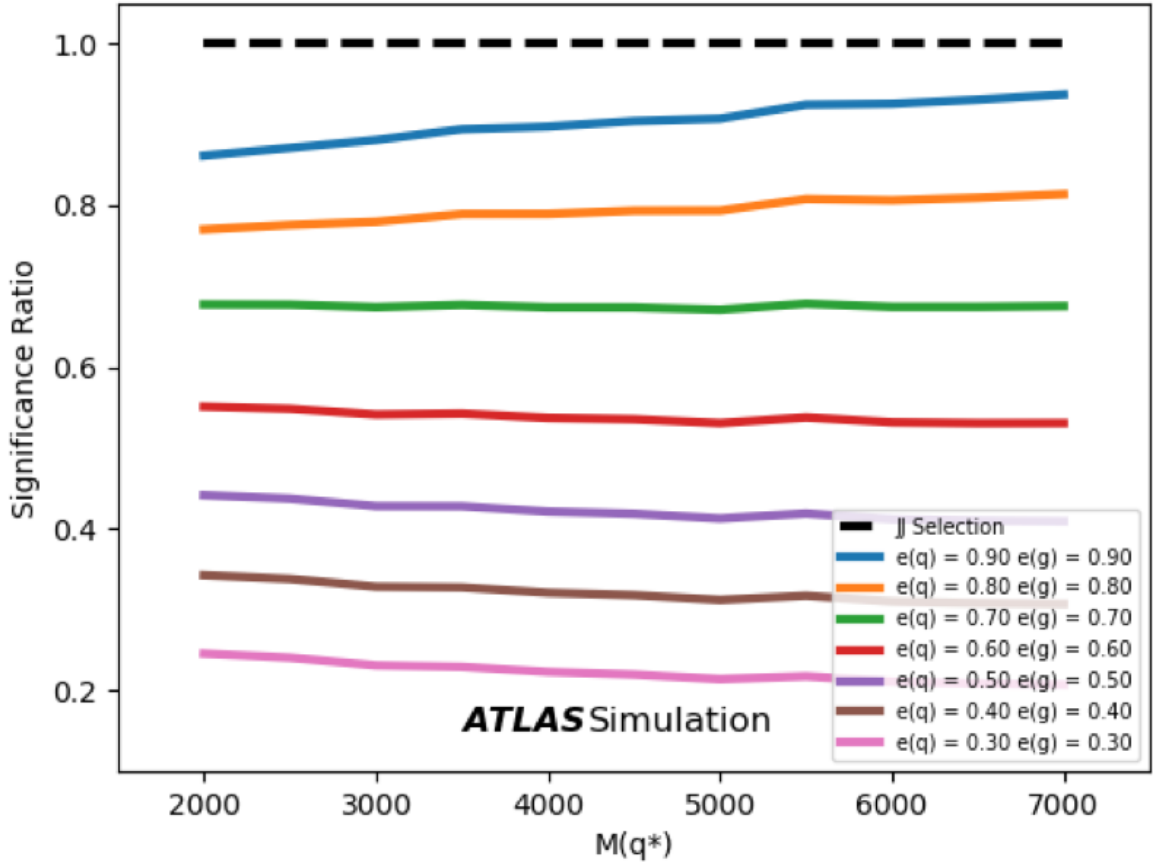


Figure 4.2: The expected significance for a  $q^*$  compared to the significance with no selection applied. The legend gives efficiency pairs  $(\epsilon_{qG}, \epsilon_{gG})$ . Masses are in GeV [94].

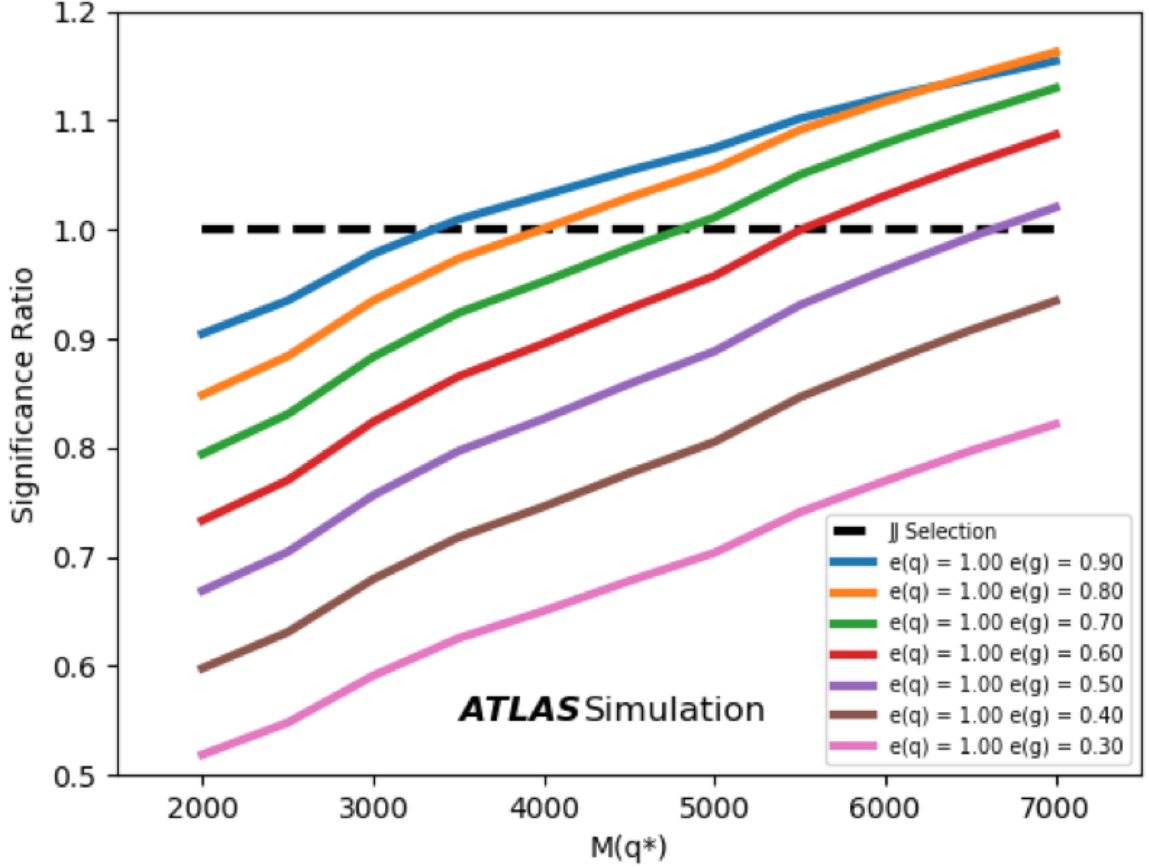


Figure 4.3: The expected significance for a  $q^*$  compared to the significance with no selection applied. The key gives efficiency pairs  $(\epsilon_{qG}, \epsilon_{qG})$ . Masses are in GeV [94].

quark selection criteria. The results are shown in Figure 4.3, with improvements of up to 25% seen for the high mass region.

## 4.2 Optimization of $y^*$

Samples can be further optimised by applying a variety of cuts. For example, the signal significance of strings (Figure 4.4) and the  $H'$  (Figure 4.5) are shown below. In QCD, 2-to-2 scattering the t-channel is dominant and dijet production is proportional to  $(1 - \cos(\theta^*))^{-2}$ . But for the  $H'$ , dijet production should be flat in  $\cos \theta^*$ , and string resonances exhibit a more complex dependence. As a result, the  $y^*$  of the QCD background will reach a minimum at 0 while the  $H'$  and strings peak. For strings signal samples, the significance peaks at about 0.8, giving an optimal cut of  $|y^*| < 0.8$ ,

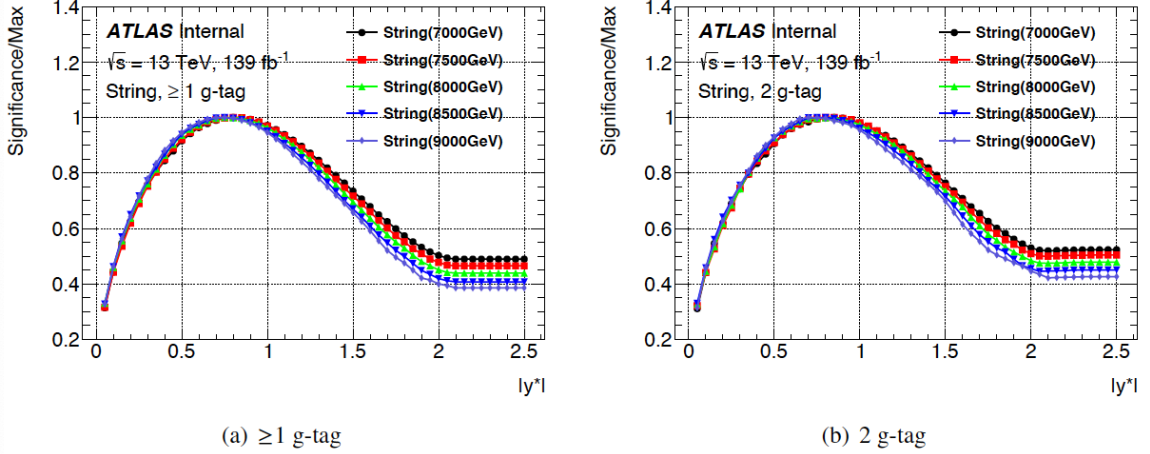


Figure 4.4: String significance as a function of the  $y^*$  cut for (a)  $\geq 1$  gluon-tag and (b) 2 gluon-tag [94].

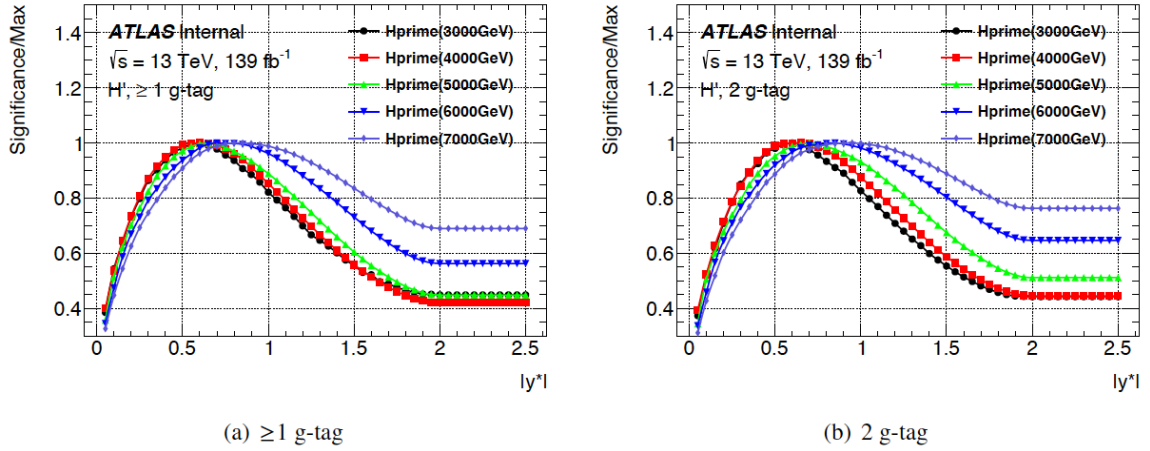


Figure 4.5:  $H'$  significance as a function of the  $y^*$  cut for (a)  $\geq 1$  gluon-tag and (b) 2 gluon-tag [94].

where for the  $H'$  the peak is earlier at  $|y^*| < 0.8$ .

The  $H'$  search requires the following additional cuts:

- $|y^*| < 0.6$
- $m_{jj} > 1100$  GeV

and for the search for string resonances:

- $|y^*| < 0.8$

- $m_{jj} > 1200 \text{ GeV}$

The cuts above define the inclusive sample, and for  $q/g$  tagging the following additional cuts are applied:

- Both jets must have  $|\eta| < 2.1$
- $\geq 1$  gluon tagged (75% gluon efficiency working point)
- 2 gluons tagged (75% working point)

where the selection criteria giving 75% gluon selection is  $n_{\text{track}} > -7.3 + 4.2 \ln(p_T)$ .

For all the above, it is assumed that the efficiency of selecting quark and gluon jets is the same for signal and QCD samples. This is true when the signal model has identical  $n_{\text{track}}$  distributions for both quark and gluon jets, which is the case in Pythia since version 8.301 since it incorporates a new coherent Vincia RF shower model [95].

### 4.3 Tagging Procedure

Quark-gluon tagging (q/g tagging) is the practice of labelling jets as either quark-like or gluon-like, based on characteristics that make it more likely they were initiated by quarks rather than gluons, or vice versa. The purpose of doing so is to maximise the signal/background ratio, since analyses often search for physics which is preferentially present in either quark or gluon jets. Taggers have been developed for this purpose, and can be optimised by comparing cross section limits obtained for different signal models. Samples enriched with either quark or gluon jets can then be created to make potential signals easier to detect. The potential for reducing background is highlighted in Figure 4.6, which shows the fraction of events with  $qq$ ,  $qg$  or  $gg$  jets. These are from simulations with a Pythia8 [96] and the leading-order NNPDF2.3 [97] PDFs. The number of tracks in a jet is an excellent discriminator [57] and the results of applying the tagger are shown in Figure 4.7.

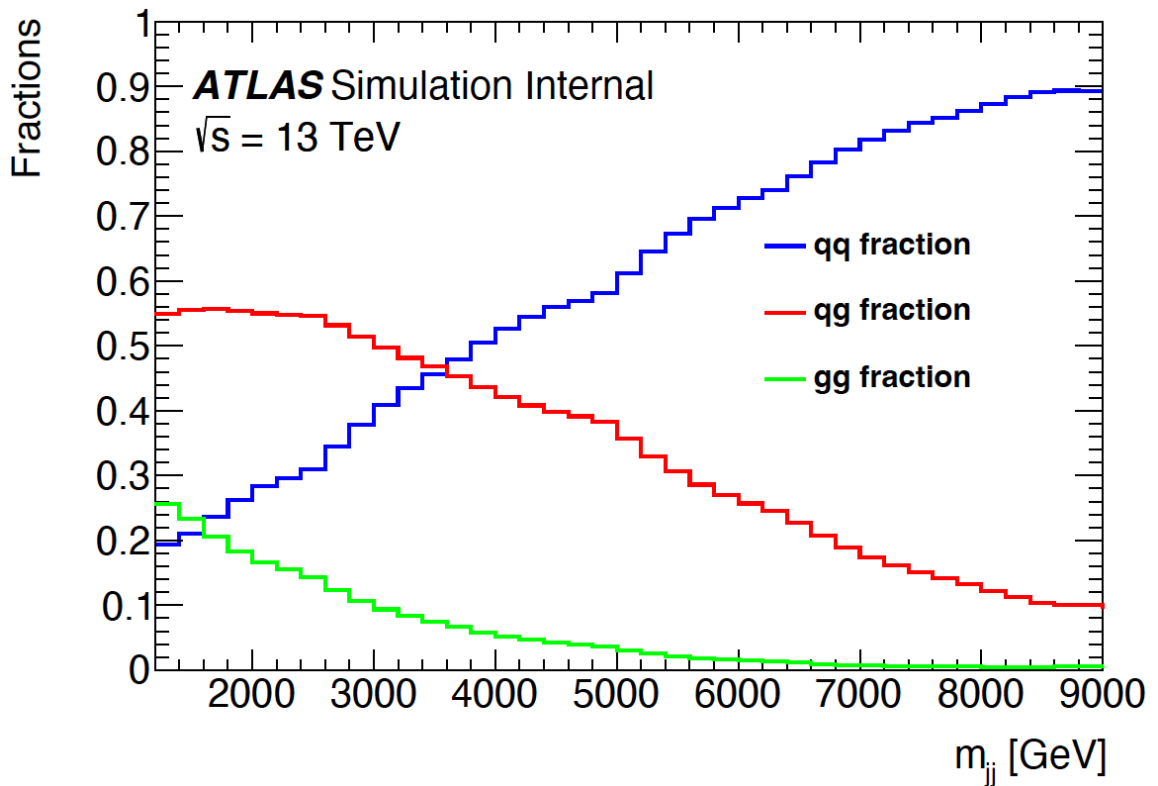


Figure 4.6: The fraction of dijet events that are initiated by quark-quark events (blue), quark-gluon events (green) and gluon-gluon events (red) in simulated data [94].

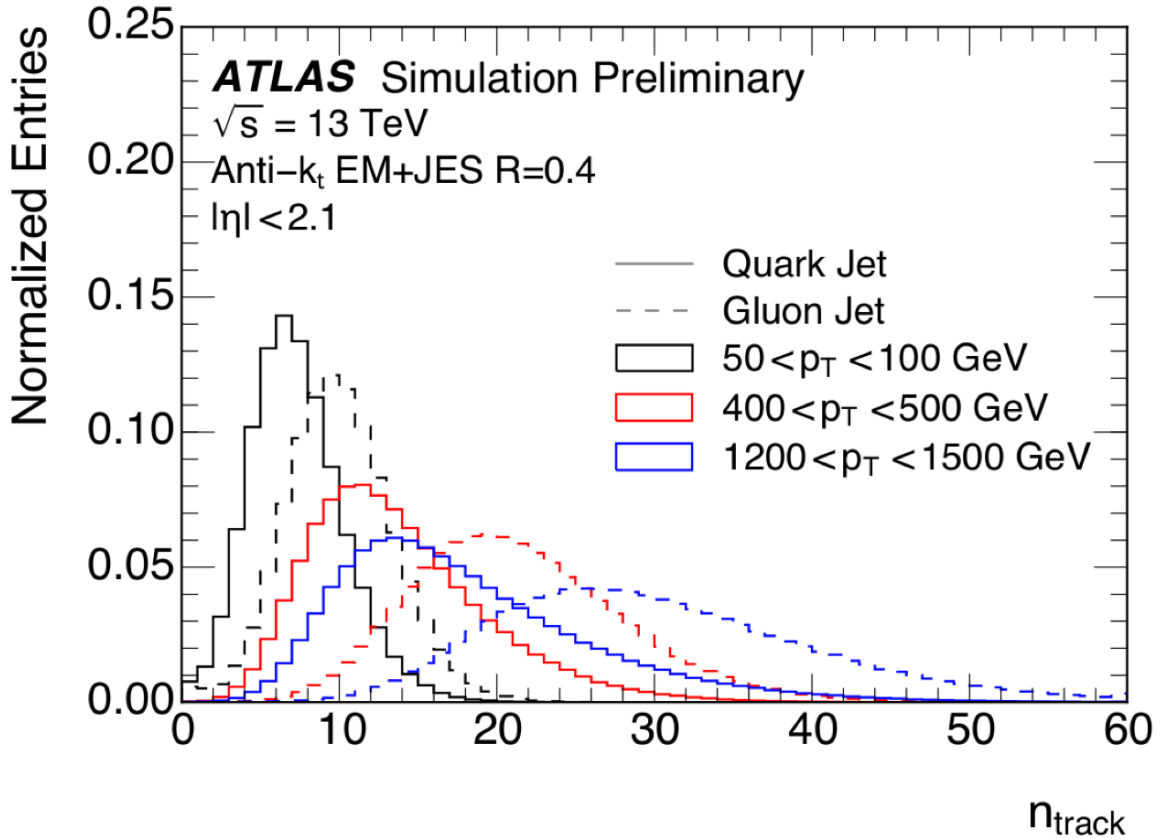


Figure 4.7: Distribution of the reconstructed number of tracks in a jet across different  $p_T$  bins and with the Pythia8 A14 generator tune results input into GEANT4. Jets must satisfy  $|\eta| < 2.1$  and tracks pass if  $p_T > 500 \text{ MeV}$  along with quality criteria described in [57]. Figure from [57].

In Ref. [57]  $q/g$  tagging studies used a working point of 60%, i.e. required each  $p_T$  bin to have 60% quark-initiated jet purity. For the steeply-falling dijet mass spectrum this selection would result in discontinuities leading to challenges with a resonance search. Instead several different selections were investigated, and a selection criteria that is linear in  $\ln(p_T)$  was found to result in a smooth mass distribution. It can also be chosen to produce a selection efficiency that is approximately uniform.

The tagger classifies a jet as more likely to be either quark- or gluon-initiated if  $n_{\text{track}}$  is less than the threshold  $n_q$  and more likely to be gluon-initiated if  $n_{\text{track}}$  is greater than the threshold  $n_g$ . The actual efficiency of any given  $n_{\text{track}}$  cut is determined using truth information in MC samples.

$$\begin{aligned} n_{\text{track}} \leq n_q & : \text{quark-initiated jet} \\ n_{\text{track}} \geq n_g & : \text{gluon-initiated jet} \end{aligned} \tag{4.4}$$

Where

$$n_{q(g)} = c_{q(g)} + m_{q(g)} \ln(p_T) \tag{4.5}$$

The constants  $m_{q(g)}$  and  $c_{q(g)}$  are chosen to provide suitable sub-samples, and  $p_T$  in units of GeV. The values of  $m$  and  $c$  are chosen by finding the value of  $n_{\text{track}}$  that correspond to the desired working point efficiency for truth quark and gluon jets, then fitting the results. For each  $p_T$  bin the value of  $n_{\text{track}}$  closest to the chosen selection efficiency is found. But this is an integer number of tracks and does not correspond exactly to the selection efficiency. It is therefore necessary to apply a correction to, done by estimating the fractional number of tracks that corresponds to the efficiency. So where an efficiency of 80% is desired and the nearest integer values of  $n_{\text{track}}$  give efficiencies of 79.6% and 80.2%, a linear interpolation is carried out between the efficiencies for the selected bin and its nearest neighbour to find the fractional  $n_{\text{track}}$  that gives exactly 80%. The uncertainty on this value is estimated using binomial uncertainties.

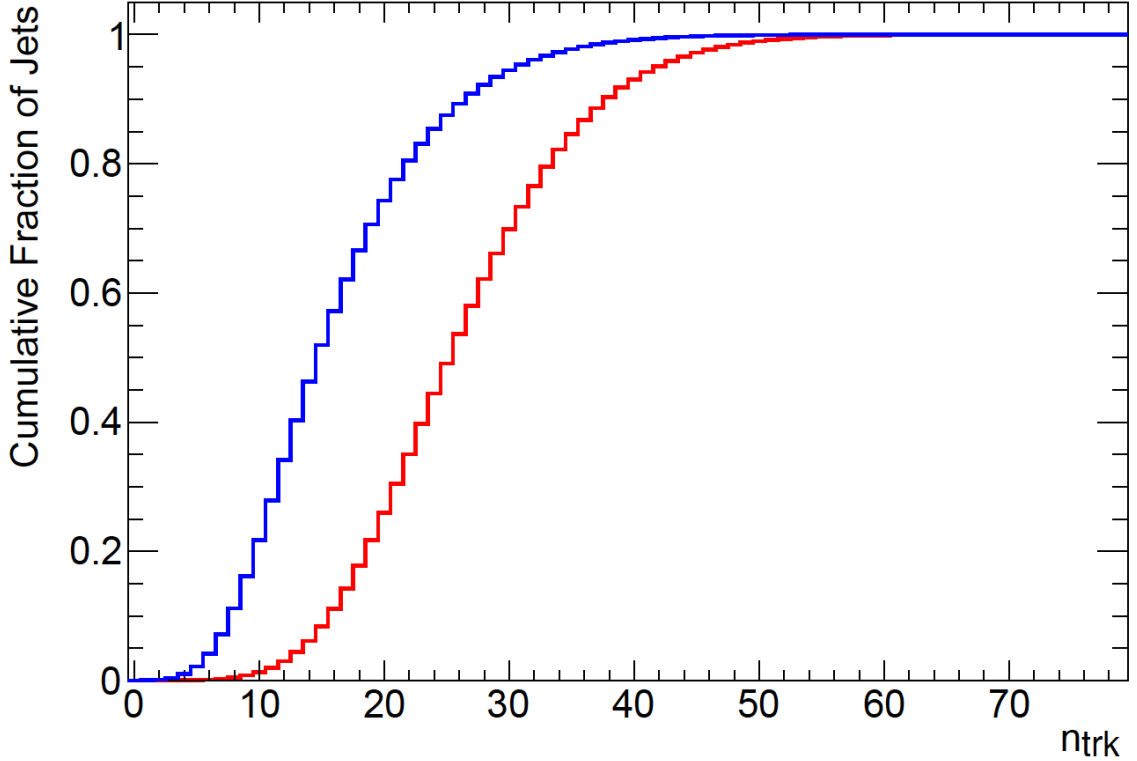
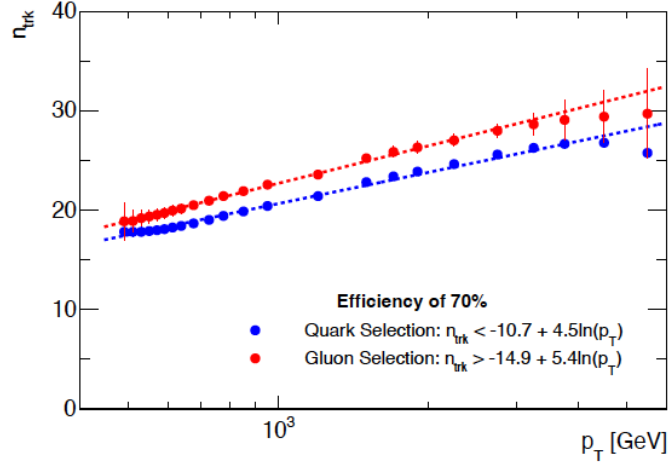


Figure 4.8: The cumulative distribution of  $n_{\text{track}}$  for truth quark (blue) and gluon (red) initiated jets satisfying  $800 < p_T < 900$  GeV.

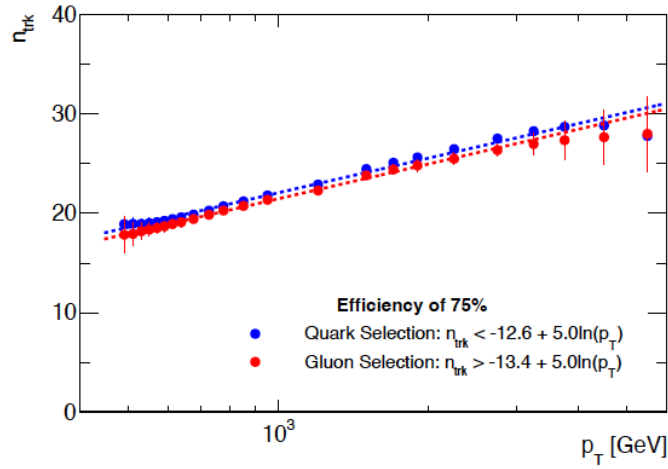
To complete the procedure described above,  $n_{\text{track}}$  must be binned in  $p_T$ . Bin edges are chosen to be 480, 500, 520, 540, 560, 580, 600, 625, 650, 700, 750, 800, 900, 1000, 1400, 1600, 2000, 2500, 3000, 3500, 4000, 5000 and 6000 GeV. An example of the cumulative  $n_{\text{track}}$  distributions for truth quark and gluon jets with  $800 < p_T < 900$  GeV is shown in Figure 4.8.

The actual values of the constants  $c_{q(g)}$  and  $m_{q(g)}$  for this analysis were found for both quark and gluon selection efficiencies between 65% and 95%, in steps of 5%. The value of  $n_{\text{track}}$  found to best satisfy the 70%, 75% and 80% selection efficiencies are shown in Figure 4.9 and the values of the constants are shown in Tables 4.3 and 4.4.

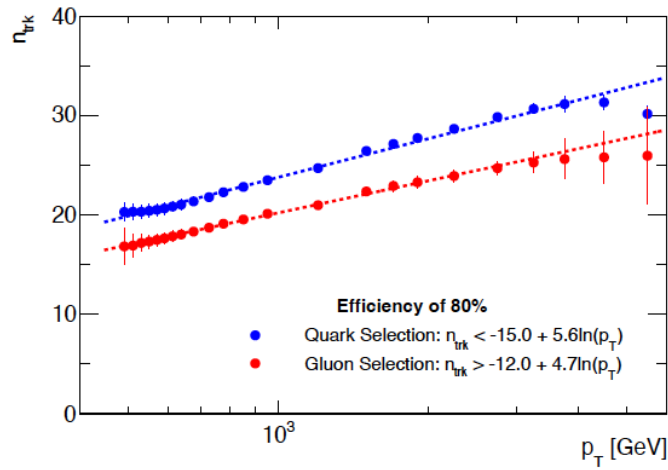
Above 4000 GeV the value of  $n_{\text{track}}$  that satisfies the selection efficiency plateaus. This could indicate a saturation effect, and as a cross-check the data is fitted with an alternative function:



(a)



(b)



(c)

Figure 4.9: The values of  $n_{\text{track}}$  for (a) 70%, (b) 75% and (c) 80% quark (blue) and gluon (red) selection efficiencies in every  $p_T$  bin, along with the best fit to Equation 4.5 [94].

Truth- $g$ selection efficiency	Truth- $q$ selection efficiency	$c_q$	$m_q$
0.95	0.732	-27.568	8.789
0.9	0.563	-21.518	7.269
0.85	0.447	-17.646	6.304
0.8	0.350	-14.956	5.610
0.75	0.278	-12.600	5.022
0.7	0.221	-10.691	4.536
0.65	0.174	-8.990	4.105

Table 4.3: Values of the constants  $m_q$  and  $c_q$  from Equation 4.5 such that  $n_{\text{track}} \leq n_g$  for truth gluon jets with efficiencies ranging from 65 to 95%.

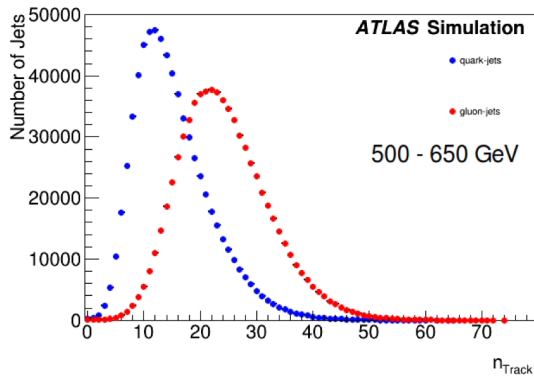
Truth- $q$ selection efficiency	Truth- $g$ selection efficiency	$c_q$	$m_q$
0.95	0.586	-7.541	3.233
0.9	0.456	-8.980	3.779
0.85	0.377	-10.419	4.230
0.8	0.320	-11.964	4.659
0.75	0.274	-13.376	5.047
0.7	0.234	-14.937	5.446
0.65	0.201	-16.466	5.834

Table 4.4: Values of the constants  $m$  and  $c$  from Equation 4.5 such that  $n_{\text{track}} \geq n_q$  for truth quark jets with efficiencies ranging from 65 to 95%.

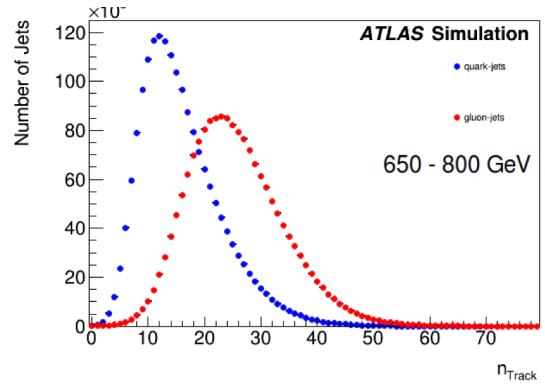
$$n_{q(c)} = c + m \ln(p_T) + n \sqrt{\ln(p_T)} \quad (4.6)$$

When the values of  $m$  and  $c$  resulting from fitting Equation 4.6 to the distribution of  $n_{\text{track}}$  are used and Figure 4.8 is reproduced with the new selection criteria, there is shown to be negligible difference. The simpler choice is then to use Equation 4.5.

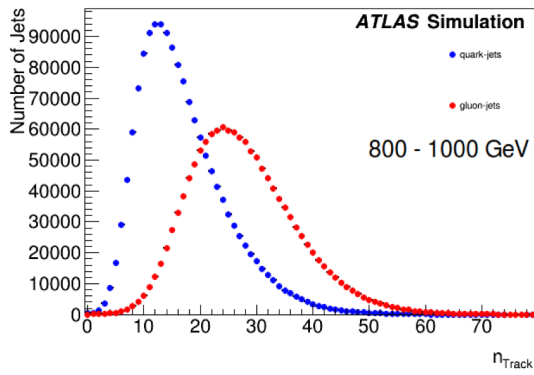
The extent to which the tagger can discriminate between signal and background QCD events is dependent on the differences between track multiplicity distributions of quark- and gluon-jets. Examples of these are shown in Figure 4.10, and for background events simulated with Pythia across different  $p_T$  ranges. Figure 4.12 shows examples of these distributions for the excited quark signal modelled using the same generator. These plots show the same trend from Figure 4.7, i.e. that separation between mean track multiplicity increases at high  $p_T$ . Also illustrated is the decline in gluon jets at high  $p_T$ , which is not evident in the excited quark sample since the decay process leads to the same final state at all the simulated mass points. This observation is however dependent on the accuracy of the model. Through this, one can observe a higher proportion of gluon jets in the enriched signal sample than in background, and therefore see the power of quark-gluon tagging. This is especially true of gluon-initiated jets with heavy final state processes at high mass.



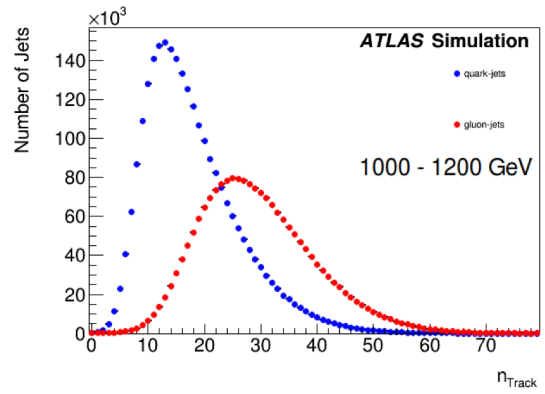
(a)



(b)



(c)



(d)

Figure 4.10: Examples of the Pythia8 Truth  $n_{track}$  distributions between 500 and 800 GeV. The quark jets shown in blue have fewer tracks than the gluon jets in red, with the separation increasing at higher  $p_T$ . Quark jets are far more numerous at high  $p_T$

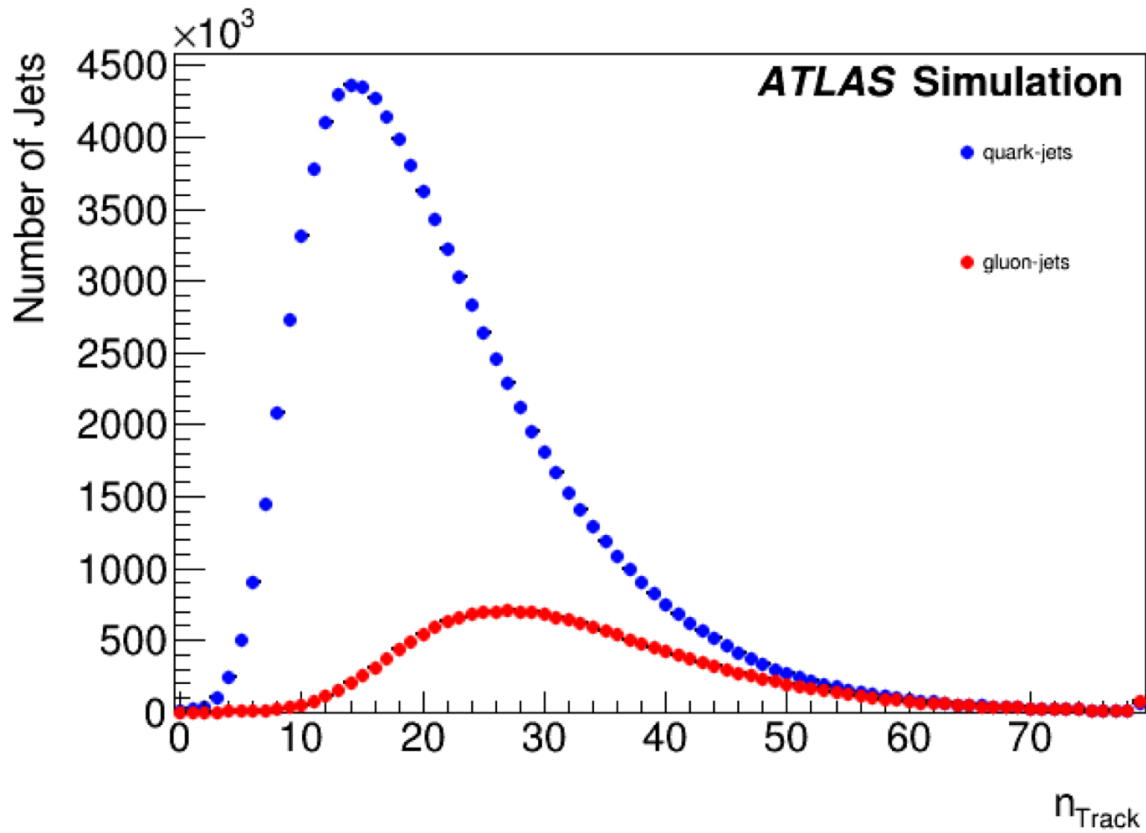


Figure 4.11: Pythia8 Truth  $n_{track}$  distributions across all  $p_T$  bins. The difference in the distributions of quark and gluon jets shows how it can act as an excellent discriminator.

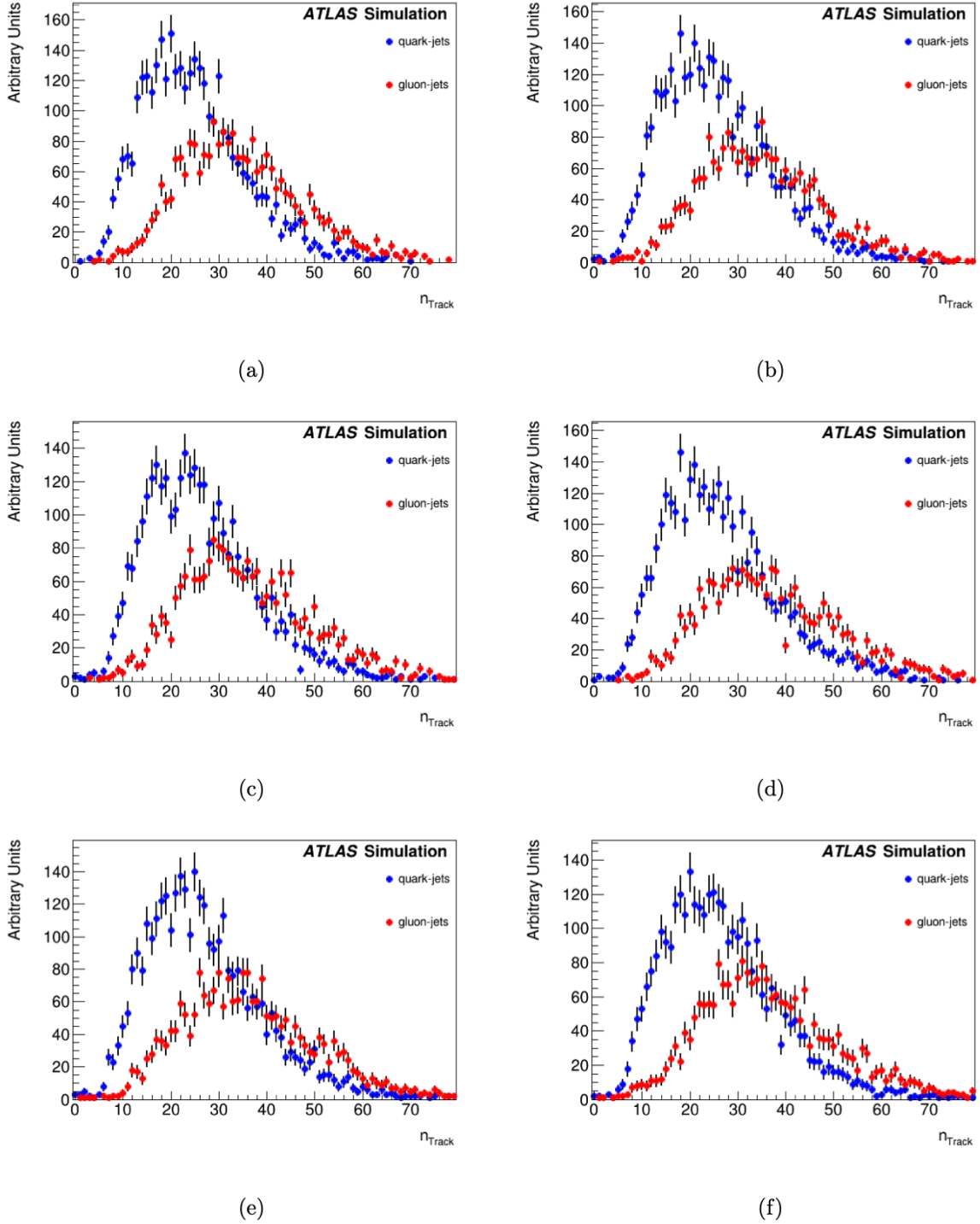


Figure 4.12: Pythia8 Truth  $n_{track}$  distributions between 4500 and 7000 GeV for excited quark samples. At high  $p_T$  the number of quark and gluon jets is roughly equal [94].

## 4.4 Systematic Uncertainties

The most significant systematic uncertainties for the quark-gluon tagger come from modelling and from track reconstruction. These have been studied previously at low  $p_T$  [57] and are a significant contribution to overall uncertainties. While the existing approach, which is data-reliant, provides good estimates of uncertainty in the 200 – 800 GeV mass range, at the edges there are issues which are described in detail below.

### 4.4.1 Existing Approach

The existing approach to deriving these uncertainties relies on a combination of simulation and data. It is based on the following system of equations:

$$\langle n_{\text{charged}}^f \rangle = f_q^f \langle n_{\text{charged}}^q \rangle + f_g^f \langle n_{\text{charged}}^g \rangle \quad (4.7)$$

$$\langle n_{\text{charged}}^c \rangle = f_q^c \langle n_{\text{charged}}^q \rangle + f_g^c \langle n_{\text{charged}}^g \rangle \quad (4.8)$$

where for the two highest  $p_T$  jets within a dijet event, the fraction labeled as quark jets in simulation is  $f_q^{f/c}$  and the fraction labeled as gluons jets is  $f_g^{f/c}$ . The superscript  $f$  denotes the jet with higher  $\eta$  (forward jet) and  $c$  labels the more central jet. The fractions are calculated using parton distribution functions convoluted with matrix element calculations.

At low  $p_T$  (up to  $\sim 250$  GeV) events are dominated by  $pp \rightarrow gg$ , becoming mostly  $pp \rightarrow qq$  at high  $p_T$  ( $\sim 2000$  GeV). In the intermediate  $p_T$  regions there is a mix of final states,  $gg$ ,  $qg$  and  $qq$  [57]. To demonstrate that Eq. 4.7 holds, it must be shown that obtaining  $n_{\text{charged}}^{q,g}$  from Equation 4.7 or directly from labeled jets gives equivalent results. It can be demonstrated that this holds to within less than 1% across almost the entirety of the  $p_T$  range (up to 1500 GeV - see [57]), thus demonstrating that to an excellent approximation, the charged particle multiplicity inside jets depends

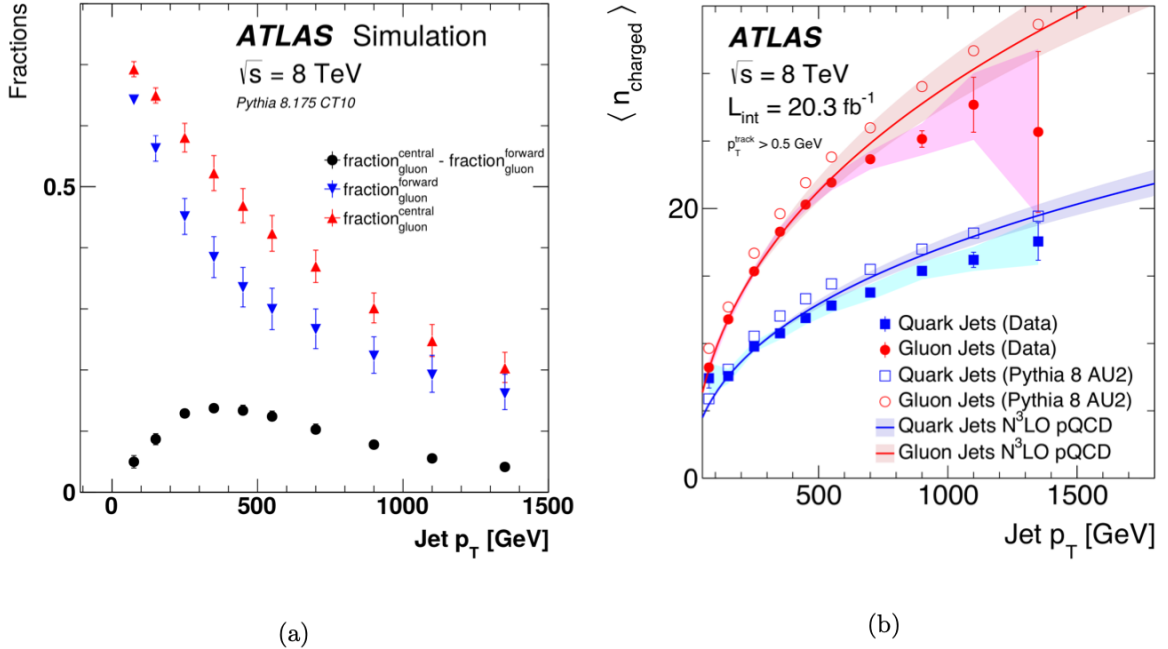


Figure 4.13: In (a), the simulated fraction of jets originating from gluons as a function of jet  $p_T$  for the more forward jet (down triangle), the more central jet (up triangle), and the difference between these two fractions (circle). The error bars represent PDF and ME uncertainties. In (b), the jet  $p_T$  dependence of the average charged-particle multiplicity of quark- and gluon-initiated jets. The error bands include the experimental uncertainties, as well as PDF and ME uncertainties. The MC statistical uncertainties are smaller than the markers. The uncertainty band for the N<sup>3</sup>LO pQCD prediction is determined by varying the scale  $\mu$  by a factor of two up and down. Both (a) and (b) use Pythia with the CT10 PDF. From [98].

only on  $p_T$  and initiating parton type. This particle level analysis provides a detector independent set of uncertainties, which are then connected to track multiplicity with a set of detector-related uncertainties.

Tagging uncertainties can be calibrated using the approach in Ref. [98] to allow  $\langle n_{\text{charged}} \rangle$  to be measured as a function of  $p_T$  and to extract  $\langle n_{\text{charged}}^{q,g} \rangle$  by exploiting the rapidity dependence of the  $q/g$  jet fraction. The result of applying this to unfolded data is shown in Figure 4.13.

The nominal fractions  $f_{q,g}^{f,c}$  are calculated from Pythia8 [99] using the CT10[100] PDF set. In addition to experimental and statistical uncertainties included in Figure 4.13(b), eigenvector variations in the CT10 PDF set give an estimate of PDF un-

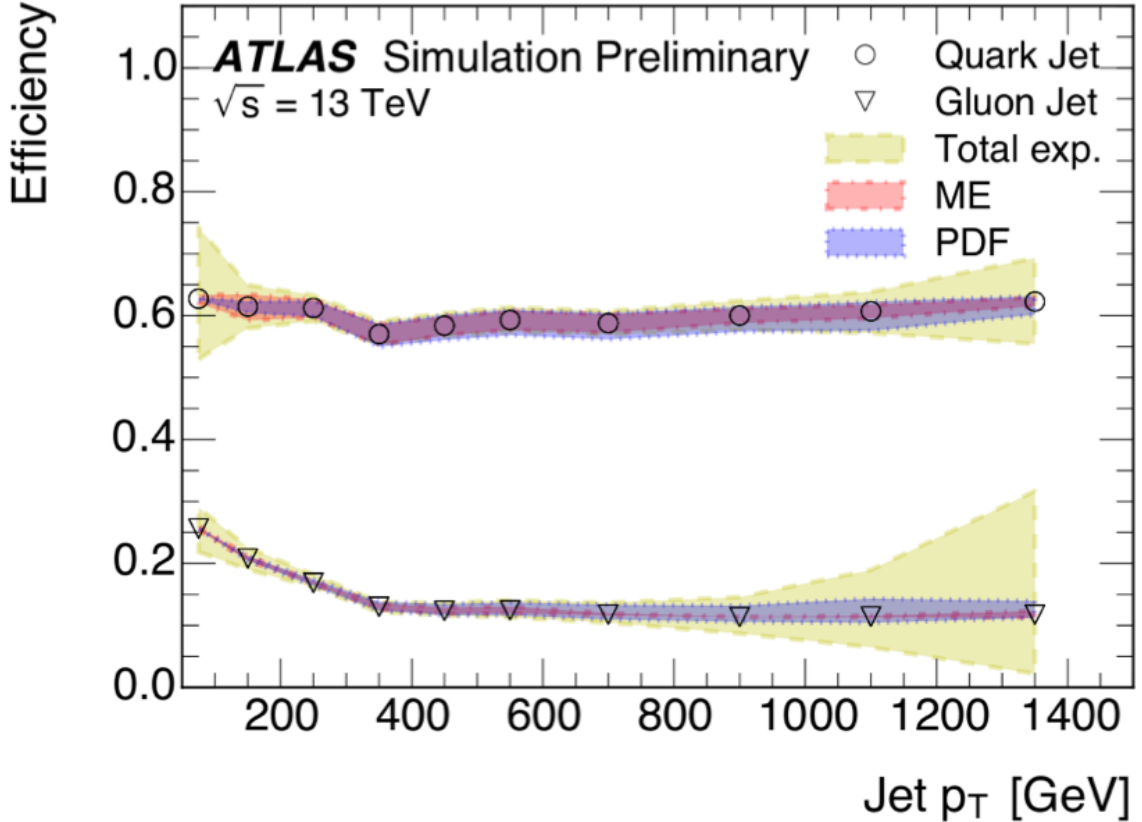


Figure 4.14: The systematic uncertainties on the particle-level charged particle distribution for a 60% quark jet efficiency working point, from [57].

certainty, and uncertainty in the  $q/g$  fraction from the matrix element calculation is estimated using the variation between Pythia and Herwig [101]. The Pythia8 results are reweighted to the PDF set in Herwig++, CTEQ6L1 [102], using the LHAPDF [103] library. Uncertainty bands are obtained by summing all these uncertainties in quadrature. The impact is shown for a 60% quark jet efficiency in Figure 4.14.

Other variations were also studied in [57] to ensure the uncertainties are reasonable. The Pythia8 sample was re-weighted to the NNPDF2.3 set to confirm these unrelated PDF sets produce similar uncertainties to the CT10 variation. The total ranged from  $\sim 0.1$  to 1 charged particles at both low and high  $p_T$  and for both checks, which is good agreement. Other negligible uncertainties are also discussed in [57].

The dijet analysis uses the A14 tune for event generators, which gives good agreement with data for  $n_{\text{track}}$  inside jets of up to  $p_T \sim 1600$  GeV. The comparison between

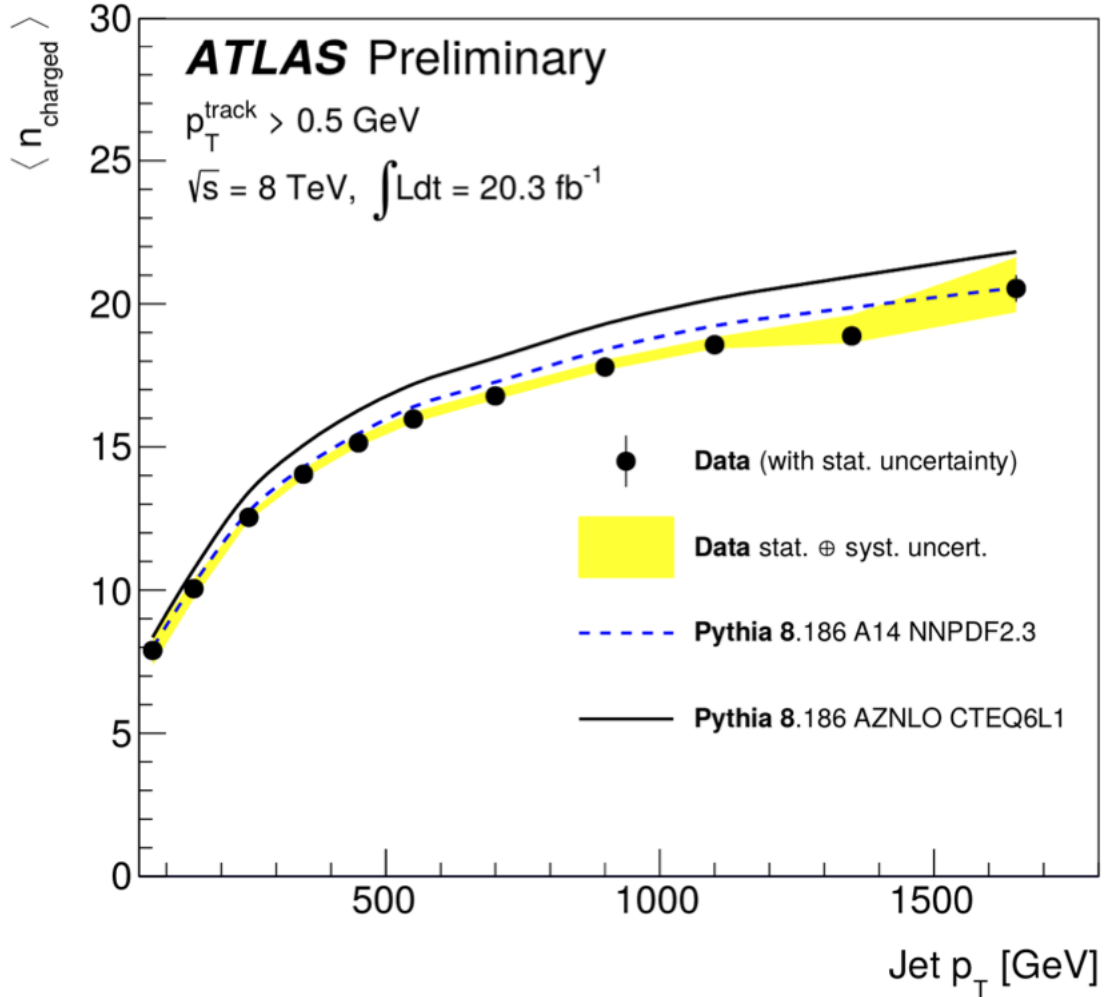


Figure 4.15: A comparison of charged particle multiplicity for the most forward jet in a dijet pair, from data, Pythia8 with the A14 tune and Pythia8 with the AZNLO tune from [57]. Data and uncertainties are from [98] via HEPData [105].

the A14 tune, data and a tune used in Higgs analyses (AZNLO [104], which overestimates  $n_{\text{track}}$ ) is shown in Figure 4.15. A factorised approach is presented in [57] which validates the use of the same procedure for any tune.

A further consideration in assessing modeling uncertainties is the topological dependence of the tagging procedure, an unavoidable issue since both quarks and gluons carry colour charge while hadrons do not. Previous studies have found this dependence to be small in  $n_{\text{track}}$ -based taggers [106].

The detector independent uncertainties are associated with some issues. At high

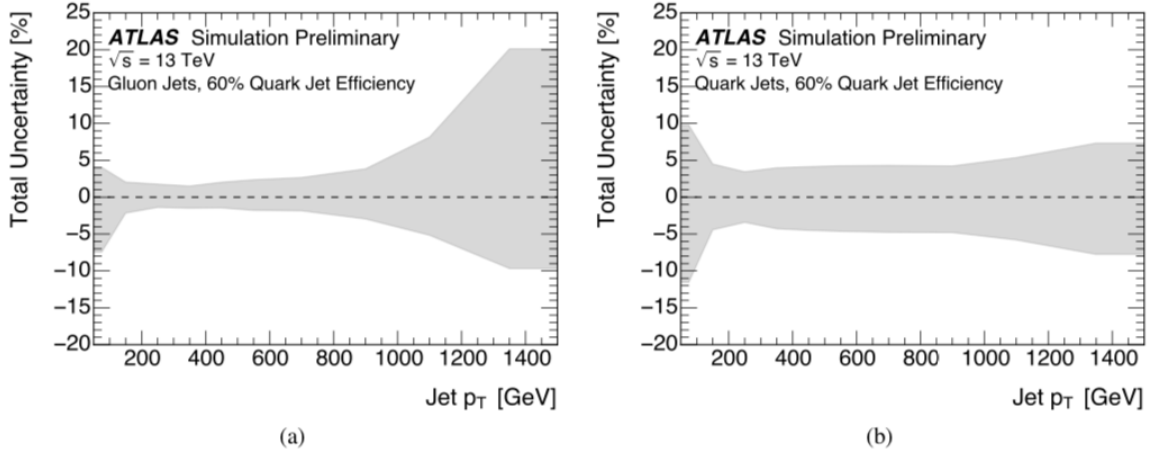


Figure 4.16: The total systematic uncertainty for the 60% quark jet efficiency working point of the quark/gluon tagger for (a) quark jets and (b) gluon jets. From [57].

and low  $p_T$  they become significantly larger than at the centre of the  $p_T$  regime, as shown in Figure 4.16.

This is because at high  $p_T$  the tagger is limited by the sample size, with insufficient gluon jets being produced. The lack of data leads to the significant increases in the uncertainty seen at the edges of the  $p_T$  range in Figure 4.16. The tracking performance itself is also complicated at high  $p_T$  because the hit density inside jets increases, and the separation between tracks becomes of the same order as the detector resolution. Hit density inside jets increases and the combinatorics involved in modelling this becomes more complicated. But the tagger depends on good track resolution for an accurate value of  $n_{\text{track}}$ . These factors also contribute to the increasing values of uncertainties given by this method.

#### 4.4.2 Pure MC-based Uncertainties

The detector-independent nature of these studied quantities offers an opportunity for improvement. A new approach based purely on MC is possible. While this does not offer improvement where sufficient data is available, it may be preferable at high and low  $p_T$ , though still not low.  $n_{\text{track}}$  depends only on  $p_T$  and the initiating parton type, so the approach taken was to plot histograms of  $n_{\text{track}}$  in bins of jet  $p_T$ . Comparing

Comparison	Uncertainty
SherpaCSS vs SherpaLund	Hadronization Uncertainty
SherpaCSS vs Pythia	PDF Uncertainty
H7Angular vs H7Dipole	Parton Shower Uncertainty

Table 4.5: Dataset comparisons and uncertainties drawn from each.

histograms of  $n_{\text{track}}$  in bins of jet  $p_T$ , generated from different simulation models, will give an uncertainty for the tagger. The simulations chosen for the comparison each model one specific process differently, with Pythia chosen as the nominal for its demonstrated similarity to data distributions.

While there are several possible variations of this plot that could be useful, the one most relevant to the q/g tagged dijet analysis is finding the cut that gives a certain gluon efficiency for each generator, applying this cut to other generators and comparing the resulting gluon efficiency. Also possible is for example calculating the 50% gluon efficiency cut in Pythia then examining the quark efficiencies this working point gives in a different model, or recalculating the cut for each generator, with each perhaps suiting a different type of analysis. To make these plots, the first step is producing ROC (efficiency) curves. These are plots of quark efficiency vs gluon efficiency, where the number of quarks misidentified by the tagger as gluons is the quark efficiency, produced separately for each  $p_T$  bin, and the number of gluons correctly identified is the gluon efficiency. An example of these plots (for the case of SherpaCSS) is shown in Figure 4.17. From these plots the  $n_{\text{track}}$  cut for any given working point can be found, along with the corresponding quark efficiency for the chosen gluon efficiency.

The uncertainty itself is given by the difference between any two given pairs of generators. An example of such a comparison plot, for Pythia, SherpaCSS and SherpaLund, is shown in Figure 4.18.

The uncertainties resulting from this method are not small (still  $> 10\%$ ), however

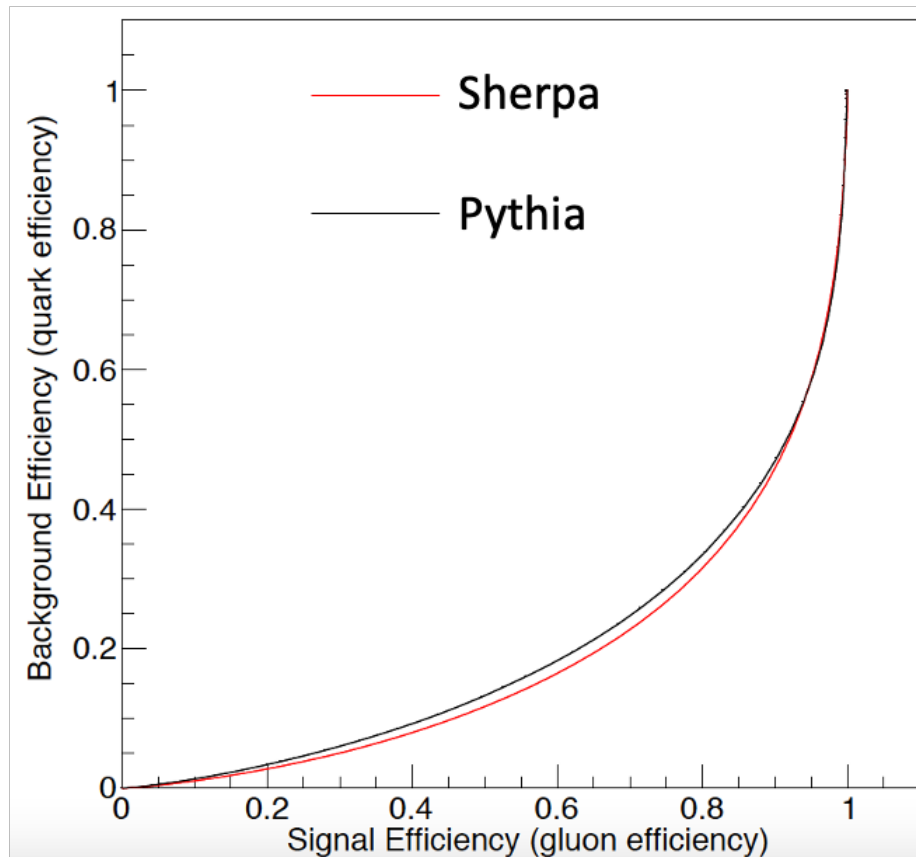


Figure 4.17: Quark Efficiency vs Gluon Efficiency for SherpaCSS. The number of quarks misidentified by the tagger as gluons is the quark efficiency, produced separately for each  $p_T$  bin, and the number of gluons correctly identified is the gluon efficiency.

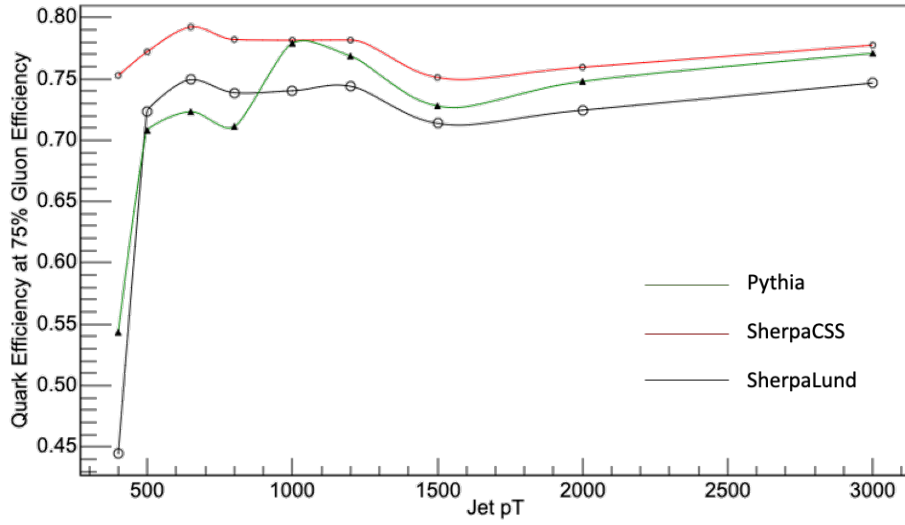


Figure 4.18: Plots are made by calculating the cut that gives a certain gluon efficiency for each generator, applying this cut to other generators and comparing the resulting gluon efficiency to the original. The hadronization uncertainty is given by the difference between SherpaCSS and SherpaLund, while a comparison of Pythia and SherpaCSS gives the PDF uncertainty.

as expected they are smaller than those from the existing method particularly at high  $p_T$ .

### 4.4.3 Track Uncertainties

Four variations are applied according to ATLAS recommendations. They are labelled as follows:

---

Comparison	Uncertainty
Tracking1	Track reconstruction efficiency
Tracking2	Fake Rate, a relative 25% uncertainty on the rate of reconstructing fake tracks passing the Loose track selection
Tracking3	Weak modes in the alignment
Tracking4	Combines a few systematics. If the track is outside a cone of $dR = 0.1$ with the jet, the track is not removed. If, however, the track is within this distance, there are a few systematic uncertainties associated with TIDE efficiency and fake rate which give separate probabilities for the track to be dropped.

---

Table 4.6: The four tracking uncertainties and the systematic associated with each.

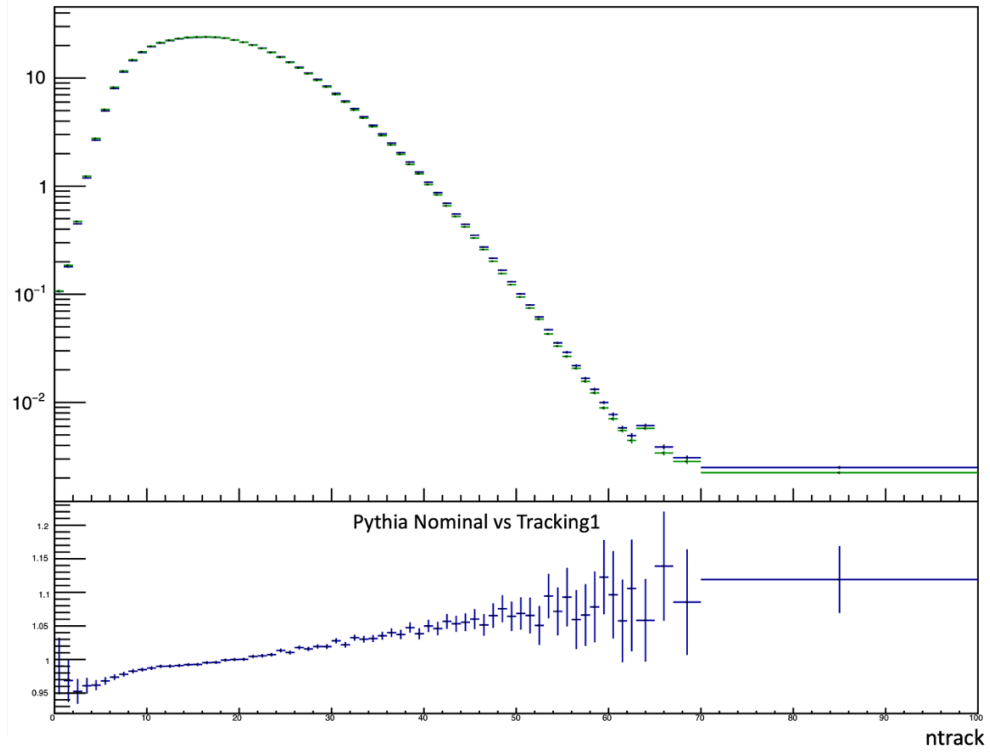
The precise origins of these uncertainties are discussed in greater detail in Section 4.4.4. Figures 4.19 and 4.20 show the above systematics compared to the nominal Pythia.

As expected these differences are very small.

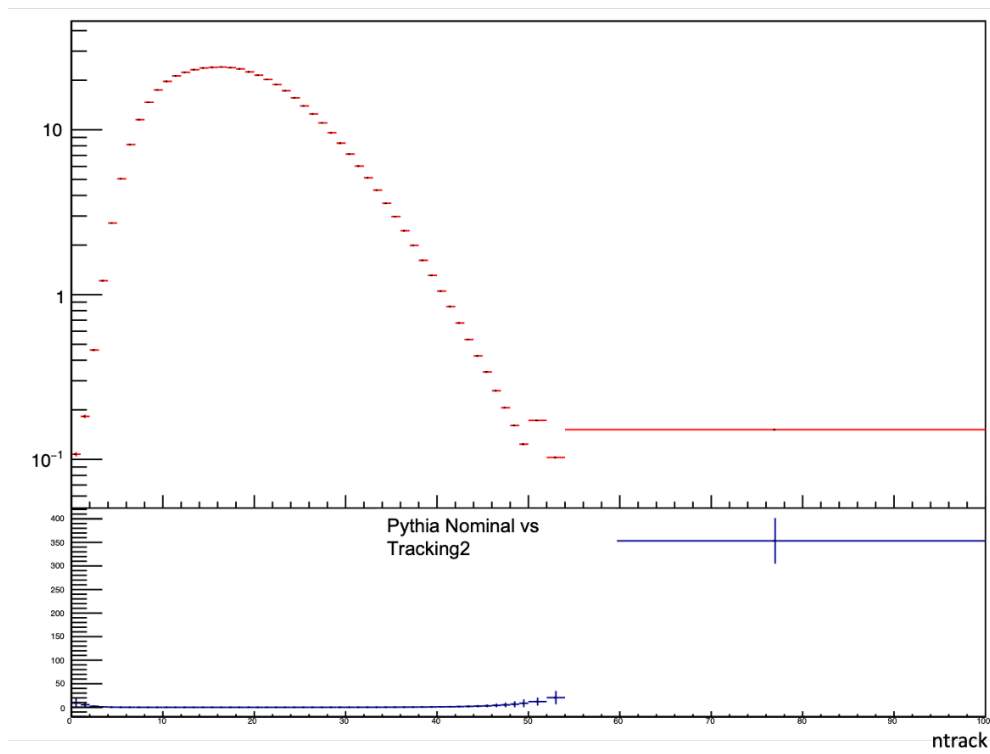
### 4.4.4 Experimental Uncertainties

Detector-specific uncertainties must also be taken into account when relating charged particle multiplicity to the observed track multiplicity. The three categories that arise are:

- Reconstruction efficiency
- Track fit parameter bias and resolution
- Fake rate

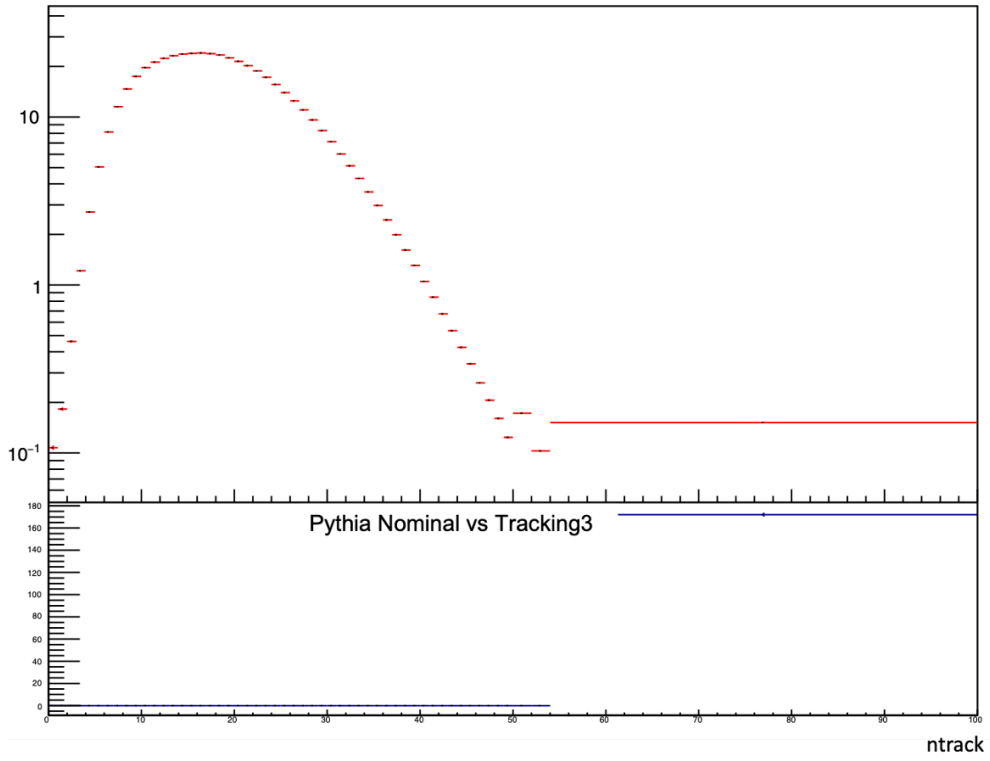


(a)

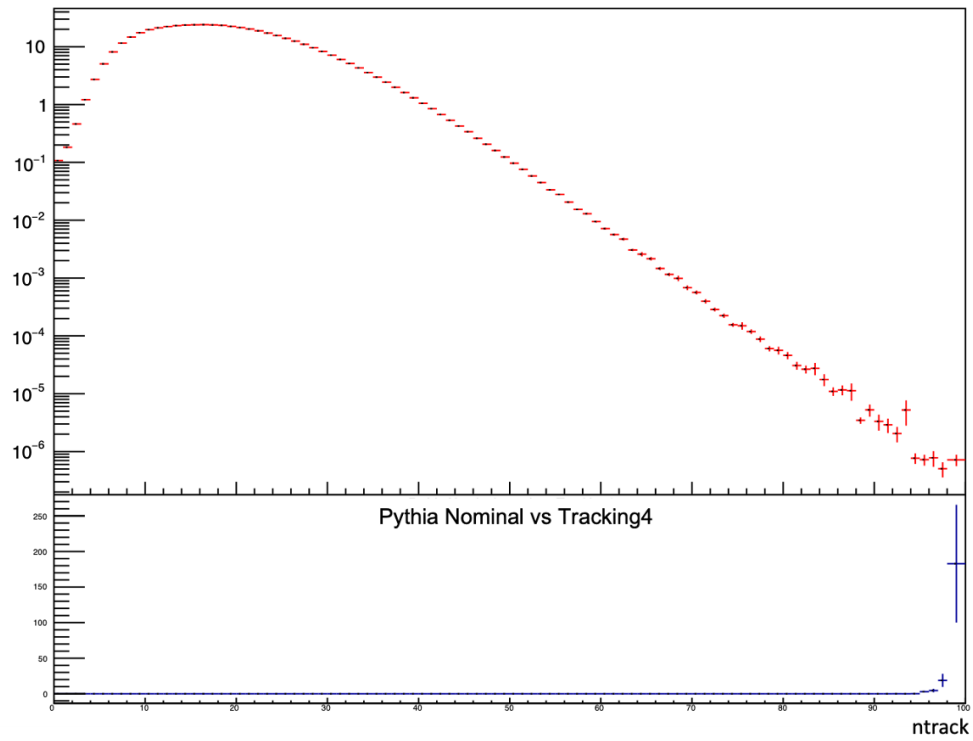


(b)

Figure 4.19: (a) Track reco efficiency variation vs nominal (b) Fake rate variation vs nominal



(a)



(b)

Figure 4.20: (c) Weak modes variation vs nominal (d) Remaining systematic variations vs nominal (vary cone acceptance, TIDE efficiency)

The uncertainty due to reconstruction efficiency comes from imperfect descriptions of the ID material in simulation, and from tracks lost in volumes with high particle density. The uncertainty arising from incorrect modelling of particle interactions with the inner detector is measured by varying the GEANT4 physics list [107]. Tracks are also lost in the core of jets, where clusters in the ID can merge. The fraction of tracks lost is measured by looking at one-track clusters in jets whose deposited charge is consistent with a minimum of two ionising particles [108]. This is the largest uncertainty and is typically within 5%.

The track fit parameter scale and uncertainties in the resolution are largely negligible when it comes to  $n_{\text{track}}$ , less than 1%. A small uncertainty on track  $p_T$  is present from a potential sagitta bias from weak modes. Deformations of the sagitta are orthogonal movements of the detector (relative to the track trajectory). These have the opposite effect on the reconstructed curvature of tracks for positive and negative particles [109]. Weak modes in detector alignment are detector deformations that preserve a helical trajectory in tracks and so don't affect the  $\chi^2$  of the track fit. These arise because the ID is aligned using a track-based technique [110], and are the main source of systematic effects in the weak modes.

Fake tracks are particle trajectories that cannot be associated to a single particle. The rate of fake tracks increases with pile-up because of the correspondingly higher hit rate in the ID. The fake rate has been studied for various track selections [107] and can be mitigated by the use of appropriate quality criteria.

The impact of experimental uncertainties on tagging efficiency is summarised in Figure 4.21. A set of quality criteria [57] are used to reject fake and badly measured tracks along with the cut  $p_T > 0.5$  GeV.

The total modelling and experimental uncertainties, when considered uncorrelated and summed in quadrature, provide the total uncertainty previously shown in Figure 4.16 for the same 60% working point, chosen as it showed the greatest potential for improvements in significance when setting cross-section limits.

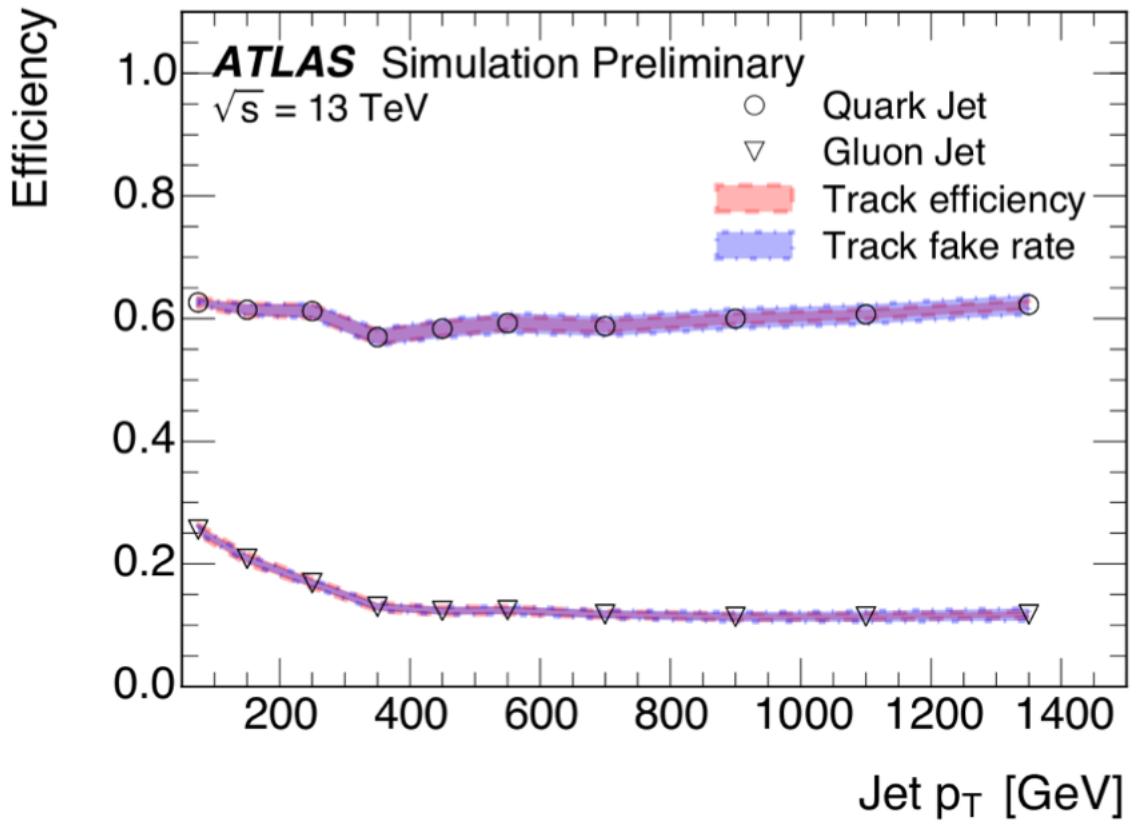


Figure 4.21: Systematics from experimental (detector-dependent) uncertainties on track reconstruction for a 60% quark jet efficiency of the tagger, from [57].

# Chapter 5

## Fitting Framework

### 5.1 xmlAnaWSBuilder

Previous searches for dijet resonances by the ATLAS collaboration have made use of the Sliding Window Fits (SWiFt) method (see e.g. [111]). It is now based on the xmlAnaWSBuilder (xAW) [112], widely used in the Higgs group and developed by them for their specific use case, with adaptations to accommodate the steeply-falling dijet mass spectrum.

xAW creates RooFit [113] workspaces based on one-dimensional observables. The workflow is summarised in Figure 5.1.

The dijet mass spectrum is fitted using a binned maximum likelihood fit, run with a modified QuickFit [115] framework that allows integration over binned data. QuickFit is built on RooFit and RooStats [116]. The modification is required due to the steeply-falling nature of the dijet mass spectrum, which presents unique challenges. Previous versions of RooFit evaluate fit functions at the centre of each bin, rather than at the center of gravity (for example, the average mass in each bin). In cases such as this analysis, this leads to significant biases in the fit results [117]. However recent developments in RooFit have created a new class, `RooBinSamplingPdf`, which resolves this issue. It is available in the Root v6.24 release and later.

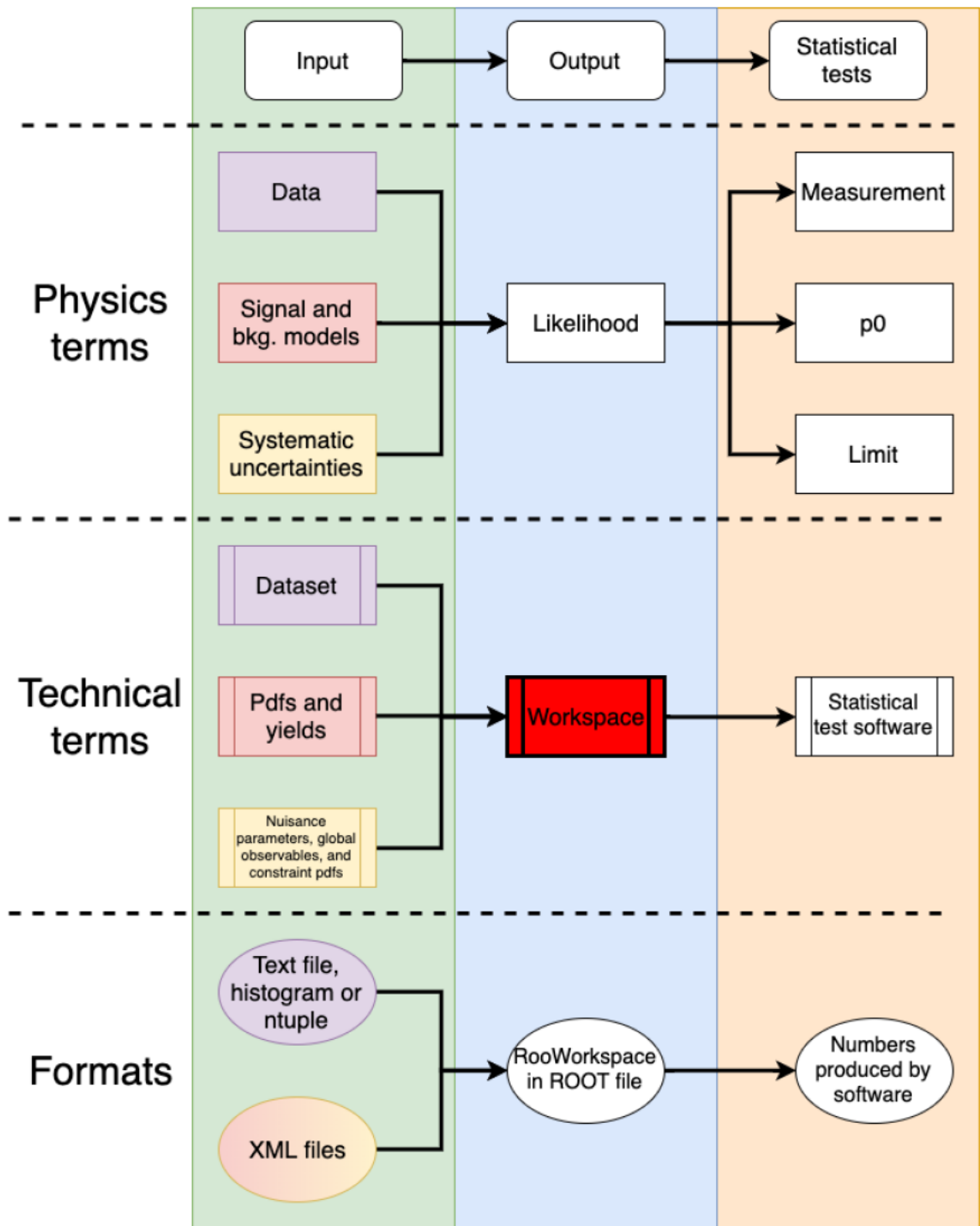


Figure 5.1: The workflow in the xmlAnaWSBuilder. The terms widely used in discussions is listed in 'Physics terms' with the specific inputs the code needs for these listed under 'Technical terms'. The file formats required as inputs and given as outputs are shown in the 'Formats' section [114].

## 5.2 Statistical Method

### 5.2.1 Limit Setting

Interaction cross section limits for simulated signal models are the key indicator by which the effect of q/g tagging is quantified. In particular, model-independent limit setting gives sensitivity to any signals that may be accessible to this analysis despite lack of current theoretical motivation, and also allows comparisons of the strength of different analyses. Hypothesis tests are performed based on a frequentist method, and the profile likelihood ratio  $\lambda_\mu$  is used to define a test statistic,  $q_{\mu_{sig}}$ :

$$q_{\mu_{sig}} = -2 \ln \lambda(\mu_{sig}) \quad (5.1)$$

For  $\lambda_\mu$  defined as a function of nuisance parameters  $\theta$ :

$$\lambda_{\mu_{sig}} = \frac{L(\mu_{sig}, \hat{\theta})}{L(\hat{\mu}_{sig}, \hat{\theta})} \quad (5.2)$$

where  $\hat{\mu}_{sig}$  and  $\hat{\theta}$  maximise the likelihood function and  $\hat{\hat{\theta}}$  maximises the likelihood,  $L$ , of a specific fixed value of signal strength  $\mu_{sig}$ . The likelihood function is the product of Poisson probabilities across all  $i$  bins,

$$L(\mu_{sig}, \theta) = \prod_{i=1}^N \frac{(\mu_{sig} s_i + b_i)^{n_i}}{n_i!} \exp(-(\mu_{sig} s_i + b_i)) \quad (5.3)$$

The parameter of interest (POI)  $\mu$  is the signal strength, with  $\mu = 0$  corresponding to the background only hypothesis and  $\mu = 1$  corresponding to the nominal signal hypothesis.

The  $CL_s$  method is used to test the exclusion of BSM physics models [108], [109]. The method defines a Confidence Level, denoted as  $CL_s$ , which is the ratio of the p-value for the null hypothesis ( $p_0$ ) to the p-value for the alternative hypothesis ( $p_1$ ). In this case it quantifies how well the data is consistent with the null hypothesis (Standard Model). To speed up the computational evaluation approximations to the asymptotic formulae are used [110].

The Run I dijet analyses used a Bayesian approach to limit setting (see e.g. [118]). Since Run II however, frequentist methods have been adopted by the analysis community. They have several advantages: faster convergence of calculations and the existence of equations to predict the distributions of posterior quantiles [110]. The interpretations of upper limits are slightly different in the Frequentist case compared to the Bayesian case. In the Bayesian case, an upper limit on signal strength is the cross-section above which there is 95% certainty that no new physics processes are occurring. In the Frequentist approach, the upper limit is the upper edge of a 95% CL interval with the lower edge set at  $-\infty$ . Frequentist statistics also remove an element of the subjectivity introduced by a Bayesian prior probability distribution. Thus it suffers from possible misinterpretation of results: conclusions are drawn about the compatibility of data and theory, but tend to be misinterpreted as a statement about the theory given the data [109]. Large statistics and small background tend to lead to convergence in both approaches.

Feldman and Cousins [119] suggest an approach based on frequentist confidence intervals, which have the drawback of sometimes leading to unintuitive results. An illustrative example would be the case of two searches with identical efficiencies but different backgrounds. The largest expected background would then lead to the strongest limit. But there is a widely accepted solution to these problems, via a generalisation of Zech’s classical derivation [120] of upper limits for single channel counting experiments. It involves normalising the confidence level for the signal+background hypothesis to that of the background-only hypothesis ( $\mu_{sig} = 0$ ). This approach enables sensible exclusion limits even with a small number of observed events which may lead to doubt in the background hypothesis. It is often referred to as the ‘modified frequentist’ approach. The resulting calculation to be performed is:

$$CL_s \equiv \frac{CL_{s+b}}{CL_b} \tag{5.4}$$

For the signal + background hypothesis  $CL_{s+b}$  and the background only hypoth-

esis  $CL_b$ , used to define a ratio of confidences  $CL_s$ . The signal hypothesis can be considered excluded at a confidence level  $CL$  which satisfies:

$$1 - CL_s \leq CL \tag{5.5}$$

It should be noted that the hypothetical false exclusion rate is lower than in the nominal rate  $1 - CL$ , since  $CL_s$  is a ratio of confidences as opposed to a true confidence. As the pdfs of signal+background and background-only become similar, the difference between these rates increases. The  $CL_s$  is therefore inherently conservative and reduces the range of model parameters in which an exclusion result is possible. The coverage of the analysis is increased, while the issue of experiments with larger backgrounds reporting stronger limits is avoided.

The statistical implementation differs slightly from previous dijet analyses. In the past, a background model without nuisance parameters was fitted to the data, and the resulting background fit parameters were used (and fixed) in the subsequent likelihood fits with nuisance parameters. In this analysis, the background fit parameters are treated as unconstrained nuisance parameters in the full likelihood used in all fits.

### 5.2.2 Implementation

The dijet invariant mass  $m_{jj}$  is the discriminating variable for this analysis. Its distribution is used as a probability density function (pdf) to build the likelihood function.

A binned maximum likelihood fit is used by the analysis (un-binned is too computationally intensive, and in this case the exact distribution of events within bins is less important). To explore maximum likelihood estimates, consider a dataset with values  $x_1, \dots, x_n$ . Even if we know the shape of the distribution from which it is drawn, for example an exponential  $\exp(\lambda)$ , the question remains: what is the value of  $\lambda$ ? When presented with random data, for which a certain parametric model has been identified as the most likely origin, the goal is usually to identify the most likely value of the

unknown parameters. Given a parametric model and observed data drawn from it, the binned maximum likelihood fit answers the question: for which parameter value does the observed data have the highest probability? The derivative of the likelihood function can be set equal to zero to find maxima, though in the case of this analysis it is most straightforward to minimise the log likelihood function. The likelihood function is described later in this chapter. The minimisation is performed via Minuit [121], implemented using RooFit.

The compatibility between data and a hypothesis is evaluated by a hypothesis test. A large number of pseudo-datasets are generated for any given hypothesis, and data is compared to these in terms of a test statistic. Pseudodata is generated from un-tagged dijet data. This un-tagged data is fitted with 5 parameter global fit function, and the fraction of events passing 1 or 2 gluon tag selection is computed from MC. These fractions are smoothed to get rid of any statistical fluctuations, and the tagging efficiencies are then applied to the fitted un-tagged data to obtain the pseudo-data. A large number (10,000 or more) pseudoexperiments are generated, by pulling from a poisson distribution at each bin of the nominal fit with mean set to equal the bin. Firstly, a hypothesis test is used to evaluate the match between data and the null ( $\mu = 0$ ) hypothesis. If the test shows no excesses are present, an exclusion limit will be set on the cross section. The hypothesis would be a signal+background hypothesis, with the test statistic built on the signal+background pdf of the discriminating variable.

Agreements or discrepancies must be quantified, and this is achieved through a  $p$ -value, defined as the integral of the test statistic distribution for the test statistic value of the dataset tested to infinity. The test statistic is defined in Chapter 6.

## **Background Model**

The parameterised distribution from which events are assumed to be drawn is one of the family of functions known as the ‘dijet functions’ [122]:

$$f(x) = p_1(1-x)^{p_2}x^{p_3+p_4 \ln(x)+p_5(\ln(x))^2} \quad (5.6)$$

For  $x \equiv m_{jj}/\sqrt{s}$ . This is the five parameter dijet function; setting  $p_5 = 0$  gives the four parameter dijet function, which was found to sufficiently describe the data for this analysis.

While xAW supports the input of signal and background as parameterised analytical functions, models made using Monte Carlo can also be used to create a pdf. The result can be imported into xAW, which can be particularly useful at high mass where there are few data events. xAW then uses it to construct the final likelihood model. The pdf must be a pure shape pdf - attaching constraint pdfs may lead to double-counting of these terms. A shape PDF describes the probability distribution of a single variable or observable of interest. It characterizes how the values of that variable are distributed across its entire range and provides information about the shape of the distribution.

Since the dijet analysis uses a binned likelihood and will use histograms, the mean number of entries in the  $i$ th bin is required for both signal and background:

$$s_i = s_{\text{tot}} \int_{\text{bin}_i} f_s(m_{jj}; \mathbf{p}_s) dm_{jj} \quad (5.7)$$

$$b_i = b_{\text{tot}} \int_{\text{bin}_i} f_b(m_{jj}; \mathbf{p}_b) dm_{jj} \quad (5.8)$$

where  $f_s$  and  $f_b$  are pdfs of  $m_{jj}$  for signal and background respectively.  $s_{\text{tot}}$  and  $b_{\text{tot}}$  are the total mean numbers of signal and background events. RooFit and Quick Fit fit the data so that the sum  $b_{\text{tot}} + s_{\text{tot}}$  is essentially equal to the total number of events. Individually,  $b_{\text{tot}}$  and  $s_{\text{tot}}$  are allowed to float.

### 5.3 Uncertainties

Currently only one source of uncertainty in the background is considered.  $\delta b$  is a statistical uncertainty on the background due to limited statistics used in the fit to  $f_s$

to determine its parameters. Five sources of uncertainty on the signal are included:

- $\delta L$ : uncertainty on the integrated luminosity of the data
- $\delta\epsilon$ : uncertainty on the signal efficiency  $\times$  acceptance
- $\delta t$ : uncertainty on gluon-tag efficiency
- $\delta E_{\text{JER}}$ : uncertainty on jet energy resolution
- $\delta E_{\text{JES}}$ : uncertainty on jet energy scale

These are all treated as shape uncertainties except  $\delta L$ , which is a normalization uncertainty. Each uncertainty is designated a nuisance parameter and associated with the symbols  $\alpha_b, \alpha_L, \alpha_\epsilon, \alpha_t, \alpha_{E_{\text{JER}}}$  and  $\alpha_{E_{\text{JES}}}$ . No theoretical uncertainties in the likelihood function are accounted for. Likelihood functions are discussed in detail in Chapter 6.

Roofit workspaces are created by xAW and passed to QuickLimit and QuickFit to be processed and set limits. A workspace can be made up of and own variables, p.d.f.s, functions and datasets. Limit setting equations are described in detail in Chapter 6.

## 5.4 Pseudodata

It is possible for the fitting procedure to identify false signals. The chance of this happening are quantified by doing spurious signal tests (described in the following section). These should be done on MC, but no MC with sufficient statistics is available for this analysis. Instead background-only pseudodata is generated from a template. After testing several options for generating this pseudodata, the process chosen is as follows. We start with untagged dijet data, applying all the cuts for this analysis. It is fitted with the 5-parameter dijet function and the fraction of events passing the 1- or 2-gluon tag selection are computed from MC. These fractions are smoothed to

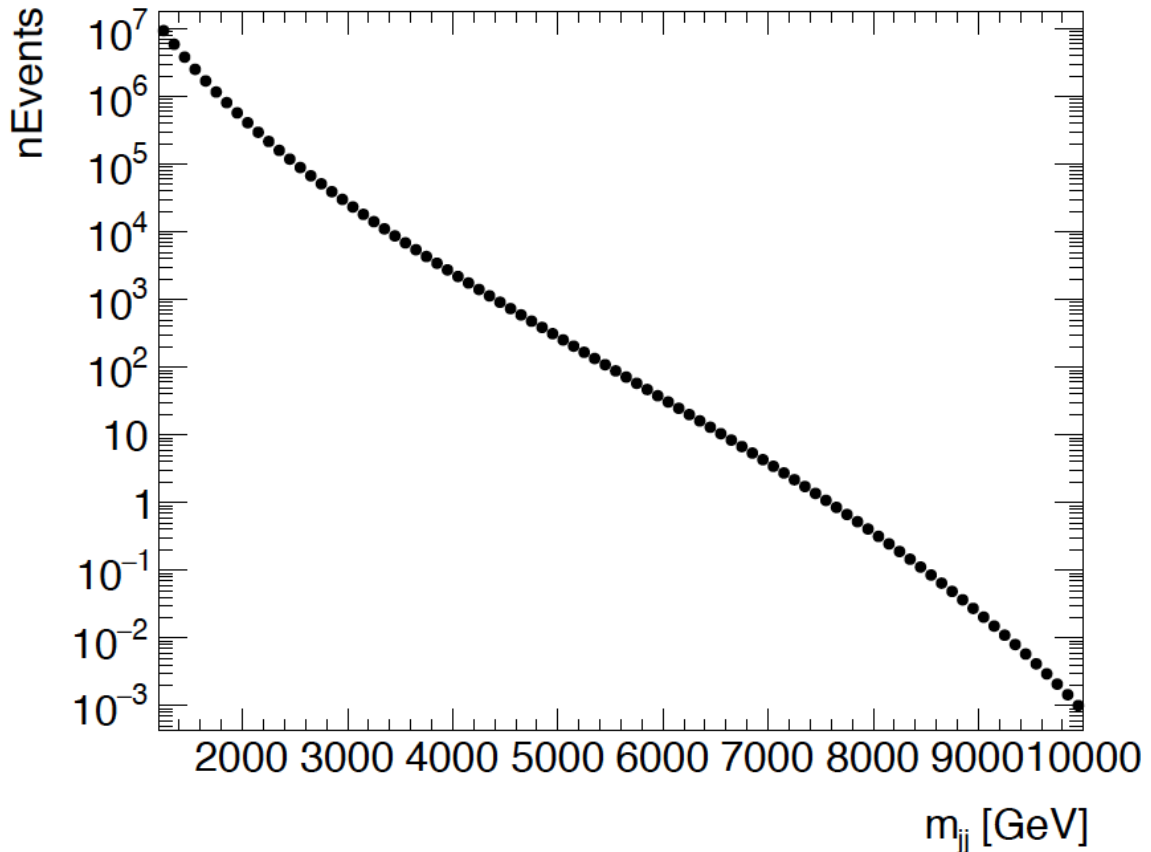


Figure 5.2: Untagged dijet spectrum with  $|y^*| < 0.8$  using full Run-2 data fitted with the 5-parameter global fit function (Equation 5.6).

remove statistical fluctuations and the smoothed tagging efficiencies are applied to the untagged data to obtain pseudodata.

The result of fitting the full Run-2 dataset with the 5-parameter fit function, implemented with Minuit2, is shown in Figure 5.2. To smooth these fractions, a smoothing based on Friedman’s SuperSmoother [123] has been used. The degree of smoothing can be tuned, with a smoothing parameter of 0 being least smooth and 10 being the highest. A variety of values of the parameter were tested, and was chosen to be 7 for the one gluon tag category, as it smooths statistical fluctuation withoutt damping real and important features. The fraction of events passing the one gluon tag selection is shown in Figure 5.3.

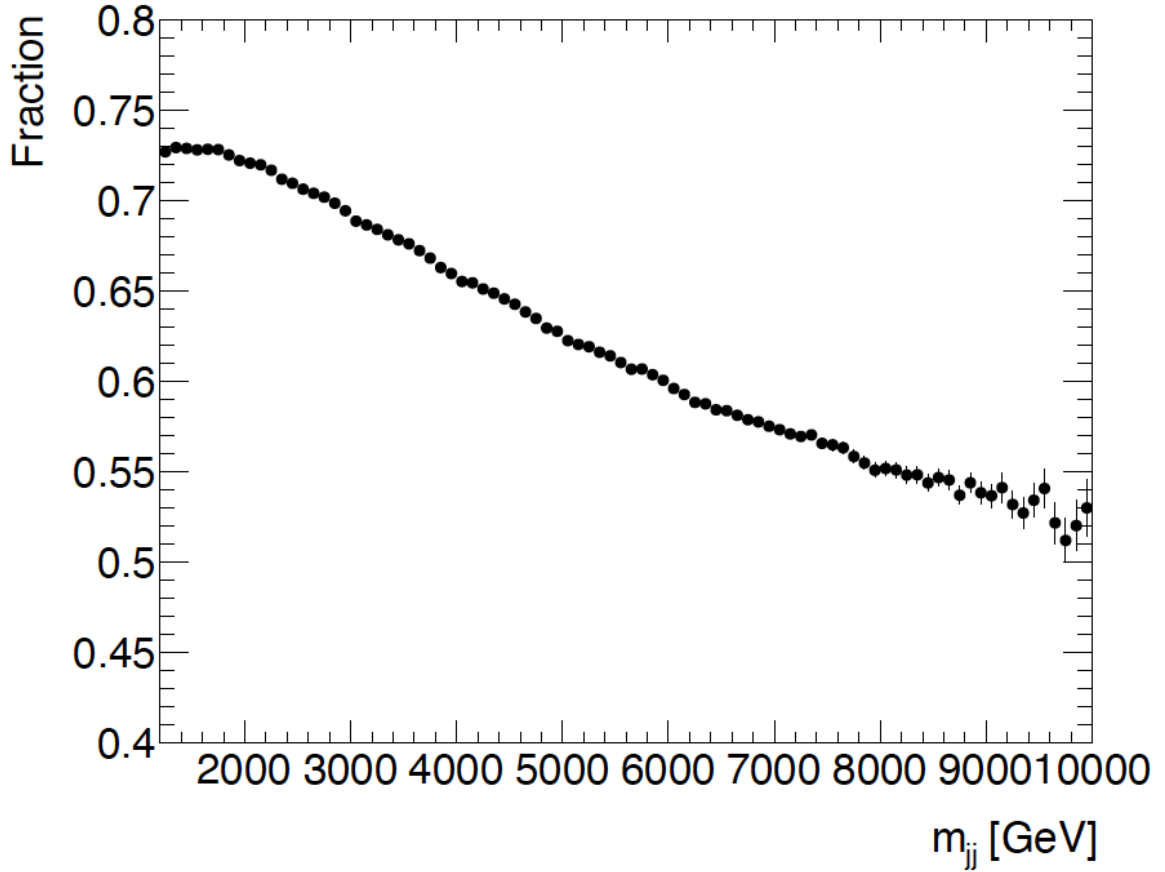


Figure 5.3: To obtain the fraction of events passing one gluon tag selection from the inclusive spectrum, analysis selection cuts are applied to the Pythia dijet MC samples. Figure 27 shows the fraction of the MC events events passing 1 gluon tag selection.

## 5.5 Spurious Signal

Spurious signal corresponds to the difference between the median fitted signal yield and expected signal yield, when fitting a template with known signal yield against a smooth background. Essentially a ‘spurious signal’ is a non-zero signal amplitude obtained when fitting a signal+background model to data known to be signal-free, i.e. a background distribution. Mathematically, a spurious signal is defined as

$$S_{\text{spur}} = S_{\text{fit}} - S_{\text{template}} \quad (5.9)$$

It is the number of signal events extracted by the signal + background fit to the pure background model. In general, if the background model used to fit data does not describe the background distribution without bias, the result will be spurious signal.

It is crucial to confirm that the fit is stable without signal injection, i.e. that on average the number of retrieved events is 0. For this analysis  $S_{\text{spur}}$  was computed by fitting a signal + background model to a background-only template. As described in the previous section, pseudodata is used for a smooth background model, with 100 pseudo-experiments used for these studies. As the injected signal is zero,  $S_{\text{template}} = 0$ . The results of spurious signal tests using Gaussian signal models are shown in Tables 5.1 and 5.2.

mass (GeV)	Mean spurious signal (number of events)	RMS	Mean/RMS
2000	73.03	313.22	0.23
2250	114.36	394.26	0.29
2500	253.20	487.60	0.52
2750	277.55	428.49	0.65
3000	316.75	403.64	0.78
3250	271.73	322.24	0.84
3500	192.74	254.63	0.76
3750	125.73	217.80	0.58
4000	69.90	147.16	0.48
4250	45.91	114.39	0.40
4500	27.19	83.69	0.32
4750	18.27	60.25	0.30
5000	9.33	34.84	0.27
5250	5.17	21.70	0.24
5500	3.29	14.07	0.23
5750	1.31	6.28	0.21
6000	1.14	4.67	0.24
6250	0.89	3.60	0.25
6500	0.69	2.45	0.28
6750	0.40	1.65	0.25
7000	0.30	1.20	0.25
7250	0.26	0.93	0.28
7500	0.24	0.83	0.29
7750	0.21	0.65	0.32
8000	0.15	0.47	0.31

Table 5.1: Spurious Signal tests using Gaussian signals for the 1 gluon tagged category.

Figures 5.4 and 5.5 show the number of signal events detected in each pseudoexperiment. For the 8000 Gev mass point it remains overwhelmingly beneath 4, which

mass (GeV)	Mean no. of spurious signal events	RMS	Mean/RMS
2000	156.41	394.69	0.40
2250	67.82	203.14	0.33
2500	47.42	132.83	0.36
2750	44.70	121.45	0.37
3000	52.05	116.12	0.45
3250	65.07	117.86	0.55
3500	75.23	135.96	0.55
3750	56.01	92.67	0.60
4000	43.56	73.56	0.59
4250	36.52	56.84	0.64
4500	29.88	42.12	0.71
4750	23.79	31.49	0.76
5000	17.39	22.94	0.76
5250	9.71	15.99	0.61
5500	7.31	11.77	0.62
5750	5.02	8.20	0.61
6000	3.81	6.06	0.63
6250	2.67	4.39	0.61
6500	1.88	3.23	0.58
6750	1.34	2.39	0.56
7000	0.93	1.76	0.53
7250	0.64	1.32	0.49
7500	0.41	0.98	0.42
7750	0.26	0.71	0.37
8000	0.19	0.57	0.34

Table 5.2: Spurious Signal tests using Gaussian signals for 2 gluon tagged category.

is negligible. At the lower 4750 GeV mass point  $N_{\text{sig}}$  goes up to almost 160.

The fit is unsuccessful if we allow negative signals (i.e. background higher than

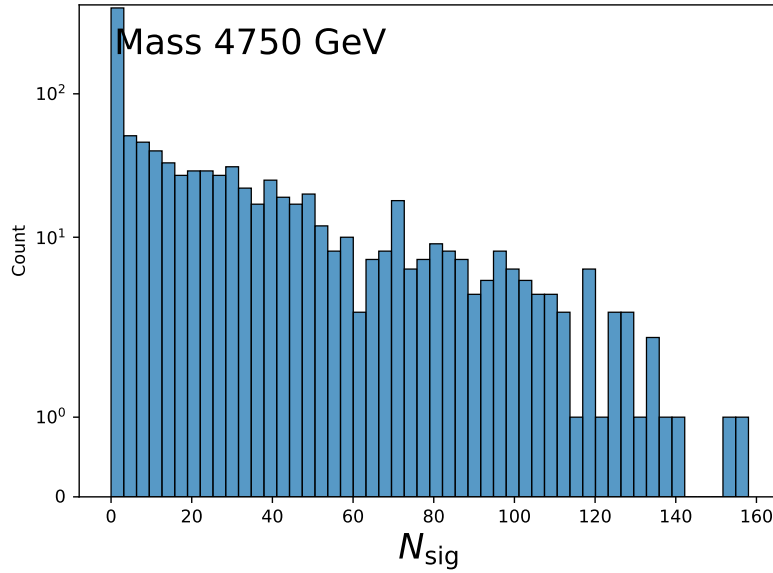


Figure 5.4: The distribution of the number of signal events from 1000 pseudo experiments fitted with a 10% width for a Gaussian with mass 4750 GeV.

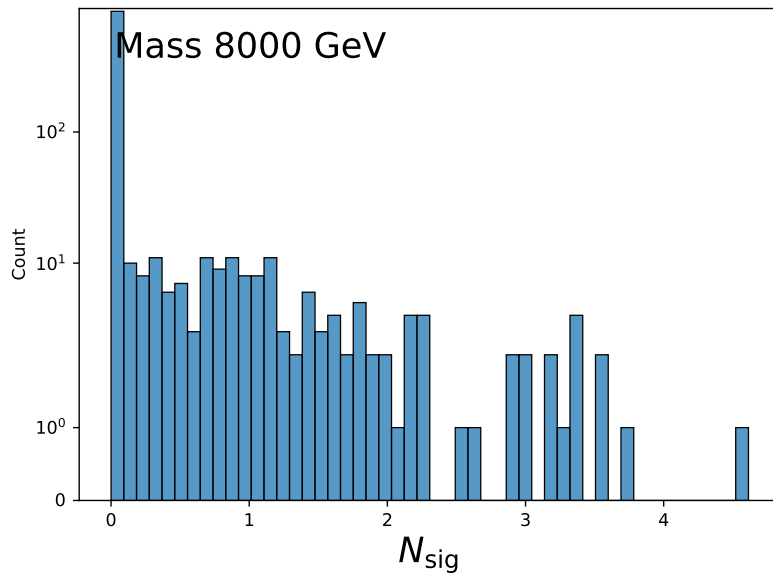


Figure 5.5: The distribution of the number of signal events from 1000 pseudo experiments fitted with an 8 TeV Gaussian with a 10% width for 8000 GeV mass.

spurious signal) at high mass, as RooFit excludes bins with a negative pdf. For large negative signals at high mass, this occurs frequently, biasing the spurious signal. For this reason, having determined the range in which negative signal does give

well-defined fits, we require the signal to be positive. The results for single-tag distributions, requiring  $n_{\text{sig}}$  to be positive definite, are shown in Figure 5.6. This is the mean and width of distributions like Figures 5.4 and 5.5. The horizontal lines correspond to 0.5 and 0.79, the mean of a one-sided Gaussian.

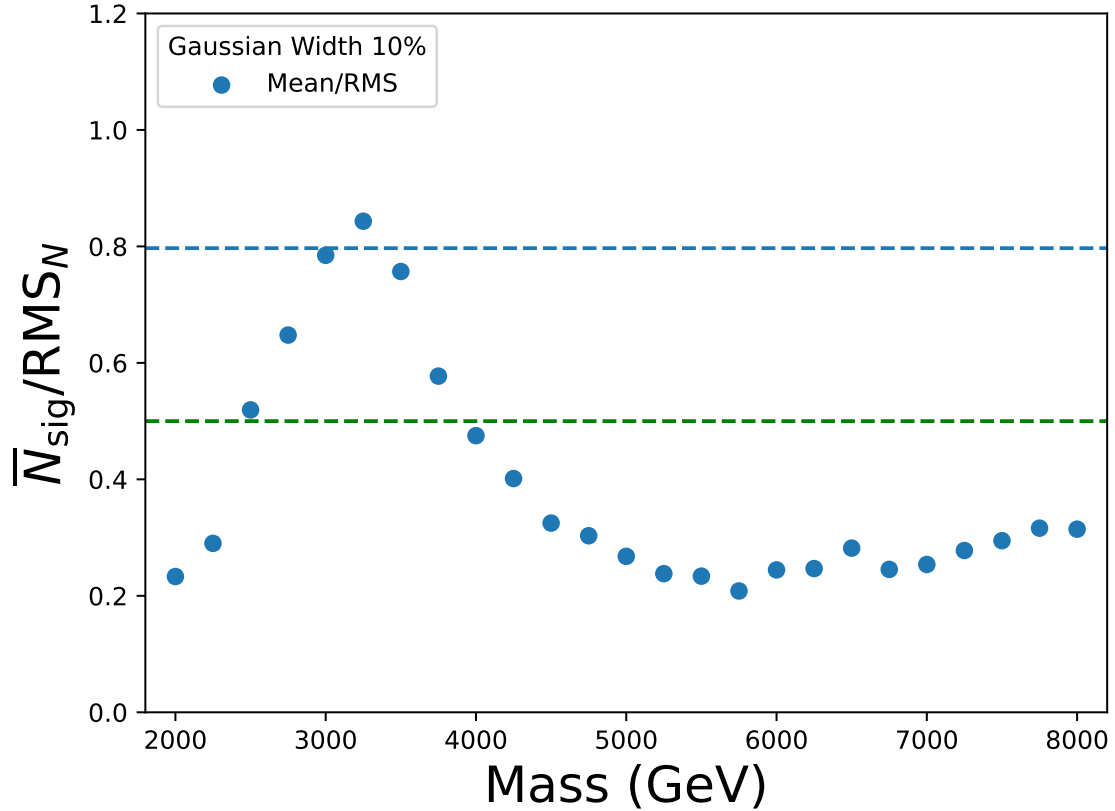


Figure 5.6: Spurious signal for single-tag distributions across the full mass range. The horizontal lines correspond to 0.5 and 0.79, the mean of a one-sided Gaussian. A high signal to noise ratio, i.e. well above the dashed lines, would indicate a signal that is less likely to be random statistical fluctuation.

These plots are effectively a signal to noise ratio, helpful in assessing whether the spurious signal observed is different to the expected background noise. Comparing the points to the means of our Gaussian signal shapes, a high signal to noise ratio, i.e. well above the dashed lines, would indicate a signal that is less likely to be random statistical fluctuation. The results for double-tagged distributions are shown in Figure 5.7, requiring  $n_{\text{sig}}$  to be positive definite. There is a drop in the mean at 5 TeV, this

is due to the fit failing to converge. Work is ongoing to modify the fitting framework to fix this.

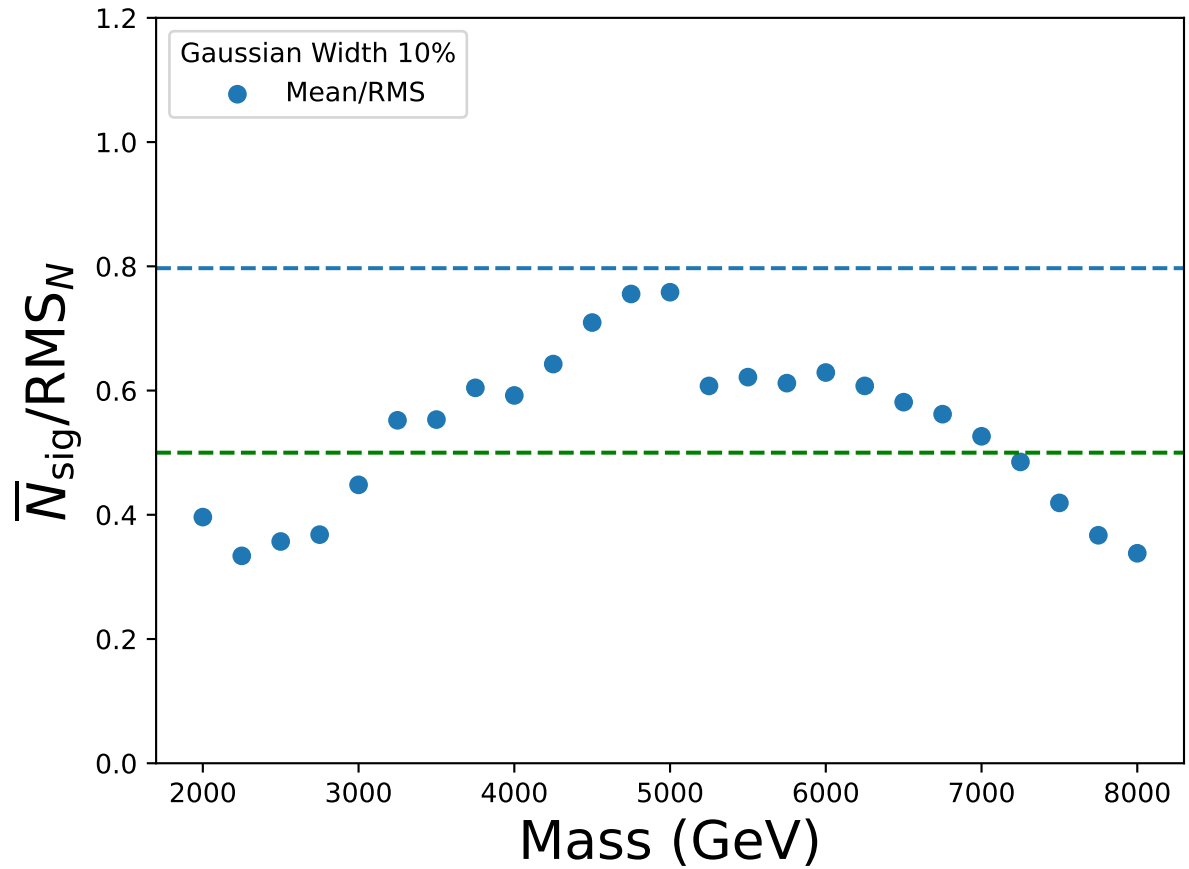


Figure 5.7: Spurious signal for double-tag distributions across the full mass range. The horizontal lines correspond to 0.5 and 0.79, the mean of a one-sided Gaussian. A high signal to noise ratio, i.e. well above the dashed lines, would indicate a signal that is less likely to be random statistical fluctuation.

## 5.6 Signal Injection Tests

To produce a background fit, the full signal range is fitted. Thus if the signal region contains a signal, the background fit will be modified relative to a signal region composed purely of background. The effect of this modification is referred to as fit stability. Because the dijet functions are well-motivated by theory, the effect on the fit of injecting signal (with width much less than the fit range) should be negligible. This must be verified via signal injection tests. These are carried out by fitting a signal + background model to a signal + background template. Different signal strengths are injected which are used to generate pseudo-experiments, 100 of which were used in the studies for this analysis. The results of signal injection tests for the 1 gluon tag category with Gaussians of various widths are shown in Figure 5.8 and the 2 gluon tag category is shown in Figure 5.9.

The injected number of signal events are consistent with the extracted number in the majority of cases, with the 2 TeV 15% Gaussian signals displaying some discrepancies and large error bars due to issues with fit convergence. Where the points are above the grey line, a signal higher than input is being extracted, and below the line the reverse is true. Ideally the points should all sit precisely on the line.

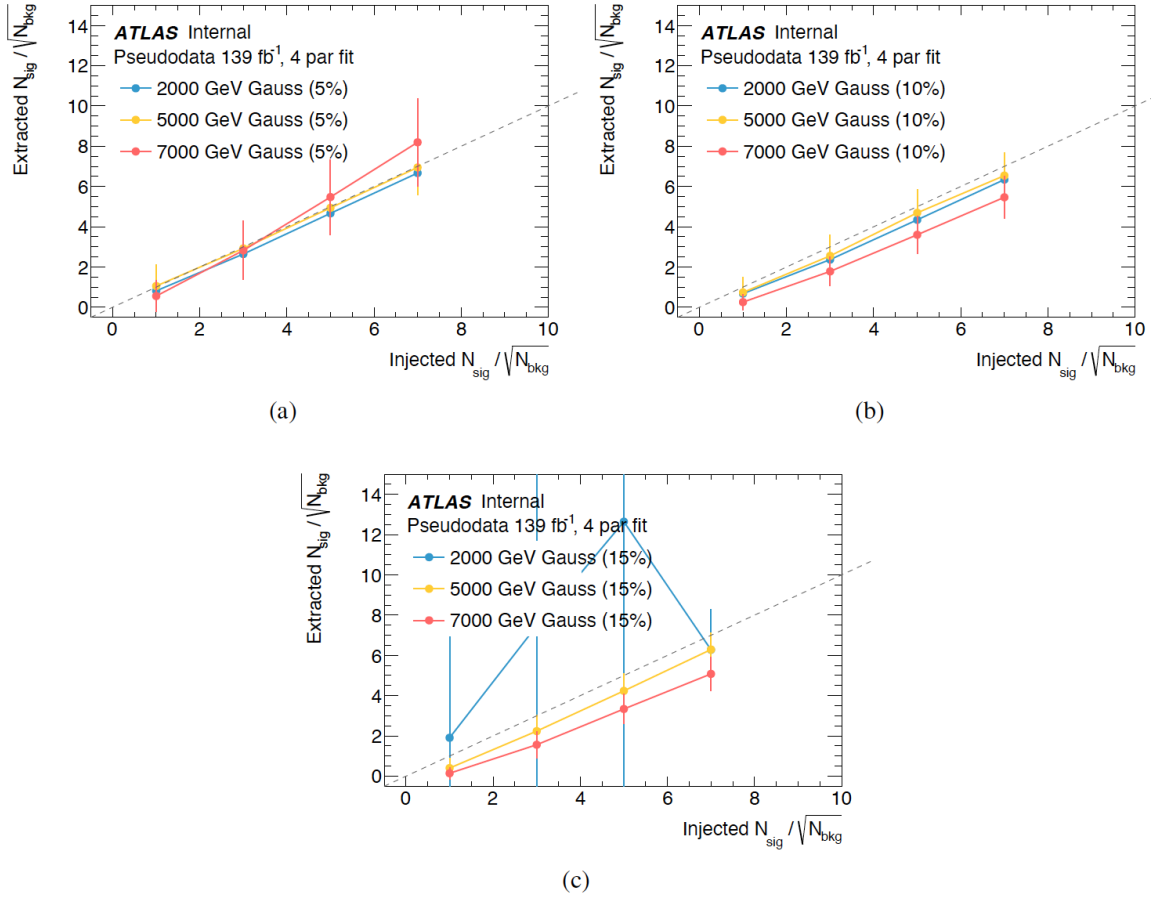


Figure 5.8: Signal injection tests for the 1 gluon tag category using Gaussian signals of (a) 5% width, (b) 10% width and (c) 15% width (of the full fit range). Where the points are above the grey line, a signal higher than input is being extracted, and below the line the reverse is true.

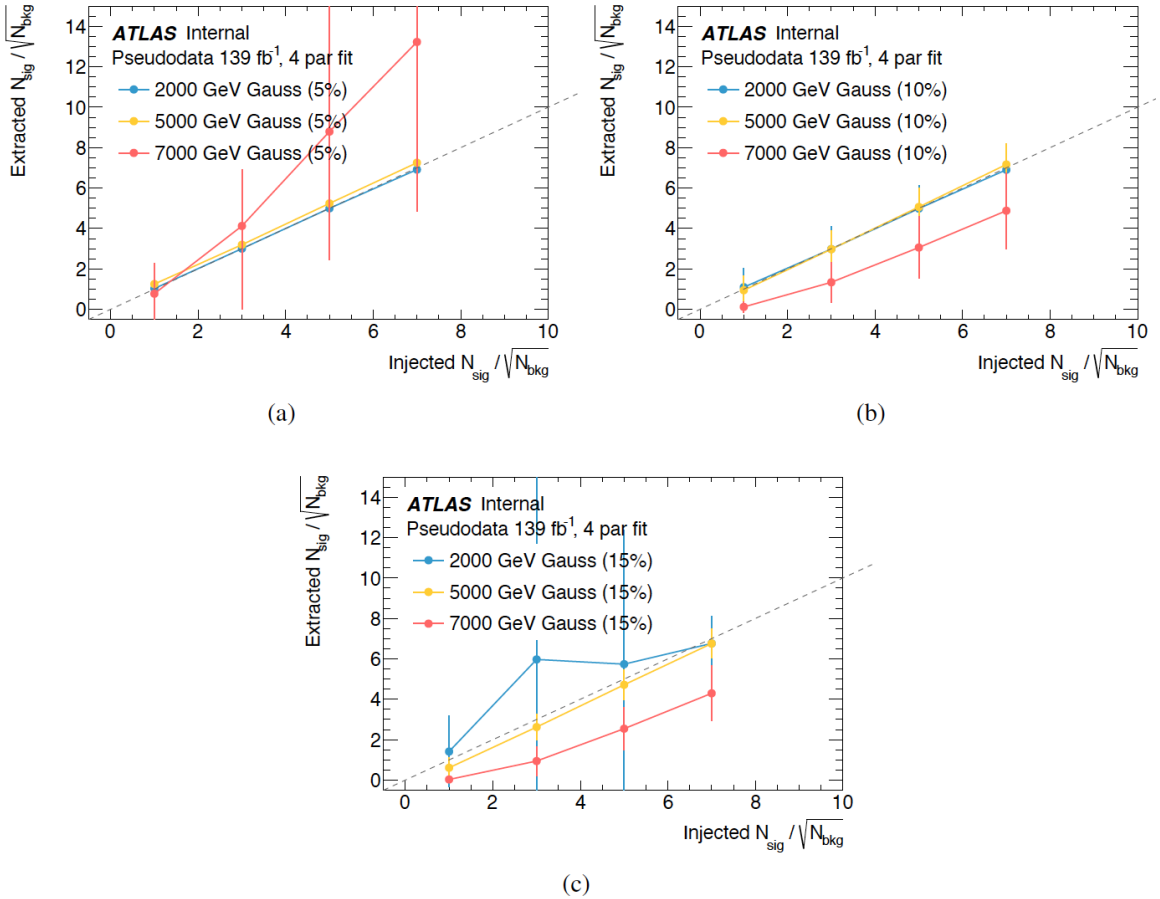


Figure 5.9: Signal injection test for the 2 gluon tag category using Gaussian signals of (a) 5% width, (b) 10% width and (c) 15% width (of the full fit range). The grey dashed line represents the correct result, where the number of extracted signal events is equal to the number of events injected. Where the points are above the grey line, a signal higher than input is being extracted, and below the line the reverse is true.

# Chapter 6

## Results

### 6.1 Model-independent Gaussian Limits

In a resonance-based analysis, a model-independent limit requires a model-independent signal, but these shapes are in general strongly influenced by their specific theoretical origins. The ‘most average’ signal shape should be used to optimise these limits, as determined by studying the range of possible signal shapes any given model allows, and in this analysis Gaussians of varying widths are used. The untagged  $y^* < 0.8$ , one-gluon tagged  $y^* < 0.6$  and two-gluon tagged  $y^* < 0.8$  model-independent limits are shown in Figures 6.1-6.3. The dashed black line is generated by performing statistical simulations (Monte Carlo simulations) that take into account the expected behavior of background processes and systematic uncertainties in the experiment. It represents the median or central value of the expected limit. The green/yellow line on the Brazil plots represents the  $1\sigma/2\sigma$  uncertainty on the expected limit. The width of these bands indicates the range within which the expected limit is likely to fall in a certain fraction of experiments. If the observed data points fall significantly above the expected limit or outside the green uncertainty bands, it may indicate the presence of new physics or deviations from the expected Standard Model behavior.

There are several reasons for the choice of Gaussian. To produce model-independent limits, a ‘model-independent’ resonance signal is required. This analysis is sensitive to shape of any resonances, which is heavily influenced by the specific model. In

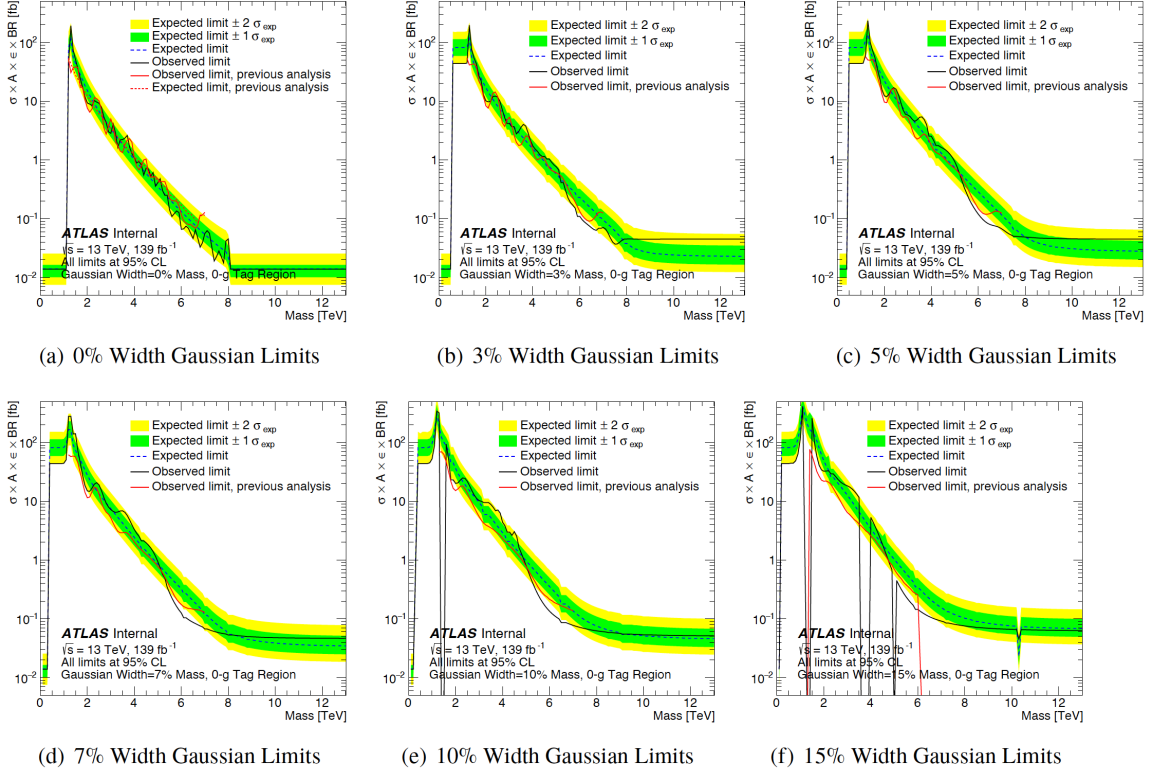


Figure 6.1: Model-independent limits set in the untagged  $y^* < 0.8$  Signal Region using Gaussian resonances of varying widths from 0% to 15% of their peak position without systematics included using the full  $139 \text{ fb}^{-1}$  Run-2 dataset.

general this feature of the analysis is useful but also results in any limits it sets being implicitly influenced by the chosen shape of the resonance. If true independence is not possible, then the goal is to ensure these limits are as model-independent as possible. Choice of a shape close to the ‘average’ signal is key. A proxy for this was chosen to be a Gaussian resonance. A dominant contribution to the shape of any real signal without model-dependent assumptions is the jet resolution, which has an approximately Gaussian shape after reconstruction. Hence a Gaussian resonance should approximately describe any realistic signal. Gaussians with widths equal to 0,3,5,7,10 15% of their peak position are used, as proxies for extremely precise (0%) up to substantially uncertain (15%) measurements .

There are small issues with fit convergence in higher width resonances (evident in the spikes where the fit drops to zero), and modifications to the fitting framework to

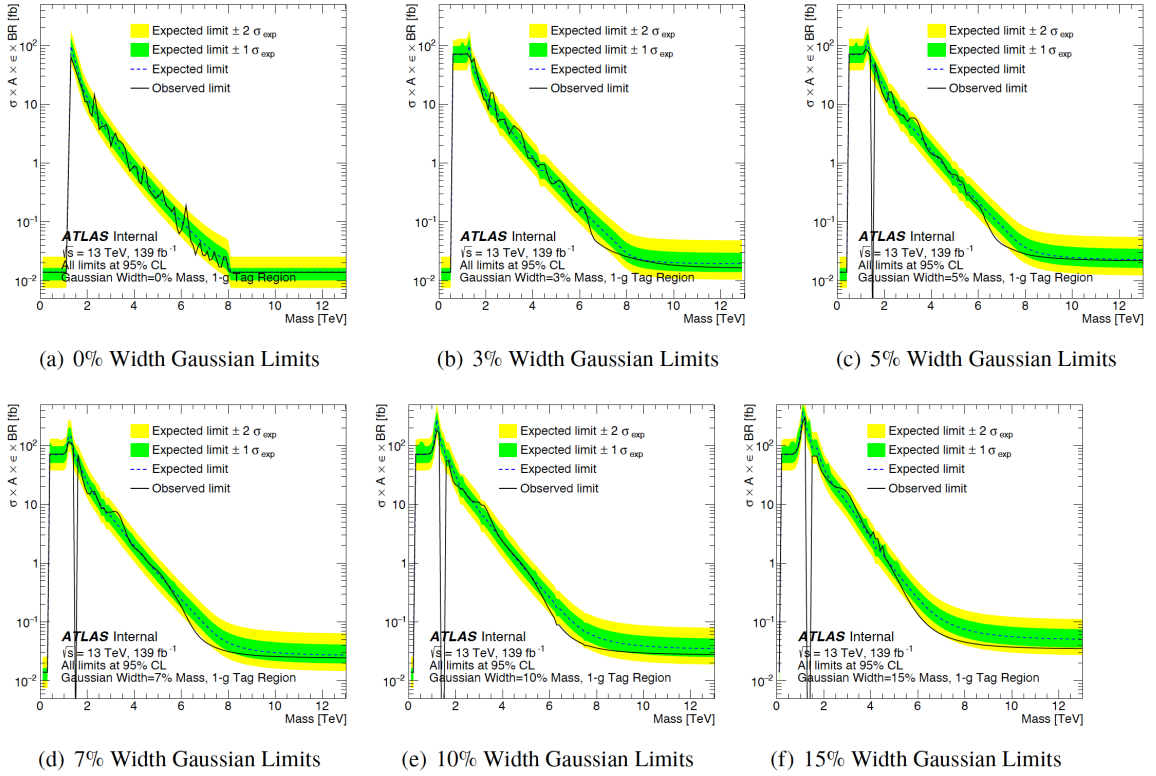


Figure 6.2: Model-independent limits set in the one-gluon tagged  $y^* < 0.6$  Signal Region using Gaussian resonances of varying widths from 0% to 15% of their peak position without systematics included using the full  $139\text{fb}^{-1}$  Run-2 dataset

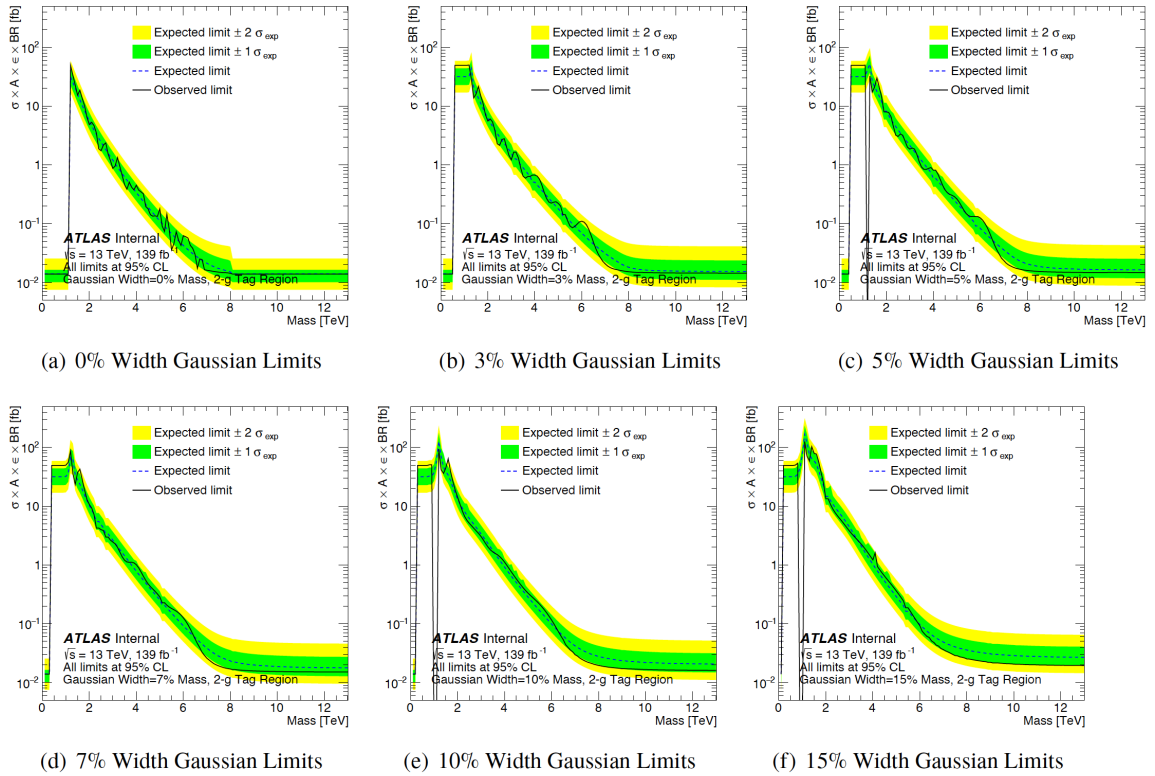


Figure 6.3: Model-independent limits set in the two-gluon tagged  $y^* < 0.8$  Signal Region using Gaussian resonances of varying widths from 0% to 15% of their peak position without systematics included using the full  $139\text{fb}^{-1}$  Run-2 dataset

fix these are currently under investigation. These results do not show deviations from the Standard Model (outside the deviations due to fitting issues).

# Chapter 7

## Conclusion and Future Work

This thesis has presented the implementation of quark-gluon tagging in dijet events at ATLAS. The tagger is a simple  $n_{\text{track}}$ -based tagger and has been shown to improve cross section limits for the  $H'$ , strings and  $q^*$  signal models. This builds on previous work to tag jets at low- $p_T$ , where a jet is classified as gluon-like or quark-like based on the number of tracks being above or below a set limit. In the case of the benchmark  $q^*$  model, when a single jet is required to pass gluon selection, the significance for observing a  $q^*$  is increased by  $\sim 25\%$  for masses above 5 TeV. The biggest increases are seen for a gluon selection efficiency of above 70%. A new method of calculating uncertainties was presented, using purely MC-based techniques, to reduce uncertainties at high  $p_T$ . No evidence of Beyond the Standard Model physics was observed, but the technique shows potential for use in other analyses.

The scope for future work is significant. The analysis was separated from the work of the high mass dijet search team when it proved extremely complex, requiring adjustments to existing software frameworks due to the steeply falling dijet mass spectrum. It was also found that Pythia generators were unable to accurately model  $q^*$  hadronisation, again requiring updates to fix. Additional signal models could be of interest, for example the search for new massive  $Z'$  bosons. The methods presented here can be adapted for more complex taggers in the future, exploiting more features of the radiation pattern inside quark and gluon jets. For example there is potential

to combine information from low-level taggers, such as this  $n_{\text{track}}$ -based tagger, into machine learning classifiers.

# Bibliography

- [1] G. Gabrielse, D. Hanneke, T. Kinoshita, M. Nio, and B. Odom, “New determination of the fine structure constant from the electron  $g$  value and qed,” *Phys. Rev. Lett.*, vol. 97, p. 030802, 3 Jul. 2006. DOI: 10.1103/PhysRevLett.97.030802. [Online]. Available: <https://link.aps.org/doi/10.1103/PhysRevLett.97.030802>.
- [2] W. Commons, “Standard model of particle physics,” Based on <https://www.fnal.gov/pub/inq> [Online]. Available: [https://en.wikipedia.org/wiki/File:Standard\\_Model\\_of\\_Elementary\\_Particles.svg](https://en.wikipedia.org/wiki/File:Standard_Model_of_Elementary_Particles.svg).
- [3] P. Checchia *et al.*, “Measurement of inclusive jet and dijet cross-sections in proton-proton collisions at  $\sqrt{s} = 13$  TeV with the ATLAS detector,” Jul. 2017.
- [4] G. Bertone and D. Hooper, “History of dark matter,” *Reviews of Modern Physics*, vol. 90, no. 4, Oct. 2018. DOI: 10.1103/revmodphys.90.045002. [Online]. Available: <https://doi.org/10.1103%2Frevmodphys.90.045002>.
- [5] R. Harlander, M. Mühlleitner, J. Rathsman, M. Spira, and O. Stål, “Interim recommendations for the evaluation of Higgs production cross sections and branching ratios at the LHC in the Two-Higgs-Doublet Model,” Dec. 2013. arXiv: 1312.5571 [hep-ph].
- [6] I. Antoniadis, E. Kiritsis, and T. N. Tomaras, “A D-brane alternative to unification,” *Phys. Lett. B*, vol. 486, pp. 186–193, 2000. DOI: 10.1016/S0370-2693(00)00733-4. arXiv: hep-ph/0004214.
- [7] P. Meade and L. Randall, “Black holes and quantum gravity at the LHC,” *Journal of High Energy Physics*, vol. 2008, no. 05, pp. 003–003, May 2008. DOI: 10.1088/1126-6708/2008/05/003. [Online]. Available: <https://doi.org/10.1088%5C%2F1126-6708%5C%2F2008%5C%2F05%5C%2F003>.
- [8] A. Collaboration, “Heavy particle searches,” From official plots page, [Online]. Available: <https://atlas.web.cern.ch/Atlas/GROUPS/PHYSICS/PUBNOTES/ATL-PHYS-PUB-2022-011/>.
- [9] C. Collaboration, “Heavy particle searches cms,” <https://twiki.cern.ch/twiki/pub/CMSPublicLimits/HCP2016.pdf>.
- [10] P. Vakilipourtakalou and D. M. Gingrich, *Monte carlo event generator for the production and decay of string resonances in proton-proton collisions*, 2018. arXiv: 1811.07458 [hep-ph].

- [11] E. Eichten, I. Hinchliffe, K. Lane, and C. Quigg, “Supercollider physics,” *Rev. Mod. Phys.*, vol. 56, pp. 579–707, 4 Oct. 1984. DOI: 10.1103/RevModPhys.56.579. [Online]. Available: <https://link.aps.org/doi/10.1103/RevModPhys.56.579>.
- [12] R. Ruiz, *Excited quarks and early discoveries at lhc run ii*. [Online]. Available: <https://www.quantumdiaries.org/2015/02/04/lhc-run-ii-excited-quarks/>.
- [13] M. Aaboud *et al.*, “Search for new phenomena in dijet events using 37 fb<sup>-1</sup> of *pp* collision data collected at  $\sqrt{s} = 13$  TeV with the ATLAS detector,” *Phys. Rev. D*, vol. 96, no. 5, p. 052004, 2017. DOI: 10.1103/PhysRevD.96.052004. arXiv: 1703.09127 [hep-ex].
- [14] U. Baur, M. Spira, and P. M. Zerwas, “Excited Quark and Lepton Production at Hadron Colliders,” *Phys. Rev. D*, vol. 42, pp. 815–824, 1990. DOI: 10.1103/PhysRevD.42.815.
- [15] Baur, Ulrich and Hinchliffe, Ian and Zeppenfeld, Dieter, “Excited quark production at hadron colliders,” 14 p, Jun. 1987. [Online]. Available: <https://cds.cern.ch/record/179084>.
- [16] ATLAS Collaboration, “Search for contact interactions in dilepton events from *pp* collisions at  $\sqrt{s} = 7$  TeV with the ATLAS detector,” *Phys. Lett. B*, vol. 712, pp. 40–58, 2012. DOI: 10.1016/j.physletb.2012.04.026. arXiv: 1112.4462 [hep-ex].
- [17] A. M. Sirunyan *et al.*, “Search for excited quarks of light and heavy flavor in  $\gamma +$  jet final states in proton–proton collisions at  $\sqrt{s} = 13$  TeV,” *Phys. Lett. B*, vol. 781, pp. 390–411, 2018. DOI: 10.1016/j.physletb.2018.04.007. arXiv: 1711.04652 [hep-ex].
- [18] ATLAS Collaboration, “Search for resonances in diphoton events with the ATLAS detector at  $\sqrt{s} = 13$  TeV,” Mar. 2016.
- [19] CMS Collaboration, “Search for resonant production of high-mass photon pairs in proton-proton collisions at  $\sqrt{s} = 8$  and 13 TeV,” *Phys. Rev. Lett.*, vol. 117, p. 051802, 5 Jul. 2016. DOI: 10.1103/PhysRevLett.117.051802. [Online]. Available: <https://link.aps.org/doi/10.1103/PhysRevLett.117.051802>.
- [20] “Search for resonant production of high mass photon pairs using 12.9 fb<sup>-1</sup> of proton-proton collisions at  $\sqrt{s} = 13$  TeV and combined interpretation of searches at 8 and 13 TeV,” 2016.
- [21] Y. Nakai, R. Sato, and K. Tobioka, “Footprints of new strong dynamics via anomaly and the 750 GeV diphoton,” *Phys. Rev. Lett.*, vol. 116, p. 151802, 15 Apr. 2016. DOI: 10.1103/PhysRevLett.116.151802. [Online]. Available: <https://link.aps.org/doi/10.1103/PhysRevLett.116.151802>.
- [22] G. G. Raffelt, “Astrophysical axion bounds,” in *Lecture Notes in Physics*, Springer Berlin Heidelberg, pp. 51–71. DOI: 10.1007/978-3-540-73518-2\_3. [Online]. Available: [https://doi.org/10.1007/978-3-540-73518-2\\_3](https://doi.org/10.1007/978-3-540-73518-2_3).

- [23] S. Chatrchyan *et al.*, “The CMS Experiment at the CERN LHC,” *JINST*, vol. 3, S08004, 2008. DOI: 10.1088/1748-0221/3/08/S08004.
- [24] G. Aad *et al.*, “The ATLAS Experiment at the CERN Large Hadron Collider,” *JINST*, vol. 3, S08003, 2008. DOI: 10.1088/1748-0221/3/08/S08003.
- [25] K. Aamodt *et al.*, “The ALICE experiment at the CERN LHC,” *JINST*, vol. 3, S08002, 2008. DOI: 10.1088/1748-0221/3/08/S08002.
- [26] O. S. Brüning, P. Collier, P. Lebrun, S. Myers, R. Ostojic, J. Poole, and P. Proudlock, *LHC Design Report*, ser. CERN Yellow Reports: Monographs. Geneva: CERN, 2004. DOI: 10.5170/CERN-2004-003-V-1. [Online]. Available: <https://cds.cern.ch/record/782076>.
- [27] P. J. Klimek, “Performance of ATLAS Detector with Start of Run 3,” 2022. [Online]. Available: <https://cds.cern.ch/record/2826480>.
- [28] N. Garelli, “Performance of the ATLAS Detector in Run-2,” *EPJ Web Conf.*, vol. 164, L. Bravina, Y. Foka, and S. Kabana, Eds., p. 01 021, 2017. DOI: 10.1051/epjconf/201716401021.
- [29] ATLAS Collaboration, *Luminosity determination in pp collisions at  $\sqrt{s}=13$  tev using the atlas detector at the lhc*, 2022. DOI: 10.48550/ARXIV.2212.09379. [Online]. Available: <https://arxiv.org/abs/2212.09379>.
- [30] Z. M. and, “Simulation of pile-up in the ATLAS experiment,” *Journal of Physics: Conference Series*, vol. 513, no. 2, p. 022 024, Jun. 2014. DOI: 10.1088/1742-6596/513/2/022024. [Online]. Available: <https://doi.org/10.1088/1742-6596/513/2/022024>.
- [31] J. T. Boyd, “LHC Run-2 and Future Prospects,” in *2019 European School of High-Energy Physics*, Jan. 2020. arXiv: 2001.04370 [hep-ex].
- [32] Novak, Tadej, “New techniques for pile-up simulation in atlas,” *EPJ Web Conf.*, vol. 214, p. 02 044, 2019. DOI: 10.1051/epjconf/201921402044. [Online]. Available: <https://doi.org/10.1051/epjconf/201921402044>.
- [33] G. Aad, J. Adelman, S. Arfaoui, M. Baak, N. Boelaert, S. Burdin, J. Cook, S. D’Auria, M. D’Onofrio, J. A. Frost, C. Guyot, M. Hauschild, R. J. Hawkings, A. Hoecker, G. Iakovidis, M. Iodice, K. J. C. Leney, E. Lytken, M. Martinez-Perez, J. Masik, A. M. Nairz, P. U. E. Onyisi, S. Roe, S. Schaezel, D. Whittington, M. G. Wilson, and S. Zimmermann, “Data quality from the detector control system at the ATLAS experiment,” *Journal of Physics: Conference Series*, vol. 219, no. 2, p. 022 037, Apr. 2010. DOI: 10.1088/1742-6596/219/2/022037. [Online]. Available: <https://doi.org/10.1088/1742-6596/219/2/022037>.
- [34] C. AC, “Layout of ATLAS. Dessin representant le detecteur ATLAS,” Mar. 1998, [Online]. Available: <https://cds.cern.ch/record/39038>.

- [35] T. Heim, “Status and performance of the atlas pixel detector after 3 years of operation,” *Nuclear Instruments and Methods in Physics Research Section A: Accelerators, Spectrometers, Detectors and Associated Equipment*, vol. 765, pp. 227–231, 2014, HSTD-9 2013 - Proceedings of the 9th International ”Hiroshima” Symposium on Development and Application of Semiconductor Tracking Detectors, ISSN: 0168-9002. DOI: <https://doi.org/10.1016/j.nima.2014.04.058>. [Online]. Available: <https://www.sciencedirect.com/science/article/pii/S0168900214004719>.
- [36] “Computer generated image of the atlas calorimeter,” Accessed: 2022-02-20, [Online]. Available: <https://cds.cern.ch/images/CERN-GE-0803015-01>.
- [37] A. Collaboration, “Measurement of the photon identification efficiencies with the ATLAS detector using LHC run-1 data,” *The European Physical Journal C*, vol. 76, no. 12, Dec. 2016. DOI: 10.1140/epjc/s10052-016-4507-9. [Online]. Available: <https://doi.org/10.1140%5C%2Fepjc%5C%2Fs10052-016-4507-9>.
- [38] —, “Muon reconstruction and identification efficiency in atlas using the full run 2 pp collision data set at s=13 tev,” *Eur. Phys. J. C 81 (2021) 578*,
- [39] “Technical Design Report for the Phase-II Upgrade of the ATLAS Muon Spectrometer,”
- [40] G. Aad *et al.*, “Technical Design Report for the Phase-I Upgrade of the ATLAS TDAQ System,” Sep. 2013.
- [41] G. Frattari, “Investigating the nature of dark matter and of the Higgs boson with jets and missing transverse momentum at the LHC,” Presented 22 Feb 2022, Oct. 2021. [Online]. Available: <https://cds.cern.ch/record/2802389>.
- [42] M. zur Nedden, “The Run-2 ATLAS Trigger System: Design, Performance and Plan,” CERN, Geneva, Tech. Rep., Dec. 2016. [Online]. Available: <https://cds.cern.ch/record/2238679>.
- [43] B. Reynolds, “ATLAS jet trigger performance in Run 2 and searching for new physics with trigger-level jets,” Presented 16 Nov 2021, Nov. 2021. [Online]. Available: <https://cds.cern.ch/record/2798574>.
- [44] R. M. Harris and K. Kousouris, “Searches for Dijet Resonances at Hadron Colliders,” *Int. J. Mod. Phys. A*, vol. 26, 5005–5055. 50 p, Oct. 2011, Comments: 50 pages, 23 figures, 5 tables. Submitted to International Journal of Modern Physics A. DOI: 10.1142/S0217751X11054905. arXiv: 1110.5302. [Online]. Available: <https://cds.cern.ch/record/1392965>.
- [45] E. Bothmann, G. S. Chahal, S. Höche, J. Krause, F. Krauss, S. Kuttimalai, S. Liebschner, D. Napoletano, M. Schönherr, H. Schulz, S. Schumann, and F. Siegert, “Event generation with sherpa 2.2,” *SciPost Physics*, vol. 7, no. 3, Sep. 2019. DOI: 10.21468/scipostphys.7.3.034. [Online]. Available: <https://doi.org/10.21468%5C%2Fscipostphys.7.3.034>.

- [46] S. Moretti, *Herwig: An event generator for mssm processes*, 2002. DOI: 10.48550/ARXIV.HEP-PH/0205105. [Online]. Available: <https://arxiv.org/abs/hep-ph/0205105>.
- [47] “Summary of ATLAS Pythia 8 tunes,” Aug. 2012.
- [48] “Summer school lecture,” 2016.
- [49] S. S. Chauhan, “Search for Quark Compositeness at  $\sqrt{s} = 14$  TeV at the Large Hadron Collider,” Ph.D. dissertation, Delhi U., 2010.
- [50] B. Andersson, “The Lund String Model,” in *7th European Symposium on Antiproton Interactions: From LEAR to the Collider and Beyond*, 1986.
- [51] A. Banfi, *Hadronic Jets*, ser. 2053-2571. Morgan & Claypool Publishers, 2016, ISBN: 978-1-6817-4073-7. DOI: 10.1088/978-1-6817-4073-7. [Online]. Available: <https://dx.doi.org/10.1088/978-1-6817-4073-7>.
- [52] G. Stermann and S. Weinberg, “Jets from quantum chromodynamics,” *Phys. Rev. Lett.*, vol. 39, pp. 1436–1439, 23 Dec. 1977. DOI: 10.1103/PhysRevLett.39.1436. [Online]. Available: <https://link.aps.org/doi/10.1103/PhysRevLett.39.1436>.
- [53] J. E. Huth *et al.*, “Toward a standardization of jet definitions,” in *1990 DPF Summer Study on High-energy Physics: Research Directions for the Decade (Snowmass 90)*, Dec. 1990, pp. 0134–136.
- [54] ATLAS Collaboration, “An ATLAS high mass dijet event,” General Photo, Apr. 2014, [Online]. Available: <https://cds.cern.ch/record/1697057>.
- [55] M. Cacciari, G. P. Salam, and G. Soyez, “The anti- $k_t$  jet clustering algorithm,” *Journal of High Energy Physics*, vol. 2008, no. 04, pp. 063–063, Apr. 2008. DOI: 10.1088/1126-6708/2008/04/063. [Online]. Available: <https://doi.org/10.1088/1126-6708/2008/04/063>.
- [56] A. Banfi, M. Dasgupta, and Y. Delenda, “Azimuthal decorrelations between qcd jets at all orders,” *Physics Letters B*, vol. 665, no. 2, pp. 86–91, 2008, ISSN: 0370-2693. DOI: <https://doi.org/10.1016/j.physletb.2008.05.065>. [Online]. Available: <https://www.sciencedirect.com/science/article/pii/S0370269308006618>.
- [57] ATLAS Collaboration, “Quark versus Gluon Jet Tagging Using Charged-Particle Constituent Multiplicity with the ATLAS Detector,” Tech. Rep., May 2017. [Online]. Available: <https://cds.cern.ch/record/2263679>.
- [58] G. Altarelli and G. Parisi, “Asymptotic Freedom in Parton Language,” *Nucl. Phys. B*, vol. 126, pp. 298–318, 1977. DOI: 10.1016/0550-3213(77)90384-4.
- [59] M. Tasevsky, “Differences between Quark and Gluon jets as seen at LEP,” 116–126. 8 p, Oct. 2001. [Online]. Available: <https://cds.cern.ch/record/524941>.
- [60] J. Gallicchio and M. D. Schwartz, “Quark and gluon jet substructure,” *Journal of High Energy Physics*, vol. 2013, no. 4, Apr. 2013. DOI: 10.1007/jhep04(2013)090. [Online]. Available: <https://doi.org/10.1007%2Fjhep04%282013%29090>.

- [61] G. Aad *et al.*, “ATLAS data quality operations and performance for 2015–2018 data-taking,” *JINST*, vol. 15, no. 04, P04003, 2020. DOI: 10.1088/1748-0221/15/04/P04003. arXiv: 1911.04632 [physics.ins-det].
- [62] ATLAS Collaboration, Physics briefing, accessed 20/06/2022, 2019. [Online]. Available: <https://atlas.cern/updates/briefing/data-quality-Run-2>.
- [63] “Search for New Phenomena in Dijet Events using  $139 \text{ fb}^{-1}$  of  $pp$  collisions at  $\sqrt{s} = 13 \text{ TeV}$  collected with the ATLAS Detector,” CERN, Geneva, Tech. Rep., Mar. 2019. [Online]. Available: <https://cds.cern.ch/record/2668385>.
- [64] ATLAS Collaboration, “Search for Quark Contact Interactions in Dijet Angular Distributions in  $pp$  Collisions at  $\sqrt{s} = 7 \text{ TeV}$  Measured with the ATLAS Detector,” *Phys. Lett. B*, vol. 694, pp. 327–345, 2011. DOI: 10.1016/j.physletb.2010.10.021. arXiv: 1009.5069 [hep-ex].
- [65] R. Brun and F. Rademakers, “ROOT: An object oriented data analysis framework,” *Nucl. Instrum. Meth. A*, vol. 389, M. Werlen and D. Perret-Gallix, Eds., pp. 81–86, 1997. DOI: 10.1016/S0168-9002(97)00048-X.
- [66] ATLAS Collaboration, “Topological cell clustering in the ATLAS calorimeters and its performance in LHC Run 1,” *Eur. Phys. J. C*, vol. 77, p. 490, 2017. DOI: 10.1140/epjc/s10052-017-5004-5. arXiv: 1603.02934 [hep-ex].
- [67] W. Lampl, S. Laplace, D. Lelas, P. Loch, H. Ma, S. Menke, S. Rajagopalan, D. Rousseau, S. Snyder, and G. Unal, “Calorimeter Clustering Algorithms: Description and Performance,” CERN, Geneva, Tech. Rep., Apr. 2008. [Online]. Available: <https://cds.cern.ch/record/1099735>.
- [68] ATLAS Collaboration, “Dijet resonance searches with the ATLAS detector at 14 TeV LHC,” 2015.
- [69] —, “Probing the measurement of jet energies with the ATLAS detector using Z+jet events from proton-proton collisions at  $\sqrt{s} = 7 \text{ TeV}$ ,” May 2012.
- [70] “Jet global sequential corrections with the ATLAS detector in proton-proton collisions at  $\sqrt{s} = 8 \text{ TeV}$ ,” CERN, Geneva, Tech. Rep., 2015, All figures including auxiliary figures are available at <https://atlas.web.cern.ch/Atlas/GROUPS/PHYSICS/CONF-2015-002>. [Online]. Available: <https://cds.cern.ch/record/2001682>.
- [71] ATLAS Collaboration, “Jet energy measurement with the ATLAS detector in proton-proton collisions at  $\sqrt{s} = 7 \text{ TeV}$ ,” *Eur. Phys. J. C*, vol. 73, no. 3, p. 2304, 2013. DOI: 10.1140/epjc/s10052-013-2304-2. arXiv: 1112.6426 [hep-ex].
- [72] —, “Jet energy scale measurements and their systematic uncertainties in proton-proton collisions at  $\sqrt{s} = 13 \text{ TeV}$  with the ATLAS detector,” *Phys. Rev. D*, vol. 96, no. 7, p. 072002, 2017. DOI: 10.1103/PhysRevD.96.072002. arXiv: 1703.09665 [hep-ex].
- [73] The ATLAS collaboration, “Jes public plots for moriond.,” <https://atlas.web.cern.ch/Atlas/C/2017-003/>.

- [74] G. Aad *et al.*, “Performance of pile-up mitigation techniques for jets in  $pp$  collisions at  $\sqrt{s} = 8$  TeV using the ATLAS detector,” *Eur. Phys. J. C*, vol. 76, no. 11, p. 581, 2016. DOI: 10.1140/epjc/s10052-016-4395-z. arXiv: 1510.03823 [hep-ex].
- [75] ———, “Electron and photon energy calibration with the ATLAS detector using LHC Run 1 data,” *Eur. Phys. J. C*, vol. 74, no. 10, p. 3071, 2014. DOI: 10.1140/epjc/s10052-014-3071-4. arXiv: 1407.5063 [hep-ex].
- [76] M. Aaboud *et al.*, “Jet energy scale measurements and their systematic uncertainties in proton-proton collisions at  $\sqrt{s} = 13$  TeV with the ATLAS detector,” *Phys. Rev. D*, vol. 96, no. 7, p. 072002, 2017. DOI: 10.1103/PhysRevD.96.072002. arXiv: 1703.09665 [hep-ex].
- [77] T. Yamanaka and A. Collaboration, “The atlas calorimeter simulation fastcalosim,” *Journal of Physics: Conference Series*, vol. 331, no. 3, p. 032053, Dec. 2011. DOI: 10.1088/1742-6596/331/3/032053. [Online]. Available: <https://dx.doi.org/10.1088/1742-6596/331/3/032053>.
- [78] S. Agostinelli, J. Allison, K. Amako, J. Apostolakis, H. Araujo, P. Arce, M. Asai, D. Axen, S. Banerjee, G. Barrand, F. Behner, L. Bellagamba, J. Boudreau, L. Broglia, A. Brunengo, H. Burkhardt, S. Chauvie, J. Chuma, R. Chytrcek, G. Cooperman, G. Cosmo, P. Degtyarenko, A. Dell’Acqua, G. Depaola, D. Dietrich, R. Enami, A. Feliciello, C. Ferguson, H. Fesefeldt, G. Folger, F. Foppiano, A. Forti, S. Garelli, S. Giani, R. Giannitrapani, D. Gibin, J. Gómez Cadenas, I. González, G. Gracia Abril, G. Greeniaus, W. Greiner, V. Grichine, A. Grossheim, S. Guatelli, P. Gumplinger, R. Hamatsu, K. Hashimoto, H. Hasui, A. Heikkinen, A. Howard, V. Ivanchenko, A. Johnson, F. Jones, J. Kallenbach, N. Kanaya, M. Kawabata, Y. Kawabata, M. Kawaguti, S. Kelner, P. Kent, A. Kimura, T. Kodama, R. Kokoulin, M. Kossov, H. Kurashige, E. Lamanna, T. Lampén, V. Lara, V. Lefebvre, F. Lei, M. Liendl, W. Lockman, F. Longo, S. Magni, M. Maire, E. Medernach, K. Minamimoto, P. Mora de Freitas, Y. Morita, K. Murakami, M. Nagamatu, R. Nartallo, P. Nieminen, T. Nishimura, K. Ohtsubo, M. Okamura, S. O’Neale, Y. Oohata, K. Paech, J. Perl, A. Pfeiffer, M. Pia, F. Ranjard, A. Rybin, S. Sadilov, E. Di Salvo, G. Santin, T. Sasaki, N. Savvas, Y. Sawada, S. Scherer, S. Sei, V. Sirotenko, D. Smith, N. Starkov, H. Stoecker, J. Sulkimo, M. Takahata, S. Tanaka, E. Tcherniaev, E. Safai Tehrani, M. Tropeano, P. Truscott, H. Uno, L. Urban, P. Urban, M. Verderi, A. Walkden, W. Wander, H. Weber, J. Wellisch, T. Wenaus, D. Williams, D. Wright, T. Yamada, H. Yoshida, and D. Zschesche, “Geant4—a simulation toolkit,” *Nuclear Instruments and Methods in Physics Research Section A: Accelerators, Spectrometers, Detectors and Associated Equipment*, vol. 506, no. 3, pp. 250–303, 2003, ISSN: 0168-9002. DOI: [https://doi.org/10.1016/S0168-9002\(03\)01368-8](https://doi.org/10.1016/S0168-9002(03)01368-8). [Online]. Available: <https://www.sciencedirect.com/science/article/pii/S0168900203013688>.
- [79] G. Aad *et al.*, “Jet energy scale and resolution measured in proton–proton collisions at  $\sqrt{s} = 13$  TeV with the ATLAS detector,” *Eur. Phys. J. C*, vol. 81,

no. 8, p. 689, 2021. DOI: 10.1140/epjc/s10052-021-09402-3. arXiv: 2007.02645 [hep-ex].

- [80] P. Bagnaia, M. Banner, R. Battiston, P. Bloch, K. Borer, M. Borghini, J. Bürger, P. Cenci, J.-C. Cholle, A. Clark, C. Conta, P. Darriulat, L. Di Lella, J. Dines-Hansen, R. Engelmann, L. Fayard, M. Fraternali, D. Froidevaux, J.-M. Gaillard, O. Gildemeister, V. Goggi, C. Gössling, B. Hahn, H. Hänni, J. Hansen, P. Hansen, N. Harnew, T. Himel, P. Jenni, O. Kofoed-Hansen, E. Lançon, M. Livan, S. Loucatos, B. Madsen, P. Mani, B. Mansoulié, G. Mantovani, L. Mapelli, B. Merkel, R. Mollerud, C. Onions, G. Parrou, F. Pastore, H. Plothow-Besch, M. Polverel, J.-P. Repellin, A. Rothenberg, A. Roussarie, G. Sauvage, J. Schacher, J. Siegrist, G. Stimpfl, F. Stocker, M. Swartz, J. Teiger, S. Tovey, V. Vercesi, A. Weidberg, H. Zacccone, J. Zakrzewski, and W. Zeller, “Measurement of jet production properties at the cern pp collider,” *Physics Letters B*, vol. 144, no. 3, pp. 283–290, 1984, ISSN: 0370-2693. DOI: [https://doi.org/10.1016/0370-2693\(84\)91822-7](https://doi.org/10.1016/0370-2693(84)91822-7). [Online]. Available: <https://www.sciencedirect.com/science/article/pii/0370269384918227>.
- [81] G. Romeo, A. Schwartzman, R. Piegai, T. Carli, and R. Teuscher, “Jet Energy Resolution from In-situ Techniques with the ATLAS Detector Using Proton-Proton Collisions at a Center of Mass Energy  $\sqrt{s} = 7$  TeV,” CERN, Geneva, Tech. Rep., 2011. [Online]. Available: <https://cds.cern.ch/record/1334193>.
- [82] N. Grau, B. A. Cole, W. G. Holzmann, M. Spousta, and P. Steinberg, “Identification and Rejection of Fake Reconstructed Jets From a Fluctuating Heavy Ion Background in ATLAS,” *Eur. Phys. J. C*, vol. 62, S. Bass, H. Caines, M. Calderon de la Barca Sanchez, A. De Falco, C. Kuhn, J. Nagle, M. Nardi, C. Salgado, and J. Velkovska, Eds., pp. 191–196, 2009. DOI: 10.1140/epjc/s10052-009-0952-z. arXiv: 0810.1219 [nucl-ex].
- [83] ATLAS Collaboration, “Selection of jets produced in 13TeV proton-proton collisions with the ATLAS detector,” CERN, Geneva, Tech. Rep., Jul. 2015. [Online]. Available: <https://cds.cern.ch/record/2037702>.
- [84] —, “Characterisation and mitigation of beam-induced backgrounds observed in the ATLAS detector during the 2011 proton-proton run,” *Journal of Instrumentation*, vol. 8, no. 07, P07004–P07004, Jul. 2013. DOI: 10.1088/1748-0221/8/07/p07004. [Online]. Available: <https://doi.org/10.1088%5C%2F1748-0221%5C%2F8%5C%2F07%5C%2Fp07004>.
- [85] —, “ATLAS Pythia 8 tunes to 7 TeV data,” CERN, Geneva, Tech. Rep., Nov. 2014. [Online]. Available: <https://cds.cern.ch/record/1966419>.
- [86] J. Pumplin, D. R. Stump, J. Huston, H.-L. Lai, P. Nadolsky, and W.-K. Tung, “New generation of parton distributions with uncertainties from global QCD analysis,” *Journal of High Energy Physics*, vol. 2002, no. 07, pp. 012–012, Jul. 2002. DOI: 10.1088/1126-6708/2002/07/012. [Online]. Available: <https://doi.org/10.1088%5C%2F1126-6708%5C%2F2002%5C%2F07%5C%2F012>.

- [87] G. Watt and R. S. Thorne, “Study of Monte Carlo approach to experimental uncertainty propagation with MSTW 2008 PDFs,” *JHEP*, vol. 08, p. 052, 2012. DOI: 10.1007/JHEP08(2012)052. arXiv: 1205.4024 [**hep-ph**].
- [88] S. Carrazza, S. Forte, and J. Rojo, *Parton distributions and event generators*, 2013. DOI: 10.48550/ARXIV.1311.5887. [Online]. Available: <https://arxiv.org/abs/1311.5887>.
- [89] A. Cooper-Sarkar, “HERAPDF1.5LO PDF Set with Experimental Uncertainties,” in *Proceedings of XXII. International Workshop on Deep-Inelastic Scattering and Related Subjects — PoS(DIS2014)*, vol. 203, 2014, p. 032. DOI: 10.22323/1.203.0032.
- [90] ATLAS Collaboration, “ATLAS tunes of PYTHIA 6 and Pythia 8 for MC11,” CERN, Geneva, Tech. Rep., Jul. 2011, All figures including auxiliary figures are available at <https://atlas.web.cern.ch/Atlas/GROUPS/PHYSICS/PUBNOTES/ATL-PHYS-PUB-2011-009>. [Online]. Available: <https://cds.cern.ch/record/1363300>.
- [91] —, “Properties of jets measured from tracks in proton-proton collisions at center-of-mass energy  $\sqrt{s} = 7$  TeV with the ATLAS detector,” *Phys. Rev. D*, vol. 84, p. 054001, 2011. DOI: 10.1103/PhysRevD.84.054001. arXiv: 1107.3311 [**hep-ex**].
- [92] —, “Jet mass and substructure of inclusive jets in  $\sqrt{s} = 7$  TeV  $pp$  collisions with the ATLAS experiment,” *JHEP*, vol. 05, p. 128, 2012. DOI: 10.1007/JHEP05(2012)128. arXiv: 1203.4606 [**hep-ex**].
- [93] S. Agostinelli *et al.*, “GEANT4—a simulation toolkit,” *Nucl. Instrum. Meth. A*, vol. 506, pp. 250–303, 2003. DOI: 10.1016/S0168-9002(03)01368-8.
- [94] Produced with other members of the ATLAS analysis group.
- [95] H. Brooks and P. Skands, “Coherent showers in decays of colored resonances,” *Physical Review D*, vol. 100, no. 7, Oct. 2019. DOI: 10.1103/physrevd.100.076006. [Online]. Available: <https://doi.org/10.1103/physrevd.100.076006>.
- [96] T. Sjostrand, S. Mrenna, and P. Z. Skands, “A Brief Introduction to PYTHIA 8.1,” *Comput. Phys. Commun.*, vol. 178, pp. 852–867, 2008. DOI: 10.1016/j.cpc.2008.01.036. arXiv: 0710.3820 [**hep-ph**].
- [97] R. D. Ball *et al.*, “Parton distributions with LHC data,” *Nucl. Phys. B*, vol. 867, pp. 244–289, 2013. DOI: 10.1016/j.nuclphysb.2012.10.003. arXiv: 1207.1303 [**hep-ph**].
- [98] G. Aad *et al.*, “Measurement of the charged-particle multiplicity inside jets from  $\sqrt{s} = 8$  TeV  $pp$  collisions with the ATLAS detector,” *Eur. Phys. J. C*, vol. 76, no. 6, p. 322, 2016. DOI: 10.1140/epjc/s10052-016-4126-5. arXiv: 1602.00988 [**hep-ex**].

- [99] T. Sjöstrand, S. Mrenna, and P. Skands, “A brief introduction to PYTHIA 8.1,” *Computer Physics Communications*, vol. 178, no. 11, pp. 852–867, Jun. 2008. DOI: 10.1016/j.cpc.2008.01.036. [Online]. Available: <https://doi.org/10.1016%2Fj.cpc.2008.01.036>.
- [100] J. Gao, M. Guzzi, J. Huston, H.-L. Lai, Z. Li, P. Nadolsky, J. Pumplin, D. Stump, and C.-P. Yuan, “CT10 next-to-next-to-leading order global analysis of QCD,” *Physical Review D*, vol. 89, no. 3, Feb. 2014. DOI: 10.1103/physrevd.89.033009. [Online]. Available: <https://doi.org/10.1103%2Fphysrevd.89.033009>.
- [101] M. Bähr, S. Gieseke, and M. Seymour, “Simulation of multiple partonic interactions in herwig++,” English, *The Journal of High Energy Physics*, vol. 2008, no. 7, Jul. 2008, Baehr, Manuel Gieseke, Stefan Seymour, Michael H. 54 INT SCHOOL ADVANCED STUDIES TRIESTE 333HR, ISSN: 1126-6708. DOI: 10.1088/1126-6708/2008/07/076.
- [102] P. M. Nadolsky, H.-L. Lai, Q.-H. Cao, J. Huston, J. Pumplin, D. Stump, W.-K. Tung, and C.-P. Yuan, “Implications of CTEQ global analysis for collider observables,” *Physical Review D*, vol. 78, no. 1, Jul. 2008. DOI: 10.1103/physrevd.78.013004. [Online]. Available: <https://doi.org/10.1103%2Fphysrevd.78.013004>.
- [103] A. Buckley, J. Ferrando, S. Lloyd, K. Nordström, B. Page, M. Rüfenacht, M. Schönherr, and G. Watt, “LHAPDF6: Parton density access in the LHC precision era,” *The European Physical Journal C*, vol. 75, no. 3, Mar. 2015. DOI: 10.1140/epjc/s10052-015-3318-8. [Online]. Available: <https://doi.org/10.1140%2Fepjc%2Fs10052-015-3318-8>.
- [104] ATLAS Collaboration, “Example ATLAS tunes of Pythia8, Pythia6 and Powheg to an observable sensitive to  $Z$  boson transverse momentum,” CERN, Geneva, Tech. Rep., Nov. 2013. [Online]. Available: <https://cds.cern.ch/record/1629317>.
- [105] E. Maguire, L. Heinrich, and G. Watt, “HEPData: A repository for high energy physics data,” *Journal of Physics: Conference Series*, vol. 898, p. 102 006, Oct. 2017. DOI: 10.1088/1742-6596/898/10/102006. [Online]. Available: <https://doi.org/10.1088%5C%2F1742-6596%5C%2F898%5C%2F10%5C%2F102006>.
- [106] G. Aad, F. Barreiro, and I. Caprini, “Light-quark and gluon jet discrimination in  $pp$  collisions at  $\sqrt{s}=7\text{TeV}$  with the atlas detector,” *Eur.Phys.J.*, vol. C74, p. 3023, Aug. 2014. DOI: 10.1140/epjc/s10052-014-3023-z.
- [107] “Alignment of the ATLAS Inner Detector Tracking System with 2010 LHC proton-proton collisions at  $\sqrt{s} = 7 \text{ TeV}$ ,” CERN, Geneva, Tech. Rep., Mar. 2011. [Online]. Available: <https://cds.cern.ch/record/1334582>.
- [108] A. L. Read, “Modified frequentist analysis of search results (the  $CL_s$  method),” 2000. DOI: 10.5170/CERN-2000-005.81. [Online]. Available: <https://cds.cern.ch/record/451614>.

- [109] A. L. Read, “Presentation of search results: The CL(s) technique,” *J. Phys. G*, vol. 28, M. R. Whalley and L. Lyons, Eds., pp. 2693–2704, 2002. DOI: 10.1088/0954-3899/28/10/313.
- [110] G. Cowan, K. Cranmer, E. Gross, and O. Vitells, “Asymptotic formulae for likelihood-based tests of new physics,” *Eur. Phys. J. C*, vol. 71, p. 1554, 2011, [Erratum: *Eur.Phys.J.C* 73, 2501 (2013)]. DOI: 10.1140/epjc/s10052-011-1554-0. arXiv: 1007.1727 [physics.data-an].
- [111] B. Whitmore, “Search for beyond the standard model signals in a quark-gluon tagged dijet final state with the atlas detector,” English, Ph.D. dissertation, Lancaster University, Sep. 2019. DOI: 10.17635/lancaster/thesis/738.
- [112] H. Yang, *Xml analytic workspace builder*, <https://twiki.cern.ch/twiki/bin/view/AtlasProtected/XmlAnaWSBuilder>, 2021.
- [113] W. Verkerke and D. Kirkby, *The roofit toolkit for data modeling*, 2003. DOI: 10.48550/ARXIV.PHYSICS/0306116. [Online]. Available: <https://arxiv.org/abs/physics/0306116>.
- [114] T. A. H. Group, “Xmlanawsbuilder,” Provided by Dr Hongtao Yang.1§.
- [115] H. Yang, *Quickfit*, 2021. [Online]. Available: %5Curl%7Bhttps://gitlab.cern.ch/atlas\_higgs\_combination/software/quickFit%7D.
- [116] L. Moneta, K. Belasco, K. S. Cranmer, S. Kreiss, A. Lazzaro, D. Piparo, G. Schott, W. Verkerke, and M. Wolf, “The RooStats Project,” *PoS*, vol. ACAT2010, T. Speer, F. Boudjema, J. Lauret, A. Naumann, L. Teodorescu, and P. Uwer, Eds., p. 057, 2010. DOI: 10.22323/1.093.0057. arXiv: 1009.1003 [physics.data-an].
- [117] V. V. Gligorov, S. Hageboeck, T. Nanut, A. Sciandra, and D. Y. Tou, “Avoiding biases in binned fits,” *JINST*, vol. 16, no. 08, T08004, 2021. DOI: 10.1088/1748-0221/16/08/T08004. arXiv: 2104.13879 [physics.data-an].
- [118] P. Francavilla, “Measurements of inclusive jet and dijet cross sections at the Large Hadron Collider,” *Int. J. Mod. Phys. A*, vol. 30, no. 31, p. 1546003, 2015. DOI: 10.1142/S0217751X15460033. arXiv: 1510.01943 [hep-ex].
- [119] G. J. Feldman and R. D. Cousins, “Unified approach to the classical statistical analysis of small signals,” *Physical Review D*, vol. 57, no. 7, pp. 3873–3889, Apr. 1998. DOI: 10.1103/physrevd.57.3873. [Online]. Available: <https://doi.org/10.1103%2Fphysrevd.57.3873>.
- [120] G. Zech, “Upper Limits in Experiments with Background Or Measurement Errors,” *Nucl. Instrum. Meth. A*, vol. 277, p. 608, 1989. DOI: 10.1016/0168-9002(89)90795-X.
- [121] F. James and M. Winkler, “MINUIT User’s Guide,” Jun. 2004.
- [122] CERN, “Dijet functions,” <https://arxiv.org/pdf/1110.5302.pdf>.
- [123] Friedman’s super smoother.